Cătălin Balan

CONTRIBUTION TO THE SCINTILLATION DETECTION OPTIMIZATION IN DOUBLE PHASE DETECTORS FOR DIRECT DETECTION OF DARK MATTER

Tese de doutoramento em Engenharia Física, ramo de Instrumentação, orientada por Professor Doutor José Antonio Matias Lopes e Professor Doutor Joaquim Marques Ferreira dos Santos apresentada no Departamento de Física da Faculdade de Ciências e Tecnologia da Universidade de Coimbra

Outubro de 2014

· U C ·

Universidade de Coimbra

CĂTĂLIN BALAN

CONTRIBUTION TO THE SCINTILLATION DETECTION OPTIMIZATION IN DOUBLE PHASE DETECTORS FOR DIRECT DETECTION OF DARK MATTER

Thesis submitted to Physics Department of Coimbra University for the degree of *Phylosophiae Doctor* in *Physics Engineering* under the supervision of

Prof. Dr. José Antonio Matias Lopes
and
Prof. Dr. Joaquim Marques Ferreira dos Santos

October 2014

UNIVERSIDADE DE COIMBRA

This work was supported by *Fundação para a Ciência e Tecnologia (FCT)* and *Fundo Social Europeu*, through *Programa Operacional Potencial Humano (POPH)* and the PhD grant *SFRH/ BD/ 72334/ 2010*

To my loving wife,

Table of Contents

List of figures

List of tables

List of Abbreviations

2dFGRS – 2 degree Field Galaxy Redshift Survey

2D – 2 Dimensional

3D – 3 Ddimensional

AMS-2 – Alpha Magnetic Spectrometer experiment

atm – atmosphere

CDMS – Cryogenic Dark Matter Search experiment

CoGeNT – Coherent Germanium Neutrino Technology experiment

CMB – Cosmic Microwave Background

DAMA – DArk MAtter experiment

DAQ – Data AQuisition

EL - ElectroLuminescence

ER – Electronic Recoil

evts – events

eV – electron Volt

FIG – Figure

FPGA – Field Programable Gate Array

FV – Fiducial Volume

GXe – Gas Xenon

HV – High Voltage

K – Kelvin

LED – Light Emitting Diode

LN_2 – Liquid Nitrogen

LNGS – Laboratori Nazionali del Gran Sasso

LUX – Large Underground Xenon experiment

LXe – Liquid Xenon

LXeGRIT – Liquid Xenon Gamma Ray Imaging Telescope experiment

MC – Monte Carlo

NR – Nuclear Recoil

OFHC – Oxygen Free High Conductivity

pe – photoelectron

ppb – parts per billion

ppm – parts per million

ppt – parts per trillion

PL – Profile Likelihood

PMT – Photo Multiplier Tubes

PTFE – PolyTetraFluoroEthylene

PTR – Pulse Tube Refrigerator

RESTOX – REcovering and STOrage system for Xenon

QCD – Quantum Chrome Dynamics

SC – Slow Control

SCS – Slow Control System

SDSS – Sloan Digital Sky Survey

slpm – standard liters per minute

SUSY - SUperSYmmetry

TPC – Time Projection Chamber

UV – Ultra Violet

VUV – Vacuum Ultra Violet

WIMP – Weakly Interacting Massive Particle

WMAP – Wilkinson Microwave Anisotropy Probe

WG – Working Group

ZEPLIN – ZonEd Proportional scintillation in LIquid Noble gases

Aknowledgements

First and foremost, I would like to thank to my supervisors, *Professor José Antonio Matias Lopes* and *Professor Joaquim Marques Ferreira dos Santos* from Coimbra University – Portugal, for valuable guidance and advices. They inspired me greatly to work in XENON experiment for direct Dark Matter searches. Their willingness to motivate me contributed tremendously to my work. I also would like to thank them for all the documentation and examples related to the topic of this thesis. I also give my sincere thanks to *Professor Elena Aprile* from Columbia University – New York USA, for allowing me be part of such a competitive experiment that she is leading.

Besides, I would like to thank *GIAN (Grupo de Instrumentação Atómica e Nuclear)* from Physics Department, Coimbra – Portugal, for providing me a good environment and facilities to do the work and because they initiated me in the field of the noble gas detectors. Special thanks to *Elisabete Freitas, Hugo Natal da Luz, Luis Panchorrinha Fernandes, Fernando Amaro, Andrêa Gouvêa, Artur Coimbra* and *Cristina Monteiro.* Many thanks to *Paulo Gomes*, for the computers support.

Further, but not least, I would like to thank and offer gratitude to my colleague *Sonja Orrigo,* for advices and suggestions in the data analysis, and to the *colleagues from* other *XENON Collaboration teams,* for many helpful discussions on the teleconferences during my activity in XENON Experiment.

Special thanks to *Alfredo Davide Ferella* for all his help and coordination during my XENON100 shifts at Gran Sasso National Laboratory in Italy.

Best regards to *Sónia Branco* and *Isabel Melo* from ADDF (Associação para Desenvolvimento do Departamento de Física), to *Elisabete Freitas* and to my old friend *Constantin Taivan* for their sincere and warm friendship.

In the last year, *my wife Alexandra* supported me a lot and she deserves also my best thanks for all the encouragements, love, patience and peace that she is offering to me.

Abstract of the Thesis

CĂTĂLIN BALAN

Physics Department
Faculty of Science and Technology - University of Coimbra, Portugal

Contribution to the scintillation detection optimization in double phase detectors for direct detection of dark matter

In the past decade, tremendous advances have been made in the development of detectors to be used for direct interaction of dark matter particles. With the gradual increase of target fiducial mass and simultaneous reduction of background levels strategies, XENON experiment achieved very good results and promising perspectives for direct dark matter detection.

Tasks regarding analysis of experimental data acquired with the actual double-phase detector, as well as electric field simulations, development, assembly and tests of the next XENON1T detector and the regular participation in general maintenance and monitoring of the actual XENON100 prototype at LNGS, constituted the work plan of this PhD research activity and my contribution for optimizing the scintillation detection in XENON detectors.

The need to achieve extremely low sensitivities demands for innovation in all aspects of detector physics, such as reducing all sources of radioactivity background. The favored mode of operation for the liquid/gas Xe-based detector involves measuring both primary and secondary scintillation from particle interaction in the liquid. The ratio of these signals allows to clearly differentiate the majority of the background and WIMP events. The scintillation readout is, then, of utmost importance.

The scintillation signal amplitude before to be read by the photo-sensors is maximized also by the optimization of several parameters such as the detector target geometry, electrode meshes transparency, secondary scintillation gain uniformity and reflective material used to cover the non-photosensitive surfaces.

KEYWORDS: Dark matter, Direct detection, Double phase detector, Electric field, Liquid Xenon, LNGS, Noble gases, Simulations, TPC, WIMP

Resumo da Tese

CĂTĂLIN BALAN

Departamento de Física
Faculdade de Ciências e Tecnologia da Universidade de Coimbra, Portugal

Contribuição para a otimização da deteção de cintilação em detetores de dupla fase para deteção direta de matéria negra

Na última década, foram feitos grandes progressos no desenvolvimento dos detetores de deteção direta das partículas que constituem a matéria negra. Com estratégias do aumento gradual do volume do alvo e, simultaneamente, de redução dos níveis de fundo, a experiência XENON obteve resultados muito bons e perspetivas promissoras para a deteção de matéria negra.

Tarefas relativas à análise de dados experimentais adquiridos com o detetor de dupla fase em uso, assim como as simulações do campo elétrico, desenvolvimento, montagem e testes para o próximo detetor XENON1T, assim como a participação regular na manutenção geral e monitorização do protótipo atual XENON100 no LNGS, constituiram o plano de trabalhos para as atividades de investigação do presente doutoramento e a minha contribuição para a otimização da deteção de cintilação nos detetores da experiência XENON.

A necessidade de alcançar níveis elevados de sensibilidade, requer inovação em todos os aspetos físicos do detetor, assim como a redução de todas as fontes de radioatividade que contribuem para o fundo. O modo mais indicado de operação para os detetores com enchimento a Xe no estado líquido e gasoso envolve a medição da cintilação primária e da secundária provenientes da interação das partículas no Xe líquido. A razão entre estes dois sinais permite diferenciar claramente a maior parte dos eventos correspondentes as fundo dos eventos correspondentes a WIMPs. Deste modo, a leitura dos sinais correspondentes à cintilação é de extrema importância.

A amplitude do sinal de cintilação antes dos fotossensores é maximizada através da otimização de vários parâmetros, tais como a geometria do alvo do detetor, a transparência das grelhas dos elétrodos, a uniformidade do ganho em cintilação secundária e a utilização de material reflectivo para cobrir as superfícies que não são fotossensíveis.

PALAVRAS CHAVE: Matéria negra, Deteção direta, Detetores de dupla fase, Campo elétrico, Xenon líquido, LNGS, Gases nobres, Simulações, TPC, WIMP

CHAPTER I

Introduction

This thesis is related to the research conducted in the context of the XENON dark matter experiment. During my activity for XENON Collaboration, I have been involved in almost all the aspects related to the operation of actual XENON100 detector (monitoring cryogenic parameters, solving emergency situations, background data acquisition and processing, calibrations of the detector with external radioactive sources as well as procedures of xenon distillation for ^{85}Kr contamination) locally at LNGS, requiring continued attention 24h/day, 7days/week within a total of 140 days as a collaboration shifter. Data analysis for XENON100, as well as simulations for the next XENON1T detector required also special timing for ROOT programming learning and understanding of all the analysis techniques and theories involved in this direct dark matter detection experiment.

The technology of scaling up the target mass of liquid noble gas detectors and the simultaneous reduction in backgrounds lead to the detection of WIMP dark matter in the near future. Further, there are great advances in the field, and the next generations of detectors will have dramatically increased sensitivity to probe orders of magnitude deeper into the WIMP cross section. In particular, liquid noble gas detectors, which are easily scalable, already approached the ton scale with plans to go beyond as well.

The next phase of XENON dark matter experiment is a 1 ton fiducial detector. Simulations have been conducted for 1 ton scale to explore different options for the detector design, incorporating a 1m height and 1m diameter TPC, which after 10cm fiducial cut has a 1 ton liquid xenon target. Field simulations have been conducted to obtain the electric potential and trajectories of drifted electrons inside the TPC. The goal of the simulations was to find a detector design capable to create a uniform drift field.

The optimization of the scintillation detection requires research activities in both experimental and theoretical physics connected by a great dedication and pleasure for discovering and understanding better our Universe. A brief description of each chapter,

in order to understand better the correspondence between them and their relevance with the theme of the thesis, is presented below.

Chapter 2 is introducing the main subject of the thesis, *Dark Matter*, presenting the theoretical hypothesis and experimental ways of detection placing also the XENON experiment in the context of the international research.

Since XENON is a direct detection experiment, we should understand all the properties of the target and the response of the detection medium to the low-energy nuclear recoils. Chapter 3 will describe some of these important aspects.

The design of the XENON100 detector, the actual prototype of XENON Experiment still taking data, and its subsystems, as well as a subset of calibration procedures, make the content of Chapter 4. The purification of the detection medium, both of impurities that attenuate the charge signal and radioactive impurities, using high temperature getters or through cryogenic distillation, respectively, as well as and the electronic and nuclear recoil calibrations, seem to require special attention for the dark matter search.

Chapter 5 is presenting the blinded analysis details of the data acquired and the published results after the un-blinding procedure. The exponential dependence of the sensitivity to WIMPs with energy threshold makes clear the idea of continuing understanding the low-energy nuclear recoil response and scaling up the actual XENON100 noble gas detector to the next phase: XENON1Ton.

Chapter 6 is describing briefly the details of this new detector that is under the construction phase in the Hall B of Gran Sasso underground laboratory in Italy but focuses in the TPC's optimization studies through COMSOL simulations of the electric field.

The studies described in this thesis and all my contribution to XENON Experiment resulted, thus far, in the following 10 publications, as a co-author of XENON collaboration since 2011, for both XENON100 and XENON1T experiments:

XENON papers in International Journals:

1. The XENON Collaboration: E. Aprile et al. (C.Balan), *Conceptual design and simulation of a water Cherenkov muon veto for the XENON1T experiment*, arXiv:1406.2374v1 (2014), submitted to JINST
2. The XENON100 Collaboration: E. Aprile et al. (C.Balan), *First Axion Results XENON100 Experiment*, arXiv:1404.1455v1, Phys. Rev. D 90, 062009

[3] The XENON100 Collaboration: E. Aprile et al. (C.Balan), *Observation and applications of single-electron charge signals in the XENON100 Experiment*, arXiv:1311.1088v2, J. Phys. G: Nucl. Part. Phys. 41 (2014) 035201

[4] The XENON100 Collaboration: E. Aprile et al. (C.Balan), *Analysis of the XENON100 Dark Matter Search Data*, arXiv:1207.3458v2, Astropart.Phys. 54 (2014) 11-24

[5] The XENON100 Collaboration: E. Aprile et al. (C.Balan), *The neutron background of the XENON100 dark matter experiment*, arXiv:1306.2303v2, J. Phys. G: Nucl. Part. Phys. 40, 115201 (2013)

[6] The XENON100 Collaboration: E. Aprile et al. (C.Balan), *Response of the XENON100 Dark Matter Detector to Nuclear Recoils*, arXiv:1304.1427v2, Phys. Rev. D 88, 012006 (2013)

[7] The XENON100 Collaboration: E. Aprile et al. (C.Balan), *Limits on spin-dependent WIMP-nucleon cross sections from 225 live days of XENON100 data*, arXiv:1301.6620v2, Phys. Rev. Lett. 111, 021301 (2013)

[8] The XENON100 Collaboration: E. Aprile et al. (C.Balan), *The distributed Slow Control System of the XENON100 Experiment*, arXiv:1211.0836, 2012 JINST 7 T12001

[9] The XENON100 Collaboration: E. Aprile et al. (C.Balan), *Comment on "On the subtleties of searching for dark matter with liquid xenon detectors"*, arXiv:1208.5762v1, [astro-ph.CO] 28 Aug 2012

[10] The XENON100 Collaboration: E. Aprile et al. (C.Balan), *Dark Matter Results from 225 Live Days of XENON100 Data*, arXiv:1207.5988v1, Phys. Rev. Lett. 109, 181301 (2012)

CHAPTER 2

Welcome to the dark side of the Universe!

When we look up at the night sky, we see a tapestry of light – visible light emitted by all the stars in the Milky Way and the galaxies that surround it. We do also see light reflecting off the planets, which makes them shine brighter than many stars.

From this picture we may believe that we are actually seeing what the Universe it looks like. But, imagine observing a building from afar, a tall glass sky scrapper of the kind found in so many modern cities. In the middle of the night, there may be some lights on inside. And what we see is a disorganized patchwork, with some windows making up bigger islands of light, where whole floors are illuminated, and other windows emitting no more than pinpricks isolated in darkness.

What should look like a tall rectangular structure looks like a chaotic mess levitating in the darkness. In this case what we see is definitely not the whole picture. Something similar is happening when we look at a galaxy or even a cluster of galaxy.

A conservative and much more travelled route is that there is some strange form of matter in the Universe which we have yet to see directly. In this thesis we explore one of possible candidates for this unknown matter.

2.1 Dark Matter

Recent studies show that most of the universe is as yet undetected. Galaxies are not what they seem. They are bigger and heavier than they look. And we cannot see directly what makes them so heavy. One of those components is a new form of matter. This invisible mass is called *Dark Matter* and it is one of the most interesting subjects for the physicists today.

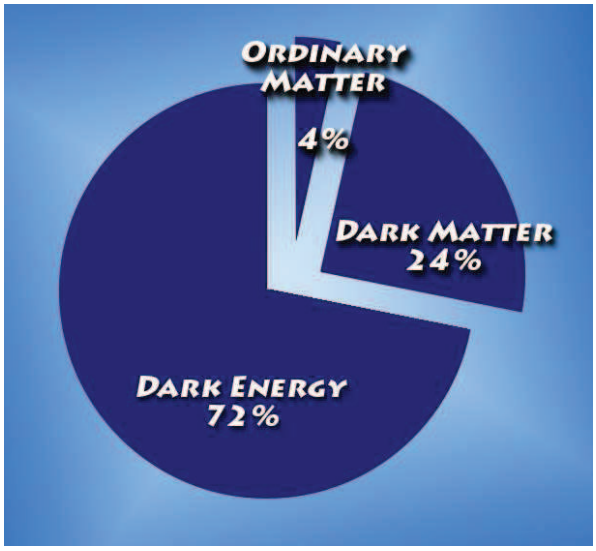

FIG. 2.1 – The Universe structure [*]

But this dark component cannot be the kind of matter of which stars, gas clouds and planets are made. Studies of the microwave radiation left over from the Big Bang suggest that such ordinary matter which we are familiar with and consist of standard model particles such as quarks and leptons, makes up only 4.6% of the Universe (see FIG. 2.1). The remaining is thought to be divided between *dark matter* (outweighing normal matter by five to one) and strange repulsive named *dark energy* [1]. Michael Turner, a cosmologist at the University of Chicago, Illinois, states that in the universe history, a "battle" of these 2 components (dark matter and dark energy) can be seen: dark matter reigned for the first ten billion years and shaped all the structure of Universe while about five billion years ago, the dark energy shut off the formation of structures and got the Universe accelerating.

This being the case, it now becomes very evident that if we are to gain a greater understanding of our universe, then we must find a way to detect and to determine the nature of this substance which so far eluded all detection efforts. In 1970, the idea that dark matter looks fundamentally different from other form of normal matter gained ground so, in 1980 began the first planning for underground detectors but, the field was only recently appreciated when the sensitivity has improved and competing experiments have emerged to attack into dark matter particle hunting from many angles.

2.1.1 Proofs of Dark Matter existence

2.1.1.1 Galaxy Clusters

The first observations and studies of Dark Matter came in the 1930s by Fritz Zwicky's search about the behavior of galaxies in the Coma Cluster [2]. His conclusion

that "dark matter is present with a much greater density than luminous matter" is confirmed by measurements of the galaxies velocities that underline an excess of mass on the cluster, more than he could see.

Coma cluster, for example, is so large and it is representative for the universe. It is composed of roughly 1000 galaxies. This is one of the objects that have been studied quite extensively by analyses of X-Ray gas temperature as well as studies of the constituent mass content of the cluster by X-Ray emission analysis and radial velocities of the member galaxies. The measurements of the amount of mass in stars, hot gas and total mass were reported by White et al. within a radius of $1.5h^{-1}Mpc$ [3]:

$$M_{star} = 1.0 \pm 0.2 \times 10^{13} h^{-1} M_{\odot}$$
$$M_{gas} = 5.4 \pm 1 \times 10^{13} h^{-5/2} M_{\odot}$$
$$M_{total} = (5.7 - 11) \times 10^{14} h^{-1} M_{\odot}$$

where $h \equiv \frac{H}{100km\, s^{-1} Mpc^{-1}}$ is the parameterized value of the Hubble Constant, H_0. The conclusion of this study is that the contribution of M_{star} and M_{gas} is between 13-26% which means that the dominant mass component of the cluster has no visible signature.

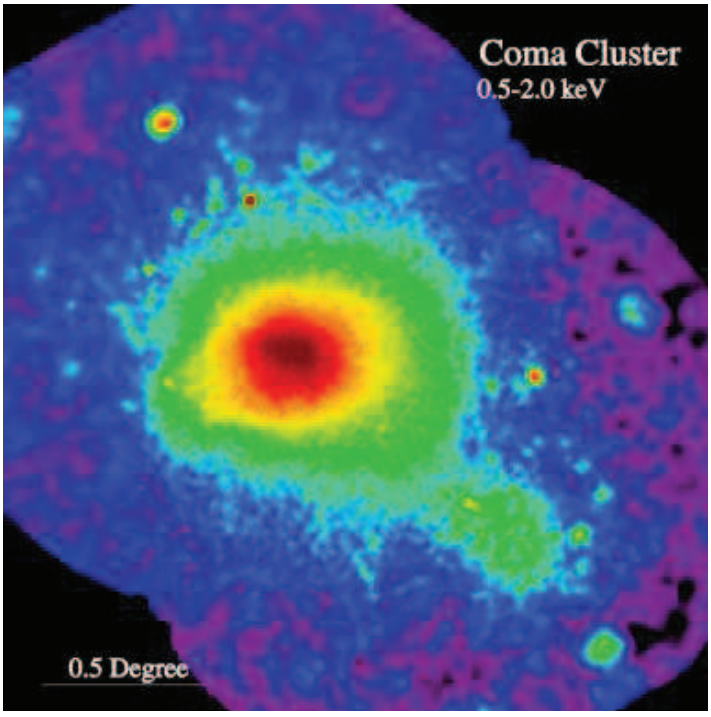

FIG. 2.2 – X-Ray image of Coma Cluster [**]

2.1.1.2 Galactic rotation curves of spiral Galaxies

The explanation from the *rotation curve of a galaxy* remains one of the leading proofs of dark matter existence today. This can be represented by a graph that plots the orbital velocity of the stars or gas in the galaxy as a function of distance from the center of the galaxy. Analyzing the curves, the galaxy rotation problem is the discrepancy between the observed rotation speeds of matter in the disk portions of spiral galaxies (FIG. 2.3 – solid line) and the predictions of Newtonian dynamics considering the known mass (FIG. 2.3 – dashed line). The discrepancy is due to the dark matter that permeates and extends into the galaxy´s halo (FIG. 2.3 – dashed & dotted line).

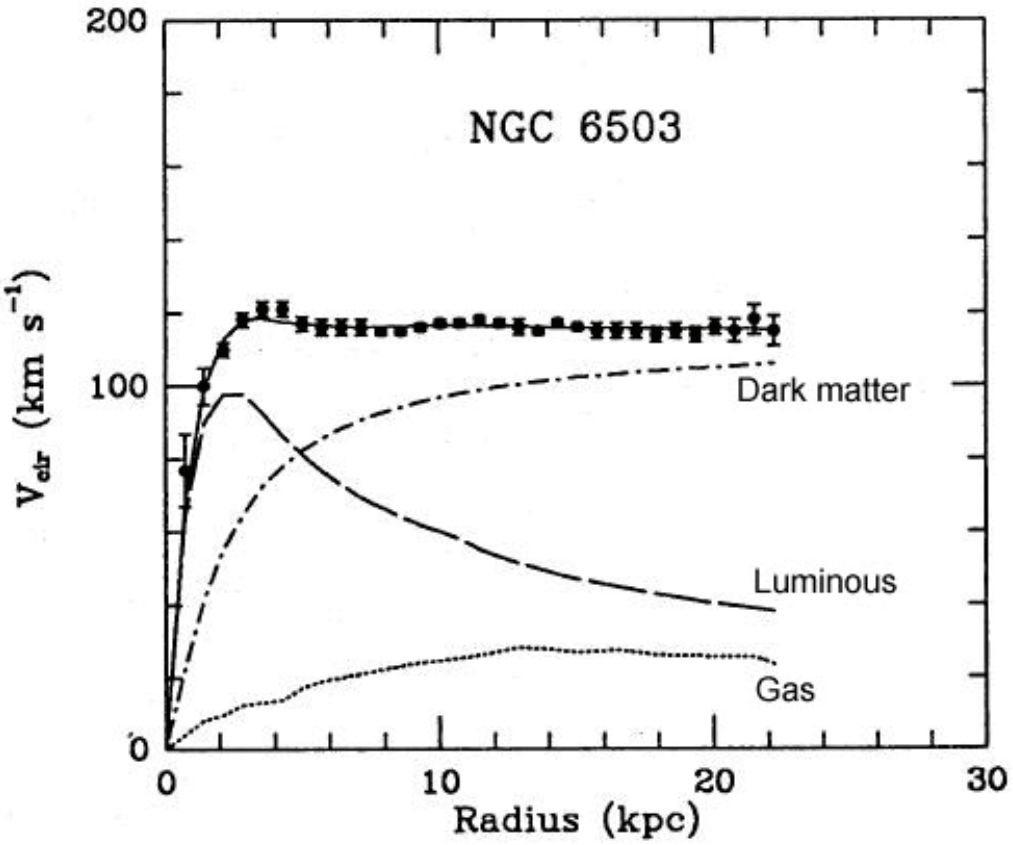

FIG. 2.3 – Rotation curve of a spiral galaxy NGC 6503. The points represent the rotation velocities measured as a function of distance from the center of the galaxy. The contributions to the rotational velocities due to the luminous and gas are represented by the dashed and dotted lines respectively [4]

The orbital velocity distribution should agree with Kepler law:

$$\frac{mv^2}{r} = m\frac{M(r)G}{r^2}. \qquad (2.1)$$

The equation 2.1 can be solved, so the velocity expression is:

$$v = \sqrt{\frac{M(r)G}{r}}, \qquad (2.2)$$

If $M(r)$ would be equal to M_{gal} for $r > r_{vis}$ then an absence of dark matter is justified. This means that the velocity would decrease as $\sqrt{\frac{1}{r}}$ once the radius r becomes greater than r_{vis} ; r_{vis} is the visible edge of the galaxy, M is the mass, r is the radius and v is the orbital velocity. This can be true only if the dominant matter component in the galaxy is characterized by the luminous matter observed in the galaxy. In the expression 2.2, $v(r) \sim constant$ for what can be measured, and this implies the dark matter existence with a density $\propto r^{-2}$ and the mass inside proportional with r.

2.1.1.3 Gravitational lensing of galaxies clusters

Nowadays, scientists believe that dark matter provides the scaffolding of all shapes of galaxy clusters and super-clusters. Big telescopes are built to map its distribution in the Universe [5]. So, going to the scale of galactic clusters even greater evidence of dark matter can be seen.

Clowe et al. used *weak lensing* observations made with Hubble Telescope to map the gravitational potential of 1E0657-588 cluster merger object [4]. An example of the measurement can be seen in the images below (FIG. 2.4). The phenomenon of focusing photons in all bands caused by dense localization of matter is known as *gravitational lensing*. In figure below (FIG. 2.4), the green contour is mapping the locations of lensing. Lensing in the visible band causes objects in the lensing path to appear brighter than they are. In the analysis of *weak lensing* small systematic distortions of the elliptical background shape of galaxies are used in terms of mass distribution reconstruction in the lensing foreground cluster. On the other hand, the *strong lensing* is a case of gravitational lensing where a single item in the source plane consists of many images and arcs.

2.1.1.4 Cosmic Microwave Background (CMB)

CMB represent a very uniform background of photons in all directions on the sky with a spectral distribution comparable to a black body spectrum at 2.73K. At the beginning, the temperature of the Universe was high for matter to be ionized and photons propagate freely. As the universe expanded and cooled matter de-ionized and photons could propagate and decoupled from the matter. What is detected today is the microwave length of free photons that have ‘red-shifted’ as the universe continues to expand up to now.

By measuring the precise temperature of CMB today, information of energy density on decoupling times can be found. This is what the Wilkinson Microwave Anisotropy Probe (WMAP) contains (see FIG. 2.5): precise measurements of CMB on entire sky, yielding maps of mass distribution in the early Universe, both total matter density and baryonic matter density. The analysis of all the data collected by WMAP in 7 years [6] shows that matter component is $\Omega_m h^2 = 0.1265 \pm 0.008$ and the baryonic component is $100\Omega_B h^2 = 2.23 \pm 0.074$ so, baryonic matter that matches luminous mass measurements, only contributes 18% from total matter density in the universe. The remaining matter must be non-baryonic so, non-luminous.

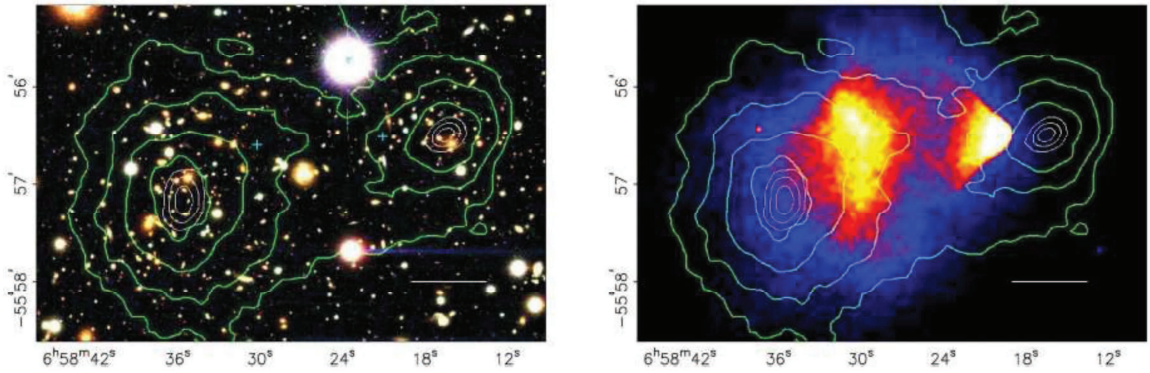

FIG. 2.4 - Map of the gravitational potential of the Bullet Cluster 1E0657-558 from [4]

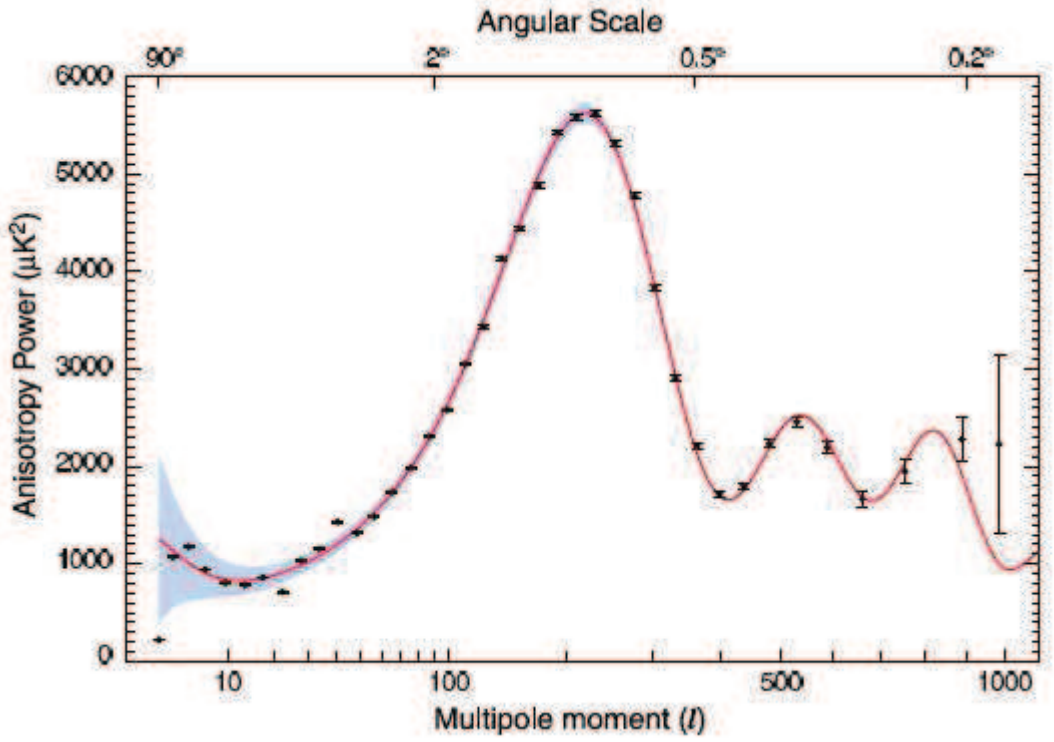

FIG. 2.5 - Angular Spectrum of the CMB Anisotropy [6]

Combining all the information collected by WMAP, observational evidence from galactic rotation curves, gravitational lensing measurements and all the others evidences of dark matter, the standard cosmological model show the universe composition of 4% ordinary matter (17% from total matter), 24% dark matter and remaining 72% dark energy (FIG. 2.1).

2.1.2 Dark Matter candidates

From many of the dark matter candidates: from brown dwarfs to black holes and even magnetic monopoles, three of the most motivated examples will be discussed in this section.

2.1.2.1 Baryonic particles

This type of dark matter candidate represents matter composed of quarks and electrons but does not radiate strongly in the electromagnetic spectrum. Examples of this category are the *primordial black holes* that have significantly reduced mass compared to standard black holes [7]. Name of *primordial* came because they formed the prior of Big Bang Nucleosynthesis (BBN) onset.

2.1.2.2 The axions and the failed neutrino candidate

Axions, particles with very small mass ($\sim 10^{-5} eV$), were originally proposed by Wilczek [8] to solve the *Charge-Parity* problem of *Quantum Chrome Dynamics* (QCD).

Other particles that have mass are not considered to be viable Cold Dark Matter particle. For example the neutrino is out of the candidates because it is a relativistic particle. With a high speed of moving it is impossible to form aggregates. Dark matter particles form structures in the universe as gravitational centers where luminous matter can condense. Neutrinos interactions with other particles at very high energies, allow them to redistribute their energy in such a way as to always be in thermal equilibrium. A value of $\Omega_\nu < 0.04$ much smaller than $\Omega_{DM} < 0.25$ assumed to dark matter abundance was found by the observations from Sloan Digital Sky Survey (SDSS) [9], WMAP and 2 degree Field Galaxy Redshift Survey (2dFGRS) [10]. This is why neutrino is not considered dark matter particle.

Axions, on the other hand, would be very weakly interacting and would never have had the opportunity to reach thermal equilibrium. Scientists considered that axions have been created non-thermally, in a very cold state, with low velocities and would behave like very massive particles and thus they are non-relativistic. They would clump and gravitate toward each other and provide a viable dark matter candidate.

The axions interactions make it difficult to detect. An experimental strategy in which a cavity is subjected to a static magnetic field can be used. Axions would be very light so we would expect to have very large number of them, even in a small region of space. They interact with the magnetic field and decay into microwave photons through a process known as Primakov effect. Scanning then the cavity it would be possible to catch any possible decay signature. Details on the detection of axions by X-Ray conversion in the presence of strong magnetic field can be read in reference [11].

2.1.2.3 Supersymmetric particles

Following the success of particle physics in constructing a unified theory of the electromagnetic and weak forces, beginning with 1970s, many ideas have emerged on how to combine them with the strong force into one simple picture, postulating a new symmetry named *SUperSYmmetry (SUSY).*

Supersymmetry is a fundamental symmetry between fermions and bosons. These two behave very differently: while bosons like to occupy states very similar to each other, fermions are not allowed to do this, because of the Pauli's exclusion principle. In the standard model, all the forces are bosons while almost all the fundamental particles, except the Higgs particle are fermions. So, in the super-symmetrical nature, for each of the fermions there is a partner or 'superpartner', which is a boson.

Although the fundamental theory may indeed be super-symmetrical, the symmetry is broken at the energies where we live and create experiments. This happens in the standard model of the electromagnetic and weak forces. In this case, the super-symmetrical partners are much heavier than the particle we 'see' so, we will need to perform experiences at very high energies in order to create these particles. Then the super-symmetrical theory become a viable candidate and host for new particle, one or more, that could account for dark matter.

One example of dark matter candidate generated by supersymmetry is the *neutralino*, a heavy, long-lived particle. Such particles would have to be heavy enough so represent an appreciable contribution to the mass density in the universe. Long-lives seem to have not decayed away by today. Neutralinos would be very weakly interacting and constantly streaming through normal matter. The permeability for this form of dark matter would make it extremely hard to detect, requiring for very sensitive experiments. An experiment which can detect dark matter should be very sensitive to any other particle on the Earth. The trick then is to discriminate, to select, the dark matter signal from the irrelevant signals due to everything else.

One of the main unsolved problems of cosmology is what dark matter is or how to see it? Many other theories have merits, but we take this one to test the validity and

behavior of one such weakly interacting massive particles (WIMPs), using the most sensitive experimental technique that will be presented in detail in the next sections.

2.2 The WIMP

Since no Standard Model particle has the right properties to be a dark matter particle, the work purpose of this thesis is to contribute to a detailed analysis of one such theory and test experimentally its validity. A motivated candidate is WIMP (Weakly Interacting Massive Particle), a stable particle arising naturally in theories with extra dimensions or supersymmetry.

These supersymmetric WIMPs have interaction cross sections of approximately weak strength. Their interactions produce fermion – anti-fermion pairs, gauge bosons of the weak interactions or the Higgs Bosons. At the beginning, WIMPs were part of the *primordial soup* composition along with the standard model particles, kept in thermal equilibrium by constant creation – annihilation process (FIG. 2.6).

While the ambient of the Universe dropped below the mass of the WIMP ($kT \ll m_\chi c^2\ time \geq 10^{-35} s$) they began to drop out of thermal equilibrium. While the universe expand and cools quickly, the weakness of their annihilation cross section led to an essential halt of annihilation, effect known as *Freezout* (see FIG. 2.7) [12]. The result of this effect is the *Relic Density* of WIMPS in the universe.

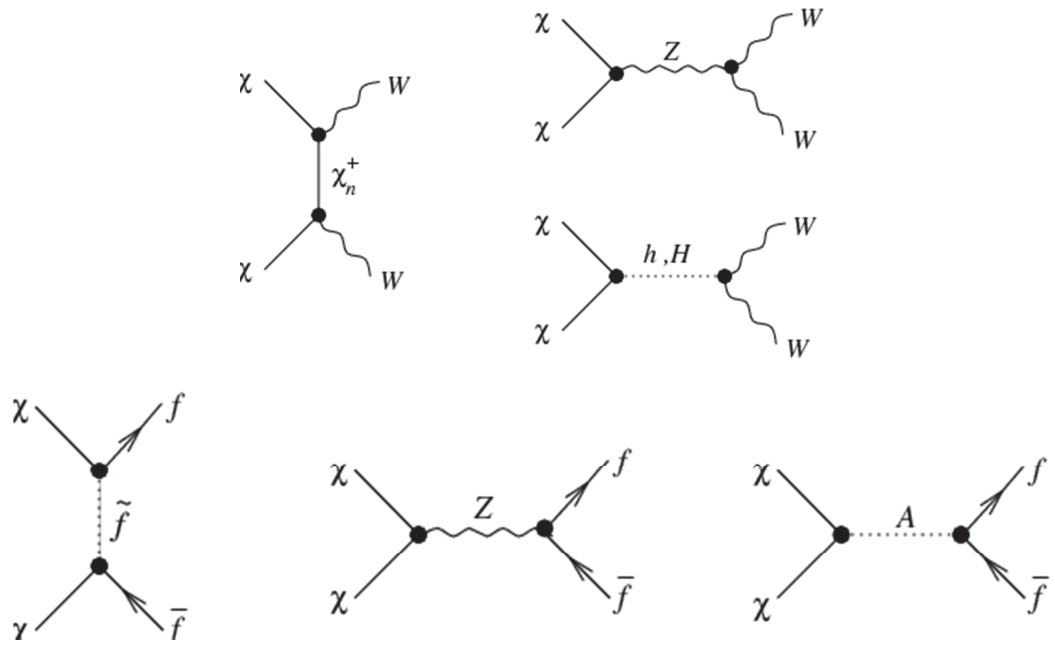

FIG. 2.6 - Some of the most important Feynman diagrams for neutralino annihilation [13]

Two general branches, regarding WIMPs experimental searches, are used; one of them is the indirect look for the signature of dark matter annihilation in the universe (Fermi, Veritas and AMS-2 experiments) but, in this work we will focus on the last type of experiments looking for direct search of dark matter interactions using a target material in a detector. These experiments with recent significant progress are well developed. The WIMPs are neutral and we are expecting them to interact with the target material nuclei (nuclear recoil interaction, NR) while, the main background comes from electromagnetic interactions of gammas and electrons with the atomic electrons (electron recoil interaction, ER). So, the background needs to be reduced as much as possible to increase the detector sensitivity to WIMPs.

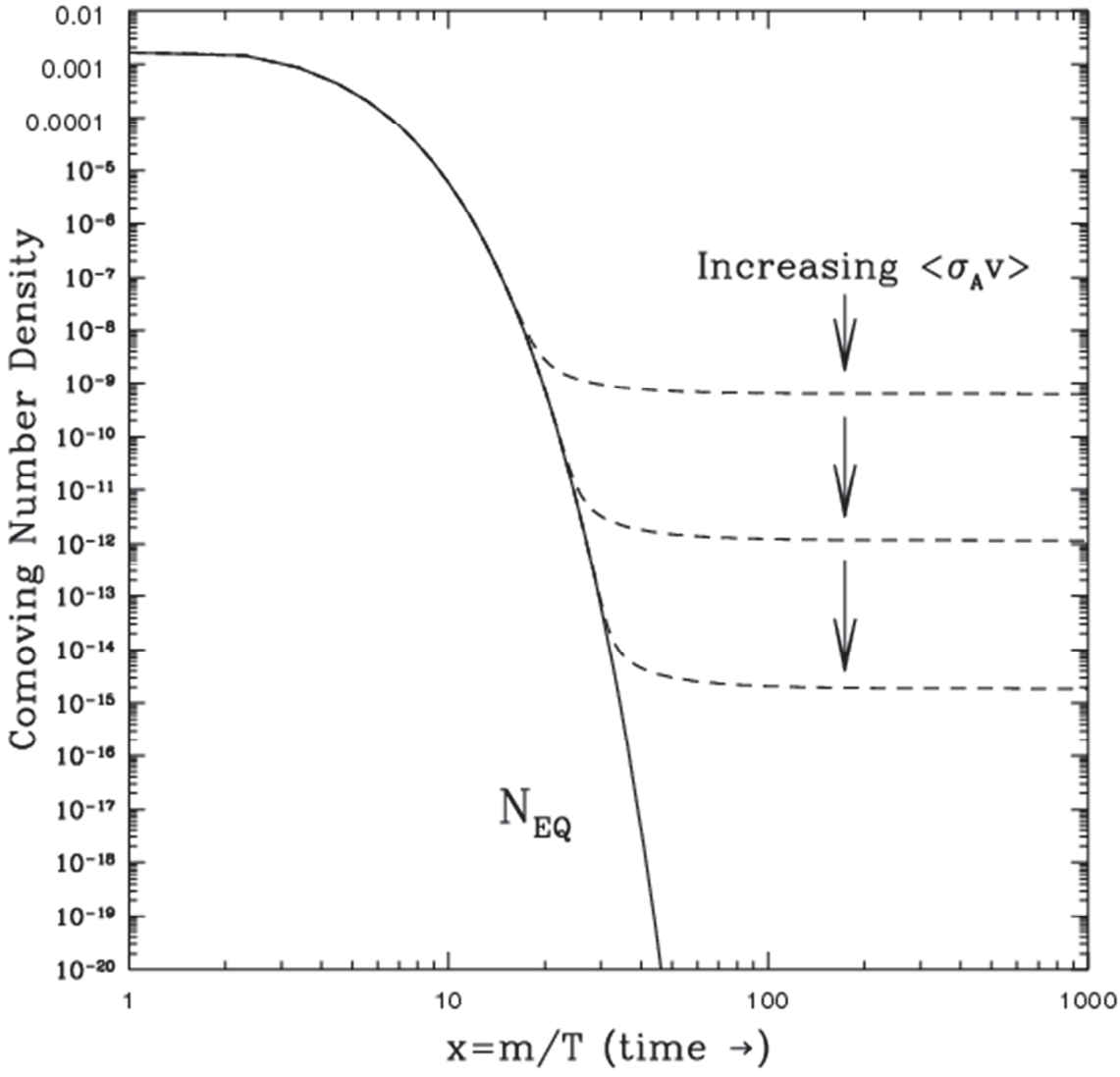

FIG. 2.7 – Comoving Number Density as a function of WIMP Mass – Temperature Ratio. The solid lime represents the equilibrium abundance of the WIMPs in the early universe. The dashed lines show the effect of the interaction cross section. Relic density decrease with increasing interaction cross section [12]

2.2.1 WIMP interaction

To study the interaction in a target for WIMPs implies an analysis on the elastic spin dependent and spin independent components with an experimental system designed to measure one or the other, and in some cases both of these components.

In any target we are writing the differential interaction rate as:

$$\frac{dR}{dQ} = \frac{2\rho_0}{m_\chi}\int_{v_{min}}^{v_{esc}} \frac{d\sigma}{d|q|^2} v f(v) dv, \qquad (2.3)$$

where:

- m_χ is the WIMP mass;
- v is the WIMP speed in the galaxy;
- $f(v)$ is the speed distribution of WIMP in the galaxy
- $\rho_0 = 0.3\ GeV/cm^3$ is the local dark matter density;
- $v_{esc} = 544\ km/s$ is the WIMPs escape velocity in the Milky Way;
- $v_{min} = \sqrt{\frac{Qm_N}{2m_r^2}}$;
- $Q = \frac{|q|^2}{2m_N}$ is the recoil energy;
- m_N is the nucleus mass;
- $\frac{d\sigma}{d|q|^2}$ is the differential cross section.

In case of the spin independent interaction due to a coherent scatter off of the nucleus, the differential cross section is given by

$$\frac{d\sigma}{d|q|^2} = \frac{\sigma_0}{4m_r^2 v^2} F^2(Q), \qquad (2.4)$$

where:

- σ_0 is the nuclear scattering cross section for the 0 momentum transfer;
- m_r is the reduced mass of the WIMP nucleus system;
- $F^2(Q)$ is the nuclear form factor.

In general the speed distribution is chosen to be a Maxwellian function. Taking into account the relative motion of earth and sun in the galaxy, v_e and the escape velocity of WIMPs, the integral will become

$$\int_{v_{min}}^{v_{esc}} \frac{f(v)}{v} dv = \frac{2}{v_0\sqrt{\pi}} \frac{k_0}{k_1} \times \left[\frac{\sqrt{\pi} v_0}{4v_e}\left(erf\left(\frac{v_{min}+v_e}{v_0}\right) - erf\left(\frac{v_{min}-v_e}{v_0}\right)\right) - exp\left(\frac{v_{esc}^2}{v_0^2}\right)\right], \qquad (2.5)$$

where $v_o = 220\ km/s$ is the sun speed relative to the center of the galaxy and

$$k_1 = k_0 \left[er\,f\left(\frac{v_{esc}}{v_0}\right) - \frac{2v_{esc}}{v_0\sqrt{\pi}} exp\left(-\frac{v_{esc}^2}{v_0^2}\right)\right], \qquad (2.6)$$

The cross section for 0 momentum is given by

$$\sigma_{0SI} = \frac{4m_r^2}{\pi}\left[Zf_p + (A-Z)f_n\right]^2, \qquad (2.7)$$

where

- Z is the number of protons in the nucleus;
- A is the number of nucleons;
- f_p is the proton coupling;
- f_n is the neutron coupling.

For the approximation $f_p = f_n = f_N$ the relation (2.7) will be written in terms of proton section σ_p for coherent scattering

$$\sigma_0 = A^2 \left(\frac{m_r}{m_p}\right)^2 \sigma_p, \qquad (2.8)$$

So, the differential interaction rate (2.3) for spin independent scatters will be written as

$$\frac{dR}{dQ} = \frac{\rho_p \rho_0 A^2}{\sqrt{\pi} v_0 m_\chi m_p^2} F^2(Q) \frac{k_0}{k_1} \times \left[\frac{\sqrt{\pi} v_0}{4v_e}\left(er\,f\left(\frac{v_{min}+v_e}{v_0}\right) - er\,f\left(\frac{v_{min}-v_e}{v_0}\right)\right) - exp\left(\frac{v_{esc}^2}{v_0^2}\right)\right], \qquad (2.9)$$

and the enhancement factor has the form of expression 2.10:

$$C_N = \frac{8}{\pi}\left(f_p\langle S_p\rangle + f_n\langle S_n\rangle\right)^2 \frac{J+1}{J} \qquad (2.10)$$

If we write $\lambda \equiv \frac{1}{J}\left(f_p\langle S_p\rangle + f_n\langle S_n\rangle\right)$ then we obtain the following expression:

$$C_N = \frac{8}{\pi}\lambda^2 J(J+1) \qquad (2.11)$$

In the table below (TABLE 2.1), the values of $\lambda_{p,Z}^2 J(J+1)$ for sample target materials are included, where J is the total nuclear spin and $\langle S_p\rangle$ and $\langle S_n\rangle$ are the expectation values of spin for the protons and neutrons in the target nucleus.

TABLE 2.1 – Expectation values for the proton and neutron spin in target materials, in accordance with [14, 15, 16]

Nucleus	J	*Odd Nucleon*	$\langle S_p \rangle$	$\langle S_n \rangle$	$\lambda^2_{p,Z}\, J(J+1)$
^{7}Li	3/2	p	0.497	0.004	0.406
^{19}F	1/2	p	0.441	-0.109	0.855
^{23}Na	3/2	p	0.248	0.020	0.089
^{73}Ge	9/2	n	0.009	0.372	0.105
^{125}Te	1/2	n	0.001	0.287	0.178
^{127}I	5/2	n	0/309	0.075	0.084
^{129}Xe	1/2	n	0.208	0.359	0.232
^{131}Xe	3/2	n	-0.009	-0.227	0.057

2.2.2 Nuclear Recoil Spectrum and Annual Modulation

The differential scattering rate in any detector for different target nuclei for the WIMP mass and a cross section can be calculated. For low energies, the heavy targets, like Xenon, give the largest rate but, for high energies more sensitive is germanium (targets with lower mass) (FIG. 2.8). The figure represents the computation for nuclear recoil spectrum for a particular target medium. The plot is represented in units of $[events\ kg^{-1}\ day^{-1}]$.

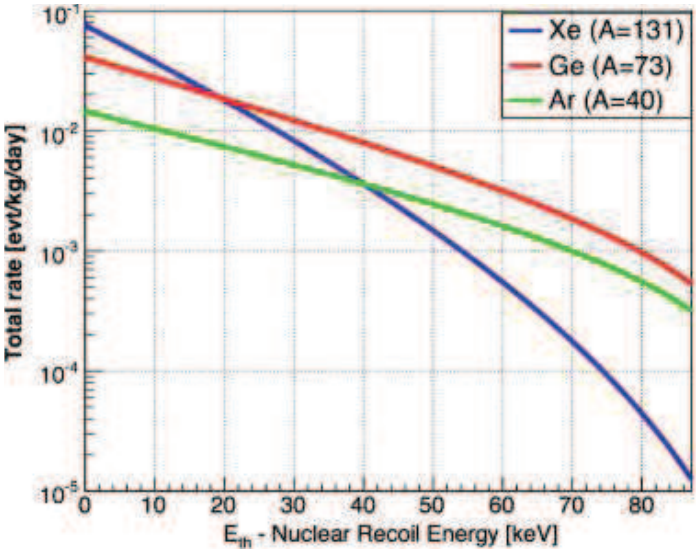

FIG. 2.8 – Spin independent scattering rate for several targets [17]

Another subject to be addressed is the prediction of the annual modulated WIMP recoil signal since the velocity of the Earth relative to the velocity of the WIMP will change in time. Assuming Maxwell distribution of WIMP velocities we can write:

$$f(v, v_e) = e^{-\frac{(\vec{v}+\vec{v_e})^2}{v_0^2}} \qquad (2.12)$$

$$v_e \cong 244 + 15\sin(2\pi\tau)\ [km\ s^{-1}] \qquad (2.13)$$

where

- v_e is the velocity of the Earth

- τ is the elapsed time $[years]$

Accurate quantifications are given by Lewin and Smith in [18].

2.2.3 WIMP direct detection and experiments

Assuming that a typical WIMP has a mass 100 times heavier than a proton, models of dark matter in the Milky Way predict that ten billion WIMPs pass through one meter of Earth every second. Since the WIMPs have such a small interaction cross section with ordinary matter, their interaction would be quite rare. A very sensitive detector would be capable to direct detect these particles by measuring the nuclear recoils interactions. Depending on the detection medium, that should be dense, the energy could be measured from photons, ionization or scintillation signals.

The direct detection implies also an undergrounded operation in terms of reducing as much as possible the nuclear recoils produced by cosmic ray muons. For example, the flux of muons at the surface of the Earth is $100\ muons\ m^{-2}s^{-1}$ in the National Laboratory at Gran Sasso Italy, while inside underground laboratory, where XENON experiment is located the muon flux is reduced to $1\ muon\ m^{-2}s^{-1}$.

Presently there are a reasonable number of experiments running and/or being designed to detect dark matter directly. The main experiments in the field are now testing the regions where many SUSY dark matter theories predict the existence of neutralino since this particle is yet definitively detected. In the figure below, FIG. 2.9, the last plot of spin independent cross section is represented as a function of WIMP mass for many of the experiments searching for dark matter.

The cross section sensitivity of each experiment is defined by the limit curve as a function of the WIMP mass. As shown in the figure below, best results regarding the spin independent search had been achieved by LUX, XENON and CDMS collaborations. All these experiments look for signatures of nuclear recoils, which are characteristic of WIMPs coherently scattering off the target material nucleus.

The ultimate sensitivity of XENON collaboration for spin independent WIMP-nucleon scattering it was $2 \times 10^{-45} cm^2$ at $55 GeV/c^2$ WIMP mass after analysis of last

225 Live Days of data [19]. XENON, LUX and ZEPLIN IIIexperiments use a dual-phase xenon time projection chamber (TPC) that monitors the light and charge signals of interactions within the xenon. The charge to light ratio gives a discrimination of electron recoils and position reconstruction based on the charge drift time and on the 2D-scintillation readout.

Some of the advantages of the liquid xenon detectors are that they are easily scalable and have high density of the target. Cross sections exclusion limits as low as $10^{-47}cm^2$ are expected for the future XENON1T detector, LXe double-phase TPC with a fiducial mass of 1000kg, which is already in construction phase in the same underground laboratory from Italy, where the previous detectors XENON10 and XENON100 (still ongoing) hunt for WIMPs since 2005 [19, 20].

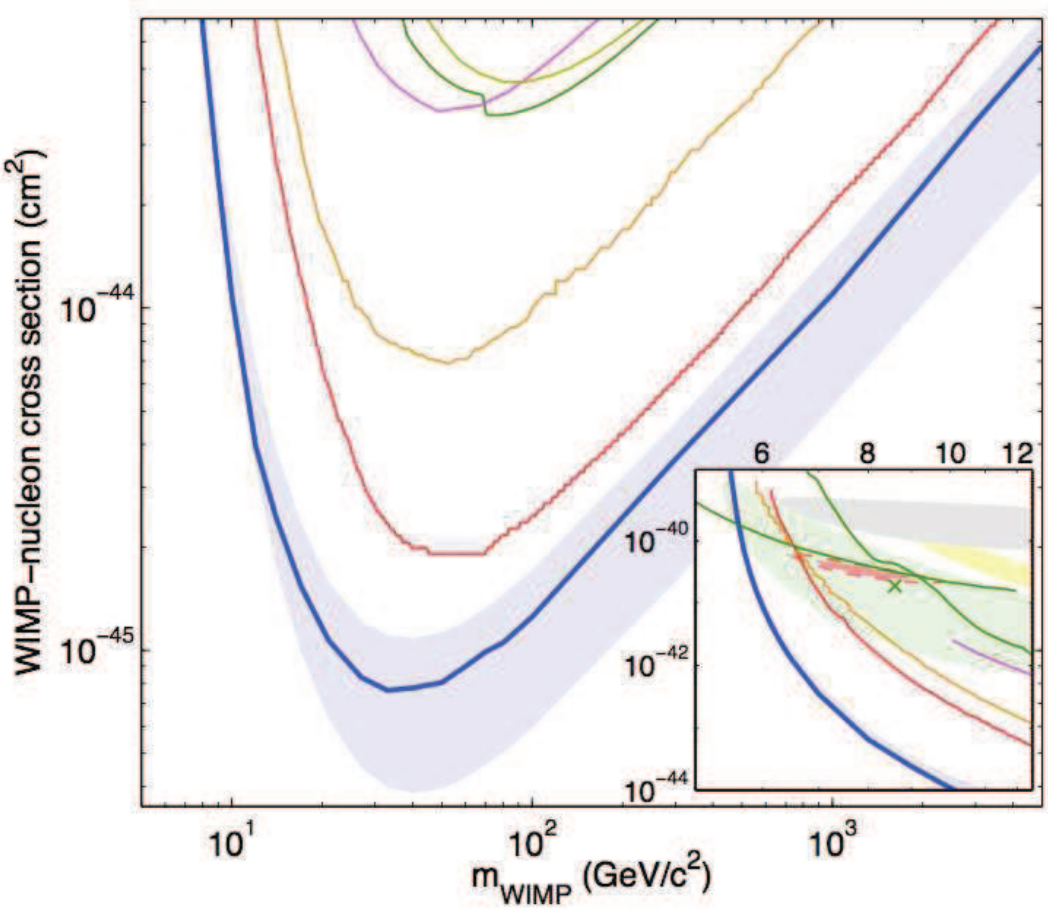

FIG.2.9 – Cross section limit as a function of WIMP mass. The most recently established limit is from LUX Experiment (blue line) corresponding to a value of $7.6 \times 10^{-46}cm^2$ at $33GeV/c^2$ WIMP mass; the blue band represents the $\pm 1\sigma$ expectancy of the blue curve; the other various lines represent the sensitivity achieved by the other experiments as following: red line for 225 live days of XENON100 Experiment, orange line for 100 live days of XENON100 Experiment, green line for CDMS II Experiment, magenta line for ZEPLIN III Experiment, and dark yellow line for Edelweiss II Experiment [21]

CHAPTER 3

Xenon as WIMP detection target

The detectors aimed to detect WIMPs are being constructed from a variety of materials. Dual phase Xenon has several advantageous properties to allow competitive dark matter searches. In this chapter I will underline all the qualities of this detection target, from physical properties up to more specifically characteristics related to its capacity to transform the energy into a measurable signal and also its profound ability of self-shielding the incident irradiation.

3.1 Xenon – physical properties

Xenon is one of the noble gases with a very small concentration in the Earth atmosphere (~0.1ppm) and also the heaviest non-radioactive noble element. Xenon is an expensive gas, its price is ~2500$/kg, and it is obtained in industry by the air liquefaction and separation into oxygen and nitrogen. The resulting oxygen mixture contains both Krypton and Xenon gases that are separated by distillation.

There are a number of properties that make Xenon a good choice of detection medium. Liquid Xenon (LXe) has a high density and a high atomic number (see table 3.1). As a liquid it provides a homogeneous volume and moderate cryogenic requirements, and as a result, the volume of the detectors is scalable to large mass. Since the WIMP nucleon cross section scales with A^2 (see previous chapter) Xenon is favorable for WIMP interactions providing a low recoils energy threshold. As a benefit of its high atomic number, Liquid Xenon is a very good absorber of energy from charged particles and γ-ray photons. The table below shows some of the important properties of liquid Xenon, related to particle detection.

TABLE 3.1 – Physical properties of Liquid Xenon

Material properties	*Value and Unit*	*Conditions*
Atomic Number	54	
Atomic Weight $\boldsymbol{A}$	$131\,\frac{g}{mole}$	
Boiling Point $\boldsymbol{T_b}$	$165.1\ K$	$1\ atm$
Melting Point $\boldsymbol{T_m}$	$161.4\ K$	$1\ atm$
Liquid Density $\boldsymbol{\rho}$	$2.98\ \frac{g}{cm^3}$	More useful if above $161.4\ K$
Radiation Length $\boldsymbol{X_0}$	$2.77\ cm$	In liquid
Refractive Index	$1.6 \div 1.72$	In liquid at $178nm$

TABLE 3.2 – Abundance of Xe isotopes [22]

Isotope	*Abundance (%)*	*Isotope*	*Abundance (%)*
^{124}Xe	0.096	^{131}Xe	21.18
^{126}Xe	0.090	^{132}Xe	26.89
^{128}Xe	1.92	^{134}Xe	10.44
^{129}Xe	26.44	^{136}Xe	8.87
^{130}Xe	4.08		

Xenon has no long lived radioactive isotopes and can be made extremely radio-pure. This makes Xenon an attractive detection medium for rare searches. The isotopic composition of natural Xenon contains nine stable isotopes. Two of these isotopes, ^{129}Xe and ^{131} Xe, have high abundance and non-zero nuclear spin, and thus these isotopes can be used to probe the WIMP spin dependent interaction. Table 3.2 contains the abundance values of all nine isotopes of natural xenon composition.

3.2 Interaction processes in LXe

It is known that liquid Xenon is a good scintillator, emitting UV photons at $178nm$. When a particle interacts with the Xenon target, the transferred energy is

split between *ionization* and *excitation* processes. In the absence of an electric field, the ionization component *recombines,* and along with the excitation component, emits the UV photons through the excimer state as it decay back to the ground state. The resulting scintillation light is not absorbed by Xenon atoms, so it can be collected by photo multiplier tubes (PMTs). Some of the ionization components does not recombine if the electric field is applied so, an independently collection from the light is allowed [23].

Another very important characteristic of LXe that gave its importance as very effective detection medium is the stopping power for electronic interactions, so the detection medium itself acts as a shield from external radiation, due to its high density. This means that in the center of the target can be defined an inner volume with a very low interaction rate called *fiducial volume*, a volume that will exclude most of the background interactions.

3.2.1 Types of interactions in LXe

3.2.1.1 X-ray and γ-ray interactions

X-rays and γ-rays interact with Xe atoms through photoelectric absorption, Compton scattering and pair production. These processes occur with formation of energetic electrons and positrons, and will lose energy by excitation and production of excited atoms and electron-ion pairs. Regarding the Compton case, the scattered γ-ray will continue the energetic exchange by subsequent interactions. In the section 3.2.2.2 the effects of this kind of interactions in xenon are explained.

3.2.1.2 Neutron interactions

One of the remarkable consequences of quantum mechanics is that matter can have both particle and wave – like nature. The neutron is no exception from this. In neutron scattering experiments, neutrons behave as particles when they are created, as waves when they scatter and again as particles when they are detected [24].

Since the neutron interactions consist in an important background for dark matter detection, below are described several of its properties useful also to understand better the data analysis performed in XENON experiment presented in chapter 5.

The neutron is a nuclear particle with a mass rather close to that of the proton:

$$m_n = 1.675 \times 10^{-27} kg \qquad (3.4)$$

The neutron does not exist naturally in free form, but decays into a proton, an electron and an anti-neutrino.

The neutron life-time $\tau = 886s$ is much longer than the time of the neutron within a scattering experiment, where each neutron spends merely a fraction of a second. The neutron is electrically neutral but still possesses a magnetic moment:

$$\mu = \gamma \mu_N \qquad (3.5)$$

where $\gamma = -1.913$ is the neutron magneto-gyric ratio and the nuclear magneton is given by

$$\mu_N = \frac{e\bar{h}}{m_p} \qquad (3.6)$$

where $\bar{h}$ is Plank reduced constant, $\bar{h} = \frac{h}{2\pi}$ and m_p is the proton mass.

The neutron magnetic moment is coupled anti-parallel to its spin, which has the value:

$$s = \frac{1}{2} \qquad (3.7)$$

The neutron interacts with nuclei via the strong nuclear force and with magnetic moment via the electromagnetic force. Consequences of these interactions are scattering and absorption of neutrons.

Neutrons can be produced in a number of ways, e.g. as products of cosmic rays or radioactive decay of heavy nuclei.

For the understanding of neutron scattering we need to introduce a term which describes the scattering of a neutron beam [25]. The flux of a neutron beam is defined as:

$$\Psi = \frac{number\ of\ neutrons\ impinging\ on\ a\ surface\ per\ second}{surface\ area\ perpendicular\ to\ the\ neutron\ beam\ direction} \qquad (3.8)$$

Since a neutron has no charge, it can easily enter into a nucleus and cause a reaction. Neutrons interact primarily with the nucleus of an atom, except in the special case of magnetic scattering where the interaction involves the neutron spin and the magnetic moment of the atom. Unlike the proton, interactions with the atomic electrons are not significant so that only neutron-nucleus reactions need to be considered.

Neutron reactions can take place at any energy, so one has to pay particular attention in the energy variation of the interaction cross section. For a given energy region, not all the possible reactions are equally important. Which reaction is important depends on the target nucleus and the neutron energy.

The most important types of neutron interactions are:

$(n, n) -$ *elastic scattering*; there are two processes, potential scattering which is neutron reaction at the surface of the nucleus (no penetration) as in a billiard ball – like

collision, and resonance scattering which involves the formation and decay of a compound nucleus;

(n,γ) – *radiative capture*; the incident neutron enters the target nucleus forming a compound nucleus. The compound nucleus then decay to its ground state by gamma emission.

(n,n') – *inelastic scattering*; this reaction involves the excitation of nuclear levels.

$(n,p),(n,\alpha),\ldots$ – *charged particle emission*;

(n,f) – *fission*; one of the most important interactions, in which the nucleus that absorbs the neutron actually splits into two similarly sized parts.

Elastic scattering is the simplest process in neutron interactions. This is an important process because it is the primary mechanism by which neutrons lose energy; from the instant they are emitted as fast neutrons in a fission event to when they appear as thermal neutrons. In this case there is no excitation of the nucleus. Whatever energy is lost by the neutrons is gained by the recoiling target nucleus. The type and nature of reaction varies with neutron energy. Elastic scattering and radiative capture reactions have no threshold for any target nucleus and are therefore dominant in the low energy region.

Inelastic scattering is the process by which the incoming neutron excites the target nucleus, so it leaves the ground state and goes to an excited state and energy above the ground state. In the case of scattering, the only way energy can be supplied is through the kinetic energy of incoming particle (neutron). If we want to know what is the minimum energy required for the reaction, the threshold energy, we look to the situation where no energy is given to the outgoing particle, so, the minimum kinetic energy required for reaction is always greater than the excitation energy of the nucleus.

Neutron interactions that produce low energy gamma rays are useful to calibrate large volume LXe detectors (see more information in the chapter 4). Neutron inelastic interactions do not constitute a background for the dark matter search because the nuclear recoils are accompanied by gamma rays energies out of the region of interest.

On the other hand, the elastic interactions represent an important background for WIMP searches and its occurrence should be reduced as much as possible. These interactions are produced by fast neutrons that are multiple scattering in large volume targets and can be rejected by defining specific cuts (see more information in data analysis section from chapter 5).

3.2.2 The measurable signal

As mentioned earlier, one of the most important properties of Liquid Xenon as target is its ability to transform the absorbed energy into a detectable and measurable

signal. This section presents the principles of signal production by the scintillation and ionization processes.

3.2.2.1 The scintillation signal (primary scintillation)

The scintillation signal is produced after the creation of the excited atoms Xe^* and the electron-ion pairs $Xe^+ + e^-$. The excited atoms can create the excimers Xe_2^* (excited molecular states), by colliding with Xe atoms. The excimers decay to the ground state and produce the scintillation light $h\nu$:

$$Xe_2^* \rightarrow 2Xe + h\nu \qquad (3.10)$$

Xe is one of the fastest scintillators; the spectrum of LXe scintillation photons is in the vacuum ultraviolet (VUV) range at 178nm that corresponds to an energy of 7eV and 13nm FWHM [26].

The production of the scintillation signal depends on many factors and different types of ionizing radiation in LXe. The electric field is reducing the scintillation yield because the recombination is reduced.

In case of a complete recombination process, i.e. one excited atom produces one scintillation photon and the recombined electron-ion pair produces one scintillation photon, the average energy to produce a photon, W_{ph} can be written as:

$$W_{ph} = \frac{E}{N_i + N_{ex}} \qquad (3.11)$$

where N_i is the number of electron-ion pairs, N_{ex} is the number of excited atoms and E is the recoil energy that can be defined as

$$E = N_i W_i \qquad (3.12)$$

where W_i is the necessary energy to produce one electron-ion pair. For LXe has the value is $15.6eV$.

In this case, the equation 3.11 can be written as:

$$W_{ph} = \frac{W_i}{1 + \frac{N_{ex}}{N_i}} \qquad (3.13)$$

Different experimental studies [27, 28] estimate variations of $\frac{N_{ex}}{N_i}$ from 0.06 to 0.2 that lead to $W_{ph,max} = 13.8 \pm 0.9eV$.

So, assuming full recombination and no bi-excitonic quenching [29], for relativistic heavy ions, the maximum *scintillation yield*, L_y, in LXe i.e. the number of photons produced per unit energy or the average energy required to produce a scintillation photon, is estimated to be, as we present above, 13.8eV.

The energy measurements of dark matter particles from LXe detectors are not obtained using directly the scintillation signal because the precise absolute scintillation yield is difficult to be reached. Related to this problem we are introducing a factor of converting the scintillation signals to nuclear recoils, $\mathcal{L}_{eff}$ *(the relative scintillation efficiency of nuclear recoils)* defined as:

$$\mathcal{L}_{eff} = \frac{L_{y,NR}}{L_{y,ER}} \qquad (3.14)$$

where $L_{y,NR}$ is the scintillation yield of nuclear recoils (NR) and $L_{y,ER}$ is the scintillation yield of electronic recoil (ER) using using γ-rays at 122keV energy from a ^{57}Co source and without any electric field.

Figure 3.1 shows the fit along several experiments dedicated to measure $\mathcal{L}_{eff}$.

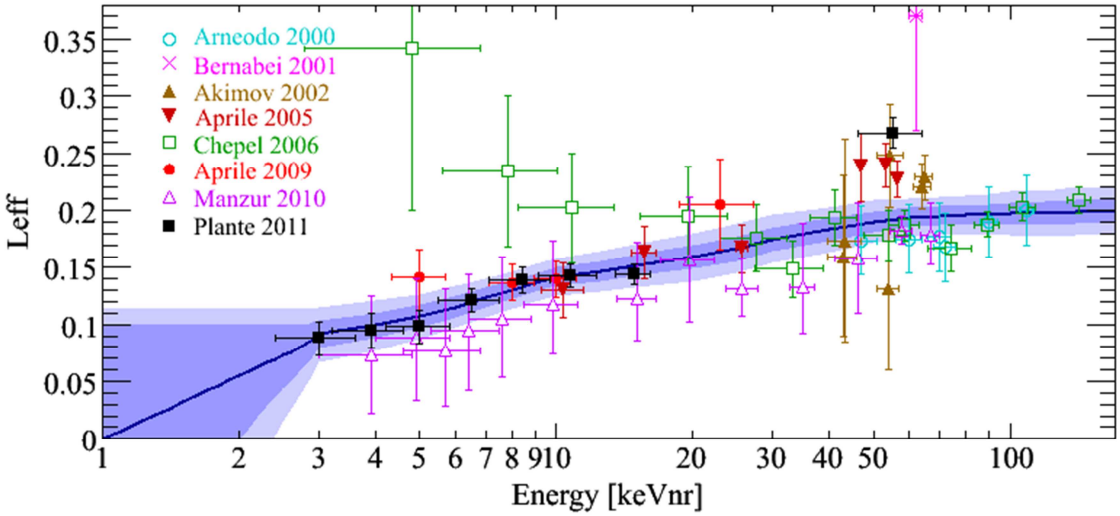

FIG. 3.1 – Global fit with all measured data for $\mathcal{L}_{eff}$ [30]

The scintillation collection efficiency should be increased by constructing the LXe detectors with high VUV reflecting materials as PTFE. Measurements of this material reflectivity in LXe reached a maximum value of 95% [31].

3.2.2.2 The ionization signal

LXe is the detection medium with the largest ionization yield, requiring an average energy of 15.6eV for producing the electron-ion pairs. The electrons produced by ionizing radiation can be drifted for long distances as it happens in XENON100 experiment (~30cm) or in the future XENON1T experiment (~1m). The drift velocity depends on the applied electric filed for low values and it saturate for high values.

To be able to measure this signal, the electron recombination should be stopped by applying the external electric field and electrons drifting through detection medium should not attach to electronegative impurities. Attaching to impurities, the ions formed are drifting much slower, implying the reduction of charge signal. The time spent by an electron before attaching to an electronegative impurity is named *electron lifetime* and depends on impurity concentration. LXe should be continuously purified; the main electronegative impurity responsible for electron attachment is O_2. Other details about target purification, so necessary in this case, are presented in chapter 4 and 5.

In the GXe phase if a strong electric field is applied, drifting electrons can acquire enough energy between collisions with Xe atoms, to exite the atoms and to produce scintillation light. This effect is named *electroluminescence* or *proportional scintillation,* since the light produced is proportional to the number of electrons drifting (see FIG. 3.2).

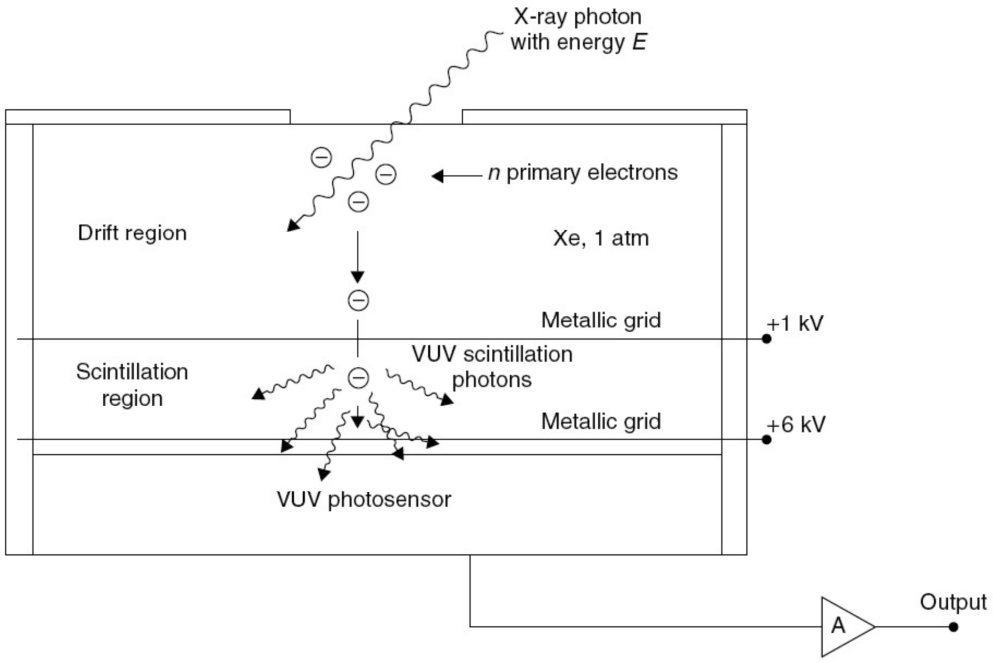

FIG. 3.2 – Example of electroluminescence production principle

For detectors that are using dual phase Xe, liquid and gas, it is possible to ionize in the liquid phase (drift region) and then to drift the electrons into the gas phase (amplification or electroluminescence region). When radiation is absorbed in the drift region (of weak electric field) then the ionization electrons drift into the electroluminescence region (of a moderately high electric field) where each electron is accelerated, exciting but not ionizing the gas atoms or molecules. The excited atoms decay, emitting UV light or *secondary scintillation* with an intensity two or three order of magnitude stronger than the *primary scintillation* (presented in previous section).

In xenon, electroluminescence (EL) occurs for a fairly wide range of E/p where E is the electric field corresponding to the process, and p is the pressure of the gas. For the constant, uniform E/p and total voltage V, the total gain η, for EL, is the number of photons generated per electron:

$$\eta = \frac{V}{V_{ph}} \qquad (3.15)$$

where V_{ph} is the average potential to generate one photon for the given E/p [32]. In the region of intense electric field between the two metallic grids, the electroluminescence signal is expected to spread over about 2μs, given that the drift electron velocity is $2 - 3\ mm/\mu s$ [33].

The electroluminescence light is peaked at 178 nm (it has the same nature of the primary scintillation UV) and is emitted isotropically. Good reflectivity of the detector walls will ensure that approximately a half of photons will reach the readout plane behind the electroluminescence grid, and the other half will reach the opposite readout plane, and the light (on the readout planes) is distributed in the same way.

CHAPTER 4

The XENON100 Experiment

The nature of dark matter and dark energy which account for >96% of the universe density [34, 35], is one of the most fundamental question in physics. As stated before in section 2.2, the leading candidates for dark matter are relic particles from the Big Bang known as WIMPs. Such particles are also predicted by extensions of the standard model of particle physics, such as SUSY [36, 37].

If WIMPs exist, they must constitute the dominant mass in the Milky Way, and, though they only very rarely interact with conventional matter, should nonetheless be detectable by sufficiently sensitive detectors on Earth. To cover this, it will be required an increase in sensitivity from the actual rate limit of ~0.1 evts/kg/day to less than 1 evts/ton/yr, demanding raising detector mass and exposure, coupled to an improved rejection of radioactive and cosmic backgrounds.

Cryogenic noble liquids, such as argon and xenon, offer the best prospects for detectors with large mass and background rejection capabilities. In the XENON Dark Matter experiment, the simultaneous detection of ionization and scintillation in a liquid Xenon (LXe) 3-D position sensitive time projection chamber (TPC) is used to identify nuclear recoils produced by WIMPs and neutrons as well as electron recoils produced by gamma and beta background. The results from the XENON R&D pointed to a rejection efficiency of 99%.

On the other hand, the event localization with millimeter resolution and the self-shielding capability of a large, homogeneous and dense liquid volume, provide additional background discrimination, unique to cryogenic liquid TPCs.

XENON Experiment started with a 10kg order fiducial mass prototype (XENON10) at Gran Sasso underground Laboratory [38], in Italy. Together with results from other smaller detectors, the performance of this first generation of TPCs

demonstrated the capability of the XENON approach for dark matter detection. With a nuclear recoil threshold of 10 keV, lower than originally proposed, XENON10 has reached in 2007 a sensitivity limit of $\sim 2 \times 10^{-44} cm^2$, comparable to the best published limit by CDMS II [39] at that time.

Based on these results and progress, XENON Collaboration proposed to pass to the next phase of the XENON original project, with the realization of a 100kg order fiducial mass detector (XENON100), to probe a spin independent WIMP-nucleon scattering cross section limit of $2 \times 10^{-45} cm^2$ [19] The detector is essentially a scaled up volume version of XENON10, by a factor of ~10.

In this chapter the specific properties and techniques used in the XENON100 detector, to increase the sensitivity and to reduce significantly the background, as well as the description of the experiment design, subsystems and calibration procedures, are presented, as Coimbra group is also part of this effort. The contribution for the data analysis and the dark matter search results obtained are specially outlined in the next chapter.

4.1 Detection principle used in the experiment

The XENON experiment works on the principle that a passing WIMP should very occasionally bump into a xenon atom, a fat target with 54 protons and 54 electrons. Such collision would release energy due to the atom recoil which can be detected by sensitive instruments.

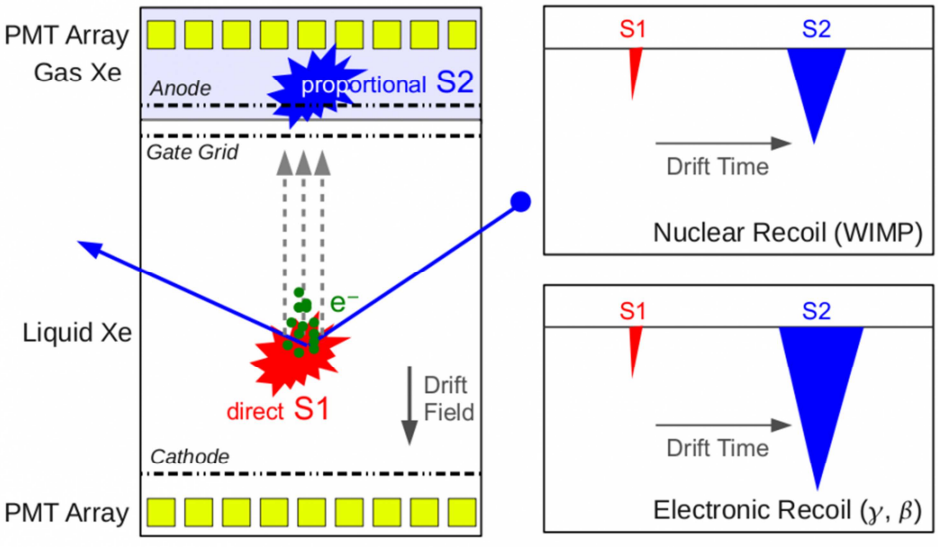

FIG. 4.1 – Detection principle: A prompt scintillation signal (S_1) is produced from a primary interaction in LXe, whereas a delayed, proportional signal (S_2) is produced into the gas phase, after the drift and extraction of electrons, originating from the ionisation of Xe. The S_2/S_1 ratio is used for electron and nuclear recoil discrimination [40]

This experiment uses LXe as target that is a very good scintillator. The interaction processes in Xenon are of the excitation and ionization types. The excitation process consists in one exited atom inducing the creation of an excited excimer Xe_2^*, which decays emitting VUV photons $h\nu$.

$$Xe^* + 2Xe \rightarrow Xe_2^* + Xe \qquad (4.1)$$

$$Xe_2^* \rightarrow 2Xe + h\nu \qquad (4.2)$$

This is the prompt scintillation (S_1) which can be seen by PMTs immersed in the LXe since quartz windows are transparent to the 178nm peaked light. The technique that this experiment involves is the use of a dual phase TPC to collect the small ionization signals that cannot be read directly. A small gas gap (few mm) is present at the top of detector. The electrons from the ionizations are drifted via an electric field ($0.53\ kV/cm$) towards the gas phase where the field is strong enough ($\sim 12\ kV/cm$) to create a secondary scintillation signal (S_2) pulse. The time delay between S_1 and S_2 allows the collection of both signals independently (see FIG. 4.1).

4.2 The XENON100 detector

4.2.1 XENON100 backgrounds

The detector of XENON100 experiment is located in the underground Gran Sasso Laboratory at an approximate 1400m depth bellow the Abruzzo mountains. Walking through cavernous halls midway on a 10 km long road tunnel (see fig. 4.2 below) one can see the XENON100 detector tucked away at the end of a small side tunnel. It is the current detector with 162kg total Xe mass that followed the XENON10 phase of the XENON collaboration. XENON10 used a total of 15kg of liquid xenon as detection medium, obtaining competitive results with liquid xenon target.

XENON100 detector is installed at LNGS (*Laboratori Nazionali del Gran Sasso)* in Italy, since the spring of 2008.

In common with other experiments that aim to directly detect dark matter, XENON experiment is housed underground for the rocks above it to shield from particles and radiation such as cosmic rays from outer space that might otherwise confuse the data. The challenge of XENON collaboration is to block as much as possible this “background” and see what’s left.

XENON100 was designed to achieve an ultimate WIMP nucleon cross section of $\sim 2 \times 10^{-45} cm^2$ corresponding to an event rate of $0.05\ mdru$ in the nuclear recoil (NR) energy region $10 - 40\ keVr$ ($1 mdru = 1 \times 10^{-3}\ events/kg/day/keV$). To achieve this goal, we rely on material selection, effective electron recoil rejection and volume fiducialization.

FIG. 4.2 – LNGS underground laboratory structure and XENON100 location

For neutron induced backgrounds, we assume the muon flux at the Gran Sasso Laboratory. XENON100 is installed in the passive shield and complemented by an active LXe muon veto. The design of the detector is such that the contribution from external (α, n) neutrons and gammas, as well as from neutrons and gammas emitted from the shield itself, are subdominant (see tables below). We divide the background sources in external and internal ones. External backgrounds originate from the radioactivity of the underground cavern and from cosmic ray (muon) interactions. Internal background originates from the detector and shield construction materials, as well as from impurities (^{85}Kr), double beta decays (^{136}Xe) and cosmic activation of the LXe itself.

Table 4.1 summaries the neutron background in XENON100: the total is well below the expected WIMP rate of 0.05 $mdru$ at 10 $keVr$ energy threshold and a cross section of $\sim 2 \times 10^{-45} cm^2$. The neutron background is dominated by the muon induced neutrons in the Pb shield. We have to specify that this result is not taking into account the 99% muon veto power.

On the other side, the electron recoil background in XENON100 is dominated by the PMTs radioactivity. Table 4.2 shows the values of the gamma background sources in the detector. After applying the 99% electron recoil discrimination, we achieved a

conservative rate of $0.018\,mdru$, which is a factor of ~3 below the expected WIMP rate.

TABLE 4.1 – Count rates for neutron backgrounds in the energy region 10-50keVr without 99% muon veto power

Neutron background source	*Count rate [mdru]*
Neutrons from PMTs by (α,n)	0.003
Neutrons from other detector components	0.001
External neutrons (rocks/concrete)	0.002
μ induced neutrons in the shield	0.008
HE μ induced neutrons in the rock	<0.003

TABLE 4.2 – Count rates for gamma backgrounds in the energy region 10-50keVr without 99% electron recoil discrimination

Background source	*Count rate [mdru]*
γ's from PMTs	1.0
γ's from other detector components	0.4
External γ's and γ's from shield	0.2
β's from ^{85}Kr decays	0.2
Cosmic and β's from 2νββ decays	<0.05

4.2.2 The XENON100 detector TPC

In the figure below one can see the detector image: a typical position – sensitive Xe TPC composed of an almost-cylindrical reflective Teflon (PTFE) surface with 30cm height and 15cm radius and two PMTs arrays for the scintillation light detection. 98 PMTs are arranged in concentric circles at the TPC top for good position reconstruction and 80 PMTs at the TPC bottom arranged as close as possible for optimal collection efficiency.

For this detector PMTs (Hamamatsu R8520-06-Al, 1´´x1´´) with high quantum efficiency ($\sim 24\%\ to\ \sim 35\%\ for\ 178nm$) and low radioactivity have been selected.

Surrounding the main target, 63kg of LXe with another 64 PMTs act like an active veto. One of the main advantages of the active veto is the reduction of background rate in the entire target volume by 50%. The PTFE [43] cylinder reflects scintillation light with high efficiency and optically separates the LXe target from the veto. The Teflon is used also as electrical insulator.

FIG. 4.3 – Teflon cylindrical structure of the detector [41, 42]

The Teflon cylinder carries the resistive network and the high voltage (HV) racetrack of 40 shaping rings, regularly spaced along the TPC wall ensuring the homogeneity of the electric field in the liquid. The anode that is placed 5mm above the gate provides the strong electric field, E_g needed for the electron extraction (see figure 4.5).

The gas gap, d_g is the distance between the anode and the liquid surface, where the secondary scintillation photons are emitted. The wire meshes and top PMT array are mounted in a cylinder closed on top but open at the bottom, which works like a "diving bell'' keeping the liquid level at a precise height, d_l (see figure 4.5 below). A positive

pressure in the bell is provided by the gas returning from the continuous recirculation system, to prevent level rising.

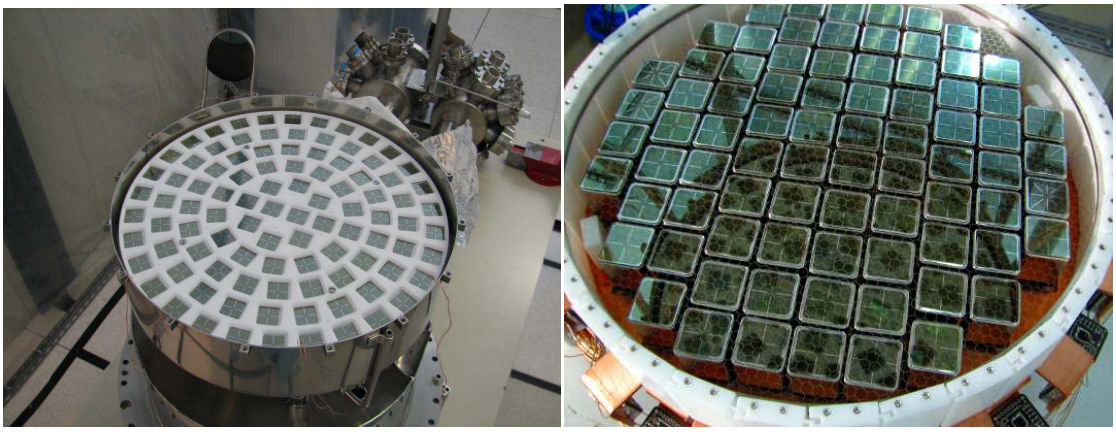

FIG. 4.4 – Left: Top PMTs array; right: Bottom PMTs array [41, 42]

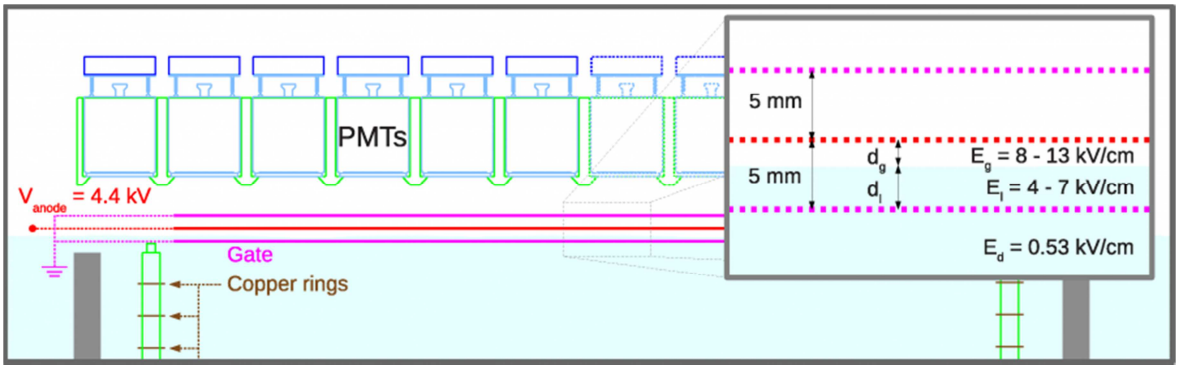

Fig. 4.5 – The scheme of the top part of the TPC; green areas indicates the PTFE used as insulator and reflector of VUV scintillation light [42]

The $E_d = 0.53\ kV/cm$ field for drifting the ionization electrons across the 30 cm drift gap, that is produced between the cathode at negative potential and the grounded gate grid, and the HV applied to anode for optimized electron extraction and gas amplification fields are provided by a custom-designed feed-through which emulates a Teflon HV coaxial cable. Commercial ceramic HV feed-through are highly radioactive and their design is not appropriate for our detector.

The "diving bell" and the vessel enclosing the TPC structure with PMTs, are made of ultra pure, oxygen free copper (OFHC). The detector is placed into a double walled cryostat made of stainless steel (SS 316Ti), selected for its low activity especially in ^{60}Co (see FIG. 4.6).

To reduce the amount of radioactivity significantly, the instrumentation, in particular all electrical feed-through and the cry-o-cooler, have been moved away from the detector vessels and mounted outside the passive shield (FIG. 4.7). All feed-through

for HV, signals, control lines, as well as gas and vacuum lines are mounted above the top flange, via long extension tubes. The shield is composed by 5 cm of ultra-pure OFHC copper, then 20 cm of polyethylene, 5 cm of low radioactivity lead and another 15 cm of standard lead and finally ~20 cm of water are shielding against neutrons on four sides.

FIG. 4.6 – Photo of Xe100 cryostat [41, 42]

FIG. 4.7 – Image of water/ lead/ polyethylene/ copper shield [41, 42]

A Pulse Tube Refrigerator (PTR) is used to cool the detector, liquefying the gas and keeping the liquid at the desired temperature.

4.2.3 Recirculation and purification system

The XENON100 detector requires a total of 162 kg of Xe, to fill the target and the active veto. The gas can be stored in 4 aluminum cylinders, each bottle containing 8000 standard liters of GXe (~43kg) at 50atm pressure, interconnected by high pressure valves (140atm). The bottles can be cooled with liquid nitrogen (LN_2) during the recuperation from the detector (see FIG. 4.8). The recirculation system was built in collaboration between Coimbra and Columbia Universities (see FIG. 4.8).

Xenon is readily purified for most electronegative and radioactive impurities. To do this, the liquid xenon from the bottom of the detector is evaporated in the gas line and goes to the buffer volume of the recirculation system. The KNF diaphragm pump circulates then the gas through the SAES heated getter purifier to reduce the concentrations of H_2O, O_2, CO, CO_2, N_2, H_2 and CH_4 below 1 ppb. The recirculation

flow is kept stable to ~5slpm (standard liter per minute) with a Teledyne flow controller.

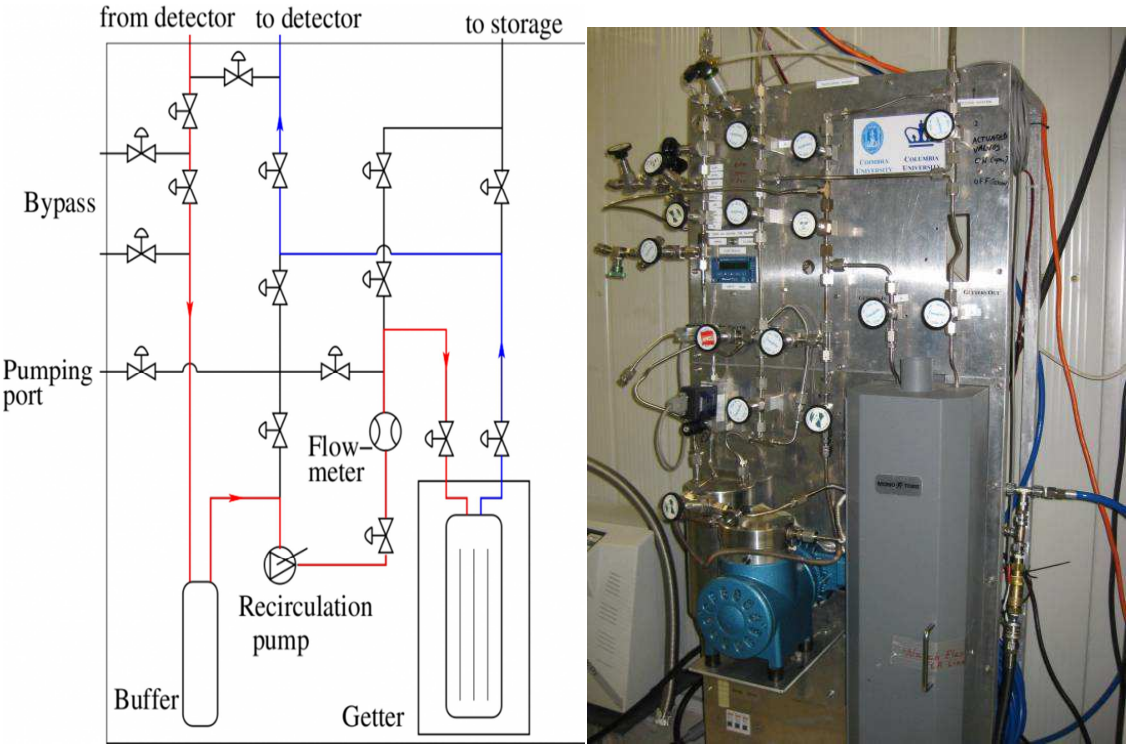

FIG. 4.8 – Xe recirculation system [42]

FIG. 4.9 – Kr purification system [41, 42]

FIG. 4.10 – Xe recuperation system [41, 42]

The notable exception from the usual purification is the ^{85}Kr radioactive isotope, present in commercial Xe gas at ppm level. A serious background for dark matter search is the beta decay of this isotope. In order to reduce the Kr to acceptable levels (ppt) a small- scale cryogenic distillation column made by Taiyo-Nippon Sanso has been used to purify the gas (see FIG. 4.9). It is 3 m tall and the purification speed is 0.6 $kg/hour$. This kind of purification is done every beginning of data taking scientific run, when all the xenon from the detector is recuperated in the 4 bottles and distillated through the column. The recuperation system built in Coimbra can be seen in FIG.4.10.

4.2.4 Safety systems

The XENON100 experiment is running continuously, day and night, 7 days per week, so it needs special attention. A set of activities should be done every day both in the underground laboratory where the detector is located and also above ground. A set of duties are assigned to the person taking care of the XENON100 detector for a determined period of time.

Thanks to the Slow Control System, XENON00 detector can be kept under remote observation 24h/day and running continuously in normal and safe conditions. For emergency procedures associated with handling a large volume of cryogenic liquid underground, an independent liquid nitrogen cooling system, controlled by the chamber pressure is automatically activated (powered by a dedicated UPS) in case of emergency. This emergency cooling keeps the detector in a safe state also in the extreme case of total power failure and no access to the underground laboratory for ~24h. We note that the large mass and thermal capacity of the detector stabilizes the temperature and the pressure in the system against abrupt changes. We have verified that even in the case of catastrophic cooling failure the thermal inertia will provide sufficient time to take the needed safety actions in a controlled and safe fashion.

4.2.4.1 The Slow Control System

A Slow Control System (SCS) [44] is responsible for real-time monitoring and controlling of different parameters. This system was built and continuously improved by the Coimbra group.

Once xenon is present inside the chamber in liquid and gas phase, constantly re-circulating through the purification system lines, the pressure inside detector is the most important parameter to be monitored since the variations over the set limits of this pressure will find out easily if the instability is created by one of the instruments in charge of this operation. The pressure is monitored by a GT1600 sensor.

There are six important temperatures to be monitored: Pulse Tube Refrigerator temperature and heat-link temperature (cold-finger) controlling xenon cooling and

liquefying and 4 temperatures monitored inside the detector in different heights of the TPC: top, bottom, below bell and inside bell. All the temperatures are read by a controller (Lakeshore 340) which communicates with the SC server via an RS232 interface.

The cathode HV is controlled by a Heinzinger PNC 100000-3neg power supply. This model can apply up to -100kV and 3 Amperes, and is applying on our detector -16kV.

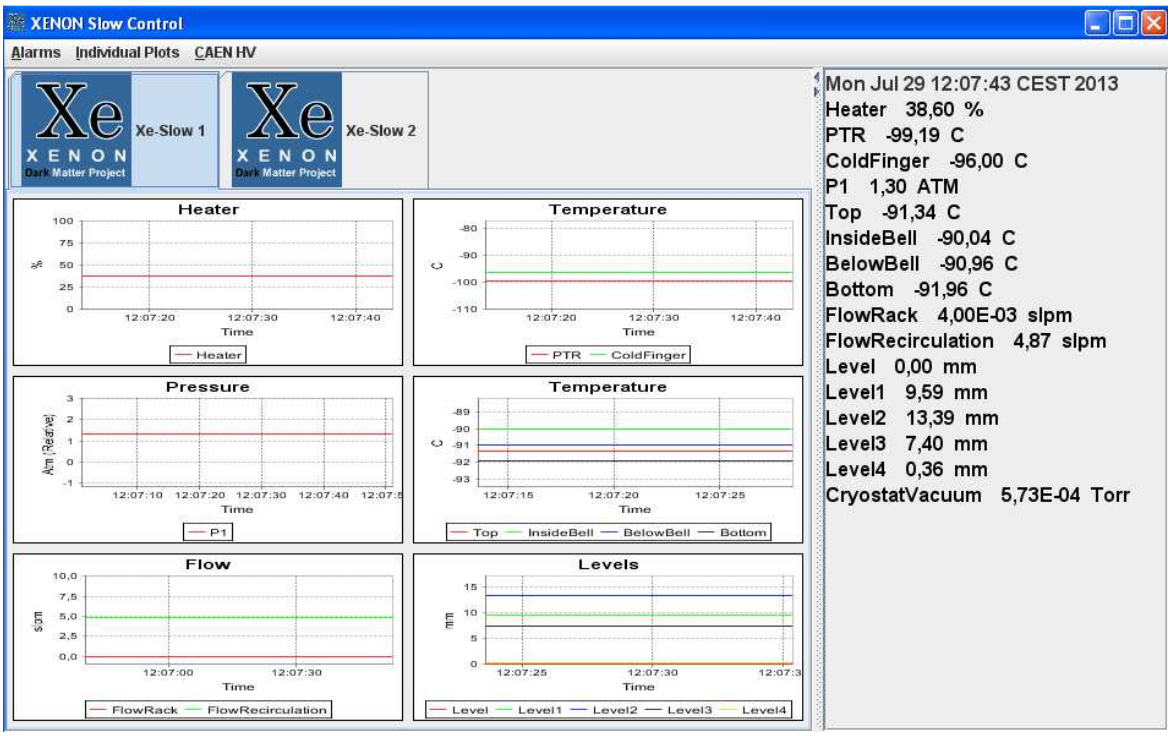

FIG. 4.11 – The main window of the SC Client program

The SC system is capable of handling a large number of instruments for reading and controlling. The whole structure of the slow control system is composed by both hardware and software designed in the Object Oriented paradigm, coded on Java language. The SC system consists of 3 main software components:

- *SC Server*, is an application that runs in a computer underground (SC machine) and locally records the physical parameters making them available to the remote clients.
- *SC Client*, is a graphical application that can run on any machine connected to the internet. It is used for real time visualization, local recording and customized local sound alarms. Figure 4.10 shows the main window of SC Client.

- *SC Alarms*, is an application that continuously monitors the physical parameters available on the SC Server, within a given range, issues periodic status reports, as well as e-mail and SMS alarms. An external application monitors the connection of both Alarms machines to the internet. It periodically pings the Alarms machines and sends an e-mail notification if the machine cannot be reached. In this way it is guaranteed the continuously monitoring of all different layers of the structure.

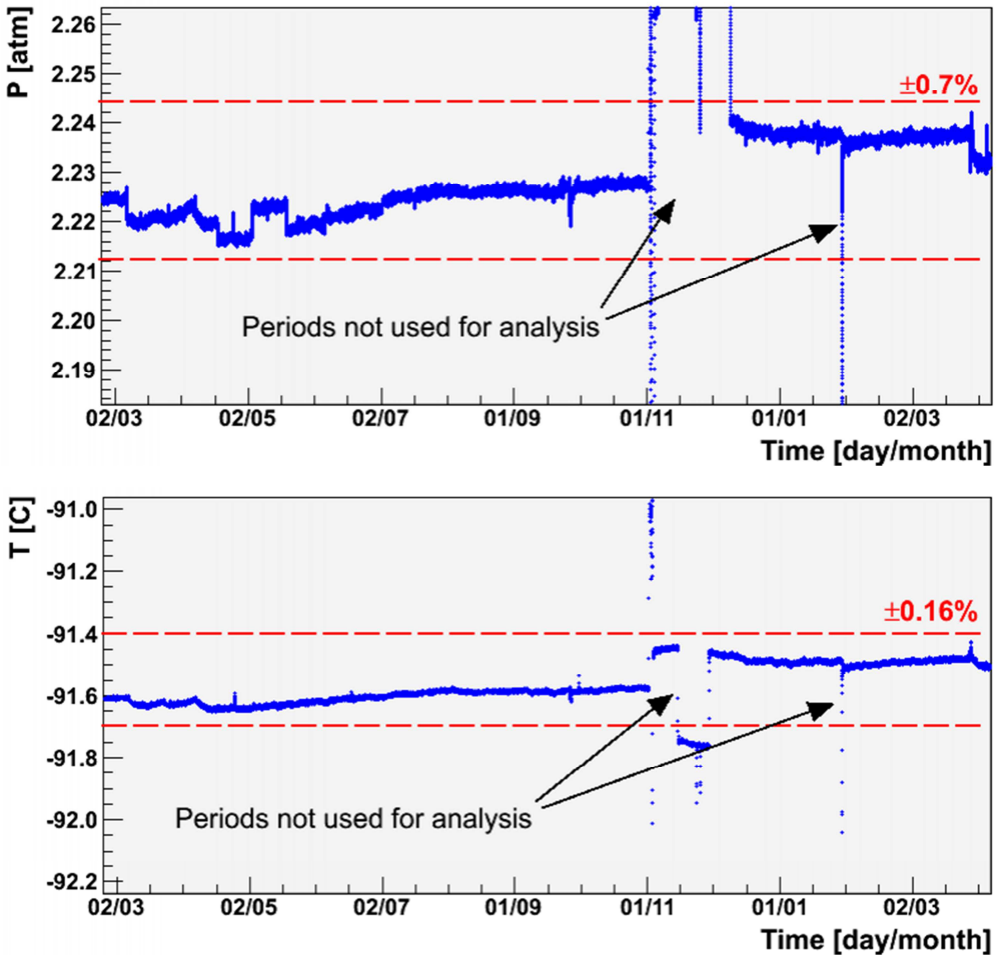

FIG. 4.12 – Example: Absolute pressure (up) and heat-link temperature (down) registered by the SC system in one of the last XENON100 runs [42]

The efficiency of the SC system is clearly visible in the XENON results. For the Run10, of 225 live days of data, the detector has been in continuous operation for a total of ~20 months and this is the first LXe detector in history to operate continuously for such a long period of time. In the figure behind (FIG. 4.12) you can see the stability plots of the absolute pressure and heat-link temperature in the period of the last run.

4.2.5 Readout electronics and Data Acquisition (DAQ) system

The XENON100 TPC events feature a fast (few ns) pulse from direct scintillation in the liquid (S_1) and a slower (~μs) pulse from proportional light in the gas (S_2). The two pulses occur within the maximum drift time of 200 μs ($2mm/\mu s$ electron drift velocity in LXe). The DAQ system acquires full waveforms from the top and bottom PMT arrays (see FIG. 4.13 below). The minimum sampling rate is given by the fast S_1 signal. For optimal signal/noise ratio, a digitization rate of 100MHz is adequate. The time scale for the event acceptance window is determined by twice the maximum electron drift time, i.e. 400 μs in total.

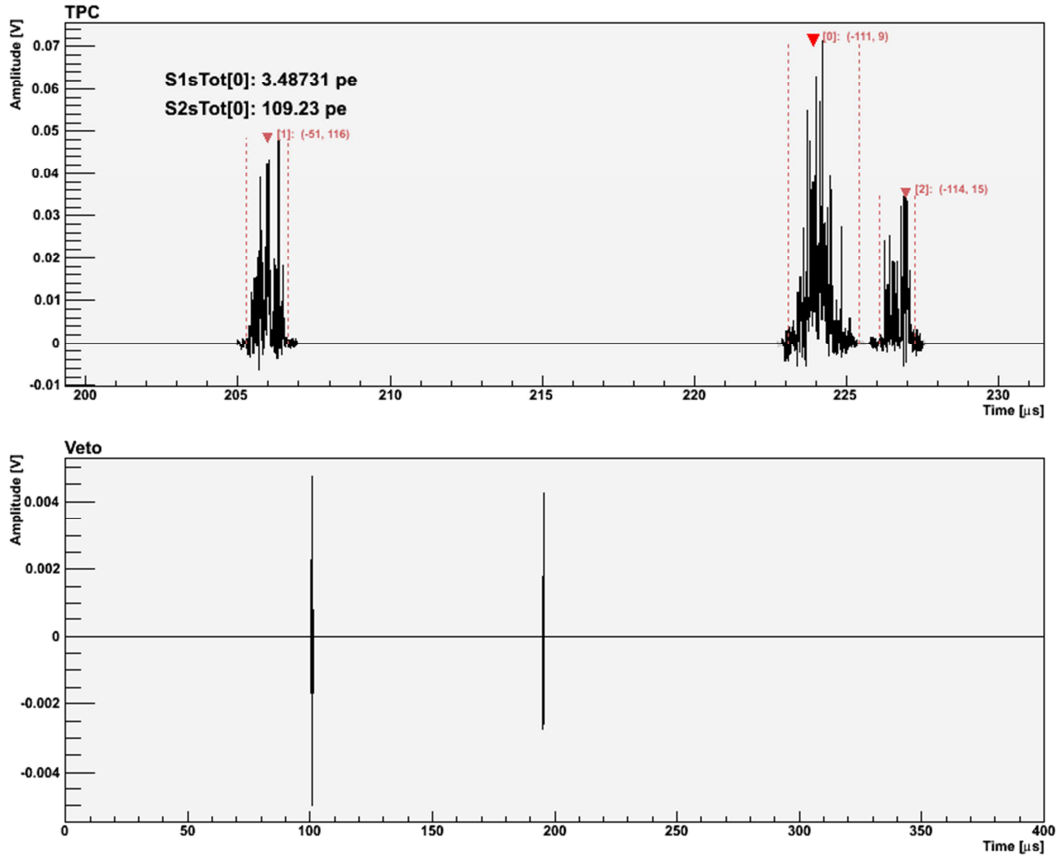

FIG. 4.13 – Example of waveform acquired by DAQ system, inside TPC (up) and veto region (down) [42]

For the dual phase operation of the TPC, we need a large dynamic range, since the system must be able to handle single photoelectrons signals from direct scintillation of a few keV gamma-rays, up to several thousand of photoelectrons for the amplified charge in gas. The PMT signals are passed through variable-gain, low-noise amplifiers. The signals are then digitized with 100MHz 14 bit resolution (CAEN V1724A). The digitizer has dual-port buffer memories for dead time free operation and one Field Programmable Gate Array (FPGA) per channel for online data processing.

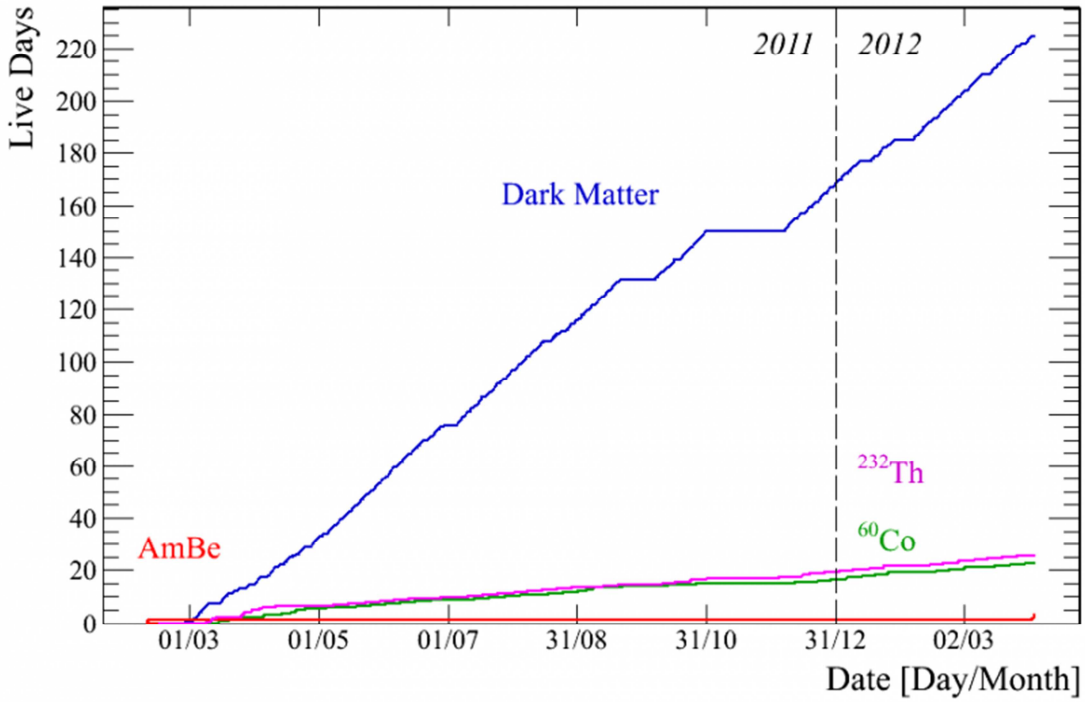

FIG. 4.14 – Example of plot describing data acquisition during one of the scientific runs (Run10) [42]

The FPGA scans the data while they are stored into the buffer memory. When a programmable threshold is crossed, a pointer to the memory location is stored. During acquisition only the channels with detected signal are read, and for them only short time windows (few μs) around the detected hits are transferred. With this scheme a factor 50 in data reduction is easily attained with no loss in original data: also multiple events are fully saved for later classification as background. A similar readout scheme was successfully designed also for the LXeGRIT balloon-borne experiment [45]. We implement a basic "majority" trigger, firing when a given number of channels go above a predefined threshold: this allows trigger on either S_1 or S_2. This configuration has been successfully tested. The generated trigger is then used to control the data readout.

In FIG. 4.14 can be seen the comparison between the amount of blinded dark matter data and calibration data acquired in one of the scientific runs.

4.2.6 Calibration of XENON100 detector

A series of detailed calibrations are designed to provide the position reconstruction, and the energy and recoil type of a given interaction. These calibrations are described in this section.

4.2.6.1 Position reconstruction

The reconstruction of the X-Y-Z position of an event is important for the purposes of position dependent corrections. The position reconstruction is determined in two steps.

The first one that implies the time difference between S_1 and S_2 is used for the determination of the Z coordinate, calculated then, from the drift velocity of electrons ($\sim 1.8\, mm/\mu s$) and the drift time. There is a diffusive process affiliated with the drift, but this should only modify the width of the S_2, as the electron cloud centroid moves at the drift velocity. The contribution from diffusion is therefore minimized by the drift time as the time between the peaks of the S_1 and S_2 signals, which correspond to the drift time of the electron cloud centroid. The resolution of the Z position determined by the S_2 width is estimated to be $< 2mm$.

The second step is for the reconstruction of X-Y coordinates. This is more complicated as it is based on the hit pattern of S_2 on the top PMTs array. Three different algorithms, one of them based on a neural network, other in a vector regression and a third on chi-squared minimization are developed and a resolution of $< 3mm$ is achieved. In FIG. 4.15 below you can see the XY position from both top and bottom PMTs arrays information.

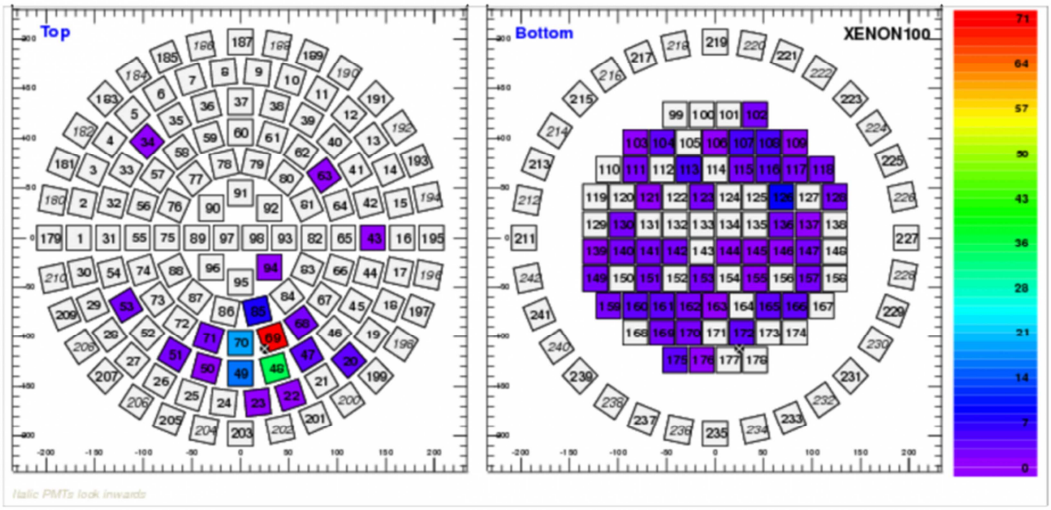

FIG. 4.15 – The XY amplitude of the signals from the both PMTs arrays [42]

4.2.6.2 LED calibration

All 242 PMTs in XENON100 detector are monitored. LED calibrations are performed every week, using a pulsed LED, to ensure its performance and the gain (ratio of charge output to charge input in the multiplication chain) is measured to

convert all PMTs signals to photoelectrons (pe). The LED is situated outside of the detector and the light is brought inside through optical fibers.

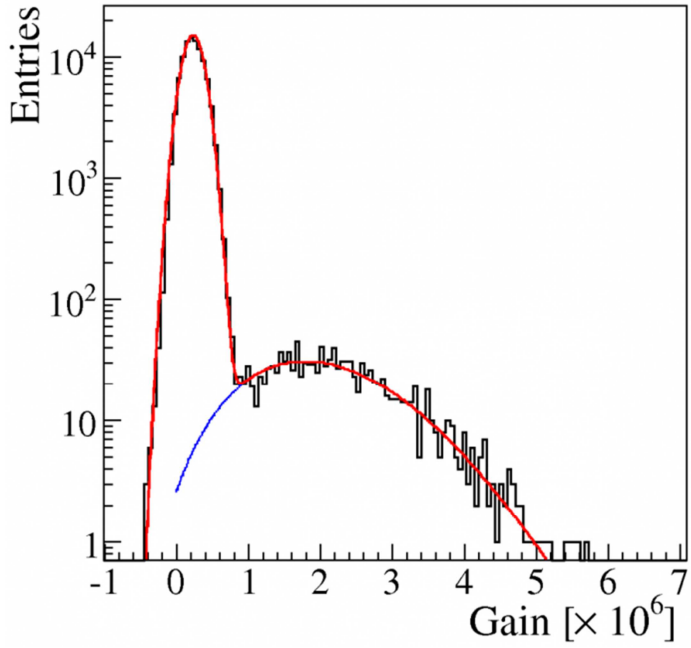

FIG. 4.16 – Typical PMT calibration spectrum; the left peak is the pedestral further right the PMT response to the LED light is observed [42]

A typical LED spectrum can be seen in FIG. 4.16. The mean value of the gain is $2 \times 10^6\ pe/e$. More information can be found in [46].

4.2.6.3 Electron lifetime determination

The electron recoil energy scale, or electron equivalent energy, is measured in units of keV_{ee}. To perform this calibration, a ^{137}Cs source which emits $662keV$ gammas was used. The single gamma line allows for an absolute calibration of the energy scale by fitting the full absorption peak of the spectrum to obtain the number of photoelectrons per keV_{ee}. The high energy gammas penetrate the entire TPC performing the position dependence correction.

As explained in the previous chapter, the electron lifetime depends on the impurities. A distribution of S_2 as a function of drift time can represent this absorption. In FIG. 4.17 an example of electron lifetime calculation is presented for a ^{137}Cs data set.

Weekly calibrations are performed to monitor the xenon purity. The electron lifetime is increasing due to the continuous purification through the Xe recirculation/purification system. In FIG. 4.18 a plot of the electron lifetime values registered in one of the scientific runs (Run10) can be seen. The substantially lower regions are due to maintenance operations. The decrease on electron lifetime is sudden

while the improvement has an exponential trend depending on the total Xe mass and the recirculation speed.

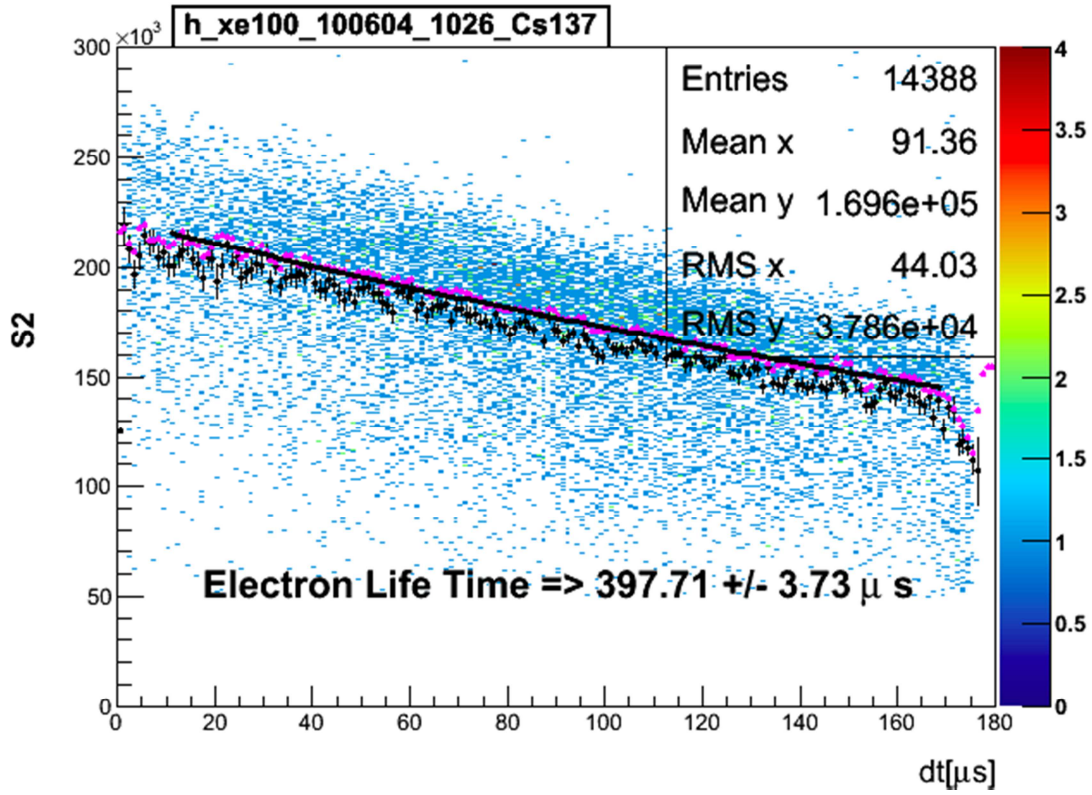

FIG. 4.17 – Distribution of single scatter events as a function of drift time; the attenuation of the signal represents the electron attachments to impurities [42]

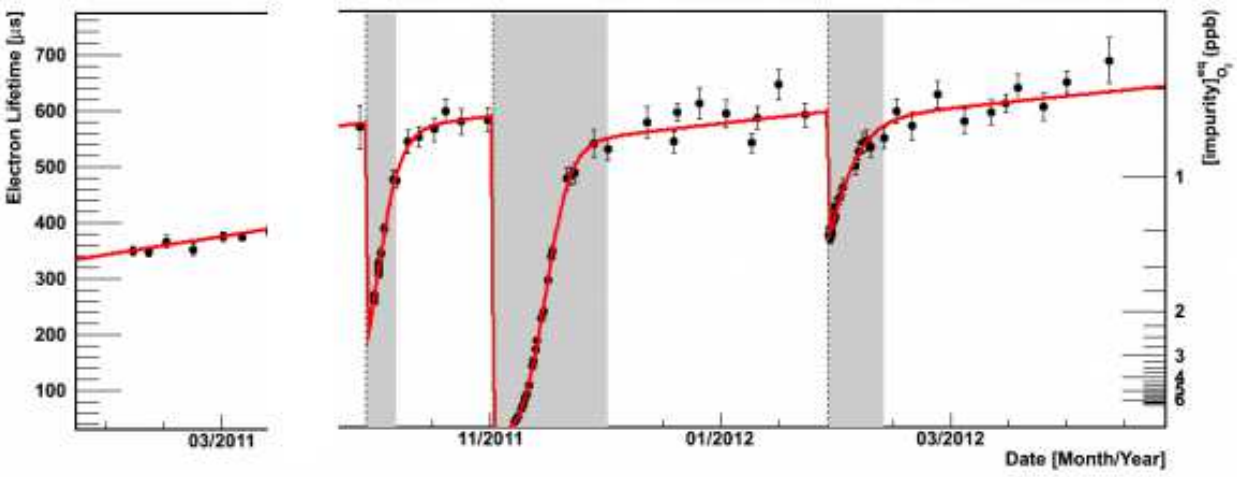

FIG. 4.18 – Exemple of the electron lifetime evolution during one of the scientific runs (Run10) [42]

4.2.6.4 Electronic and nuclear recoil calibration

The detector responds differently to electron recoils and nuclear recoils, so a different energy scale is needed for these two types of events. Dark matter interactions occur as nuclear recoils, so these events are important for our research.

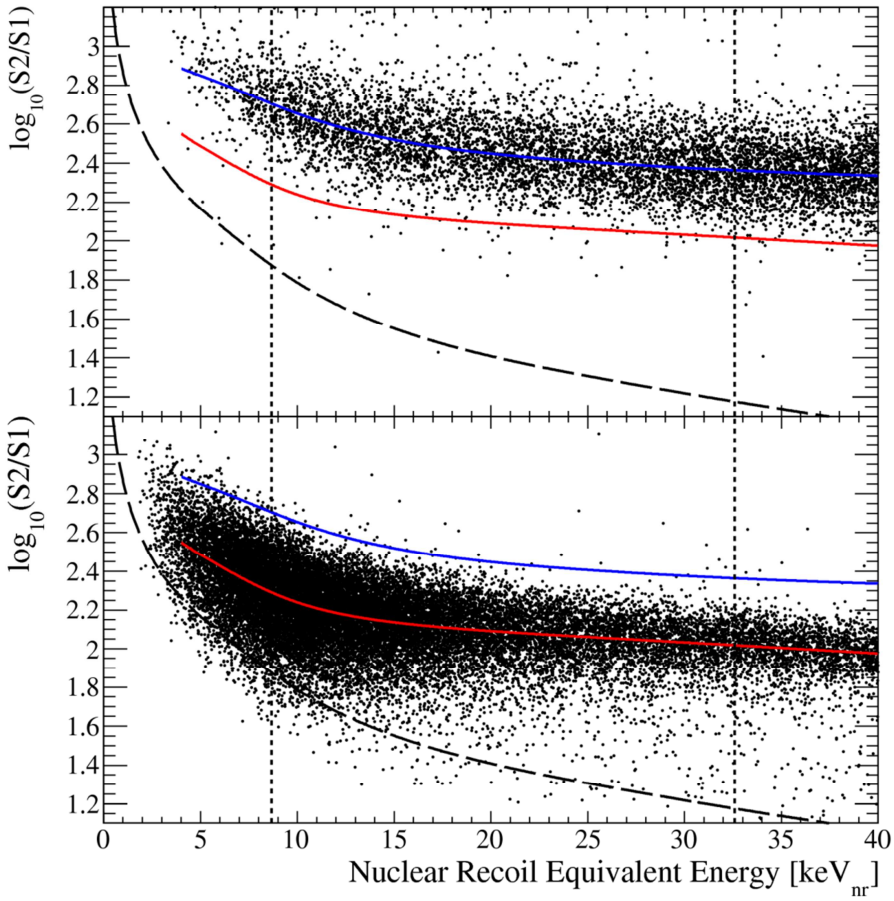

FIG. 4.19 – Detector response to electron recoils (average: blue line, top) and nuclear recoil (average: red line, bottom) [49]

The nuclear recoil energy is related to the S1 signal [47, 48]:

$$E_{nr} = \frac{S_1}{L_y}\frac{1}{\mathcal{L}_{eff}}\frac{S_{ee}}{S_{nr}} \qquad (4.3)$$

where

- L_y is the S_1 light yield;
- S_{ee} and S_{nr} are the field quenching factors measured to be 0.58 respectively 0.95 for the operational voltage;
- $\mathcal{L}_{\text{eff}}$ is the relative nuclear recoil efficiency;

Using dedicated calibration runs, the electron recoil band is measured using gammas from ^{60}Co source while the nuclear recoil band is measured using neutrons from ^{241}AmBe source (see FIG. 4.19).

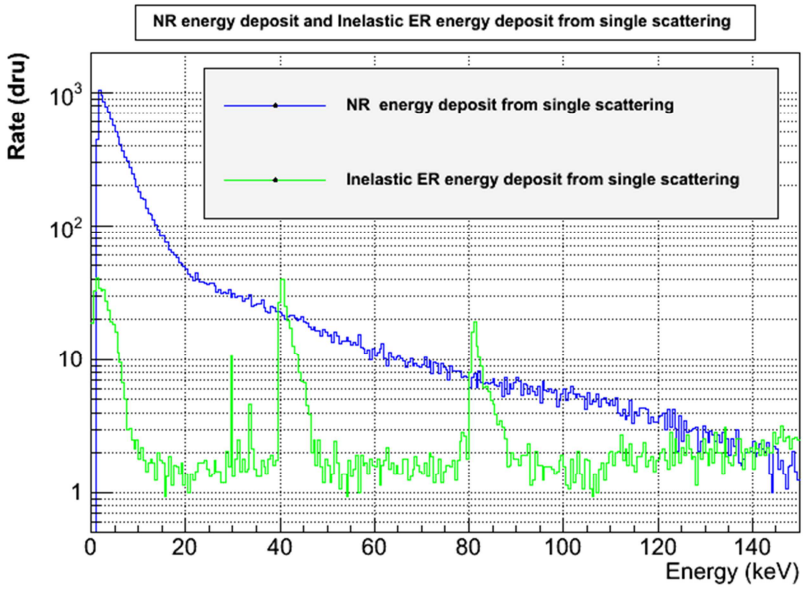

FIG. 4.20 – NR energy deposit and inelastic ER energy deposit from single scattering [50]

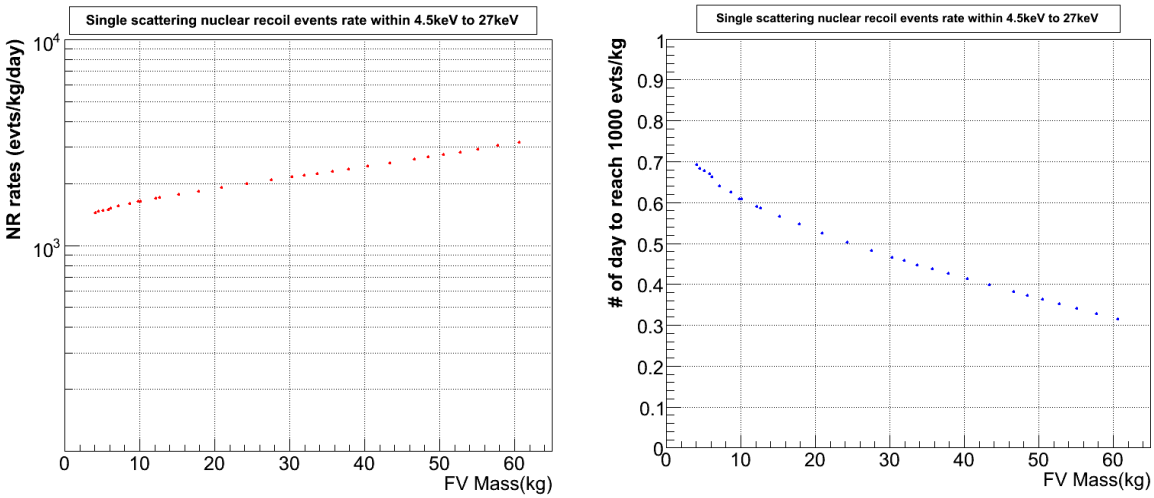

FIG. 4.21 – Left: single scattering NR rates vs. of fiducial volume; right: number of days needed to reach 1000ev/kg vs. fiducial volume [50]

Since we know the AmBe source activity, ~220neutrons/sec for 3.7MBq source [50], we can easily obtain the time needed to have a number of interactions in the sensitive volume of the TPC, data taking time, within certain energy range. By simply

dividing the number of entries by data taking time and categorizing by each event type (NR, ER, elastic and inelastic), it is possible to estimate the rate of each category.

The histogram presented in FIG. 4.20 shows the NR events and inelastic ER events in the energy range from 0 to 150keV for the maximum fiducial volume, 60.6484kg. The blue line represents the nuclear recoil events rate which includes both elastic and inelastic scattering within 4.5keV and 27keV. The green line shows the inelastic ER events and we can see clearly the 40keV and 80keV gamma lines from ^{129}Xe and ^{131}Xe respectively.

The two plots presented in FIG. 4.21 have basically the same information. The first plot shows the single scattering NR rate (evts/keV/kg) within 4.5keV and 27keV as a function of fiducial volume (FV). In the second plot, the Y axis is the number of days needed to reach ~1000 events/kg within fiducial volume. According to this plot we need about 0.4day of AmBe exposure to have 1000 events/kg in 48kg fiducial volume defined by the dedicated volume cut.

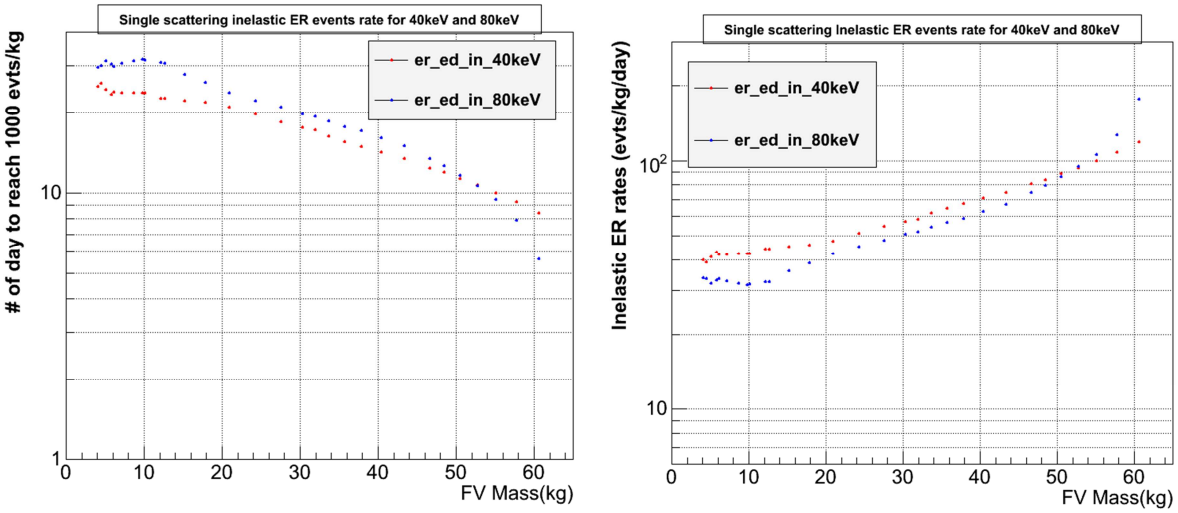

FIG. 4.22 – Left: number of days needed to reach 1000ev/kg vs. fiducial volume; right: inelastic ER rates vs. of fiducial volume [50]

It is also possible to use the AmBe neutron source as 40keV and 80keV gamma ray source. The neutrons from AmBe cause elastic recoil, but in the case of inelastic scattering, Xe nucleus is excited and when it de-excites the 40keV and 80keV gamma ray are emitted from ^{129}Xe and ^{131}Xe respectively. It is expected to need ~15days of exposure to have 1000evts/kg rate in 48kg fiducial volume for both 40keV and 80keV lines (see FIG. 4.22).

In figure 4.23 the AmBe neutron calibration of one of the most recent science runs can be seen. Besides the elastic nuclear recoil band that is the WIMP signal region,

the activated xenon lines at 40keV, 80keV, 164keV, 263keV can be used to characterize light and charge signals as function of energy as well as to perform spatial and uniformity corrections to the data. The activated ^{19}F lines at 110keV and 197keV start becoming also dominant since the gamma-rays are released from the Teflon (PTFE) wall of the TPC.

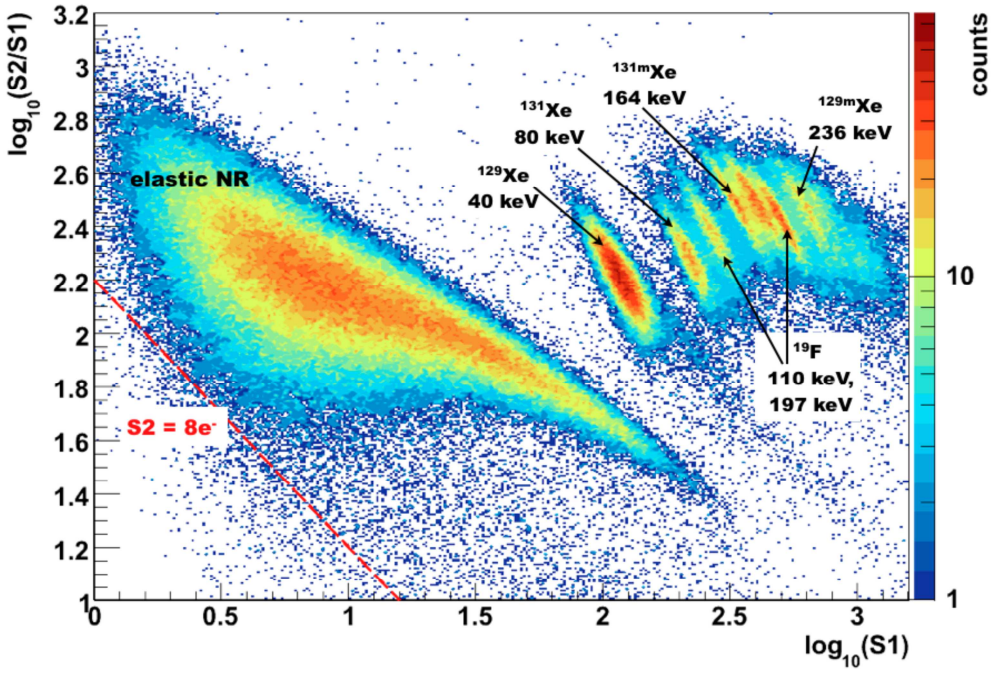

FIG. 4.23 – Ratio between charge and light as a function of energy for AmBe calibration [42]

CHAPTER 5

Data analysis and results of XENON100 experiment

The analysis of XENON100 dark matter experiment is presented in some details in this chapter. While the data analysis is a collaborative work, the huge analysis effort is divided in several fields as: position reconstruction and correction, NR energy scale, selection of dark matter datasets based on several quality parameters, cuts to select proper event signatures from interactions that might be WIMP candidates and cut efficiencies, background expectation and profile likelihood. Each of these fields implies different analysis tasks required for the dark matter search and for every scientific run. Therefore, the first part of this chapter (section 5.1) is focusing on the analysis of the data. Section 5.1.1 is presenting a general description of the most important cuts defined and the sections 5.1.2, 5.1.3 and 5.1.4 describe in details the tasks accomplished and used also to generate the general results and conclusions of the XENON100 experiment that are presented in the second part of the chapter (section 5.2).

5.1 Analysis of data performed

The analysis is based on data acquired since 2010. Usually, a blinded analysis is performed, in which the analysis is based on a limited sample of data and the experiment is run without looking at the data for the WIMP search. The analysis is finished before the data are un-blinded, then the results are presented based on the pre-defined analysis.

During the first 11.17 days of exposure (named Run07), the analysis was non-blind since these data were acquired during the commissioning phase of the detector. Another three dedicated blinded runs, named Run08, Run10 and Run12, have subsequently been performed. Calibration data of these runs have been used also in the

analysis presented below and the competitive scientific results from the un-blinding processes are presented in paragraph 5.2.

5.1.1 Data quality cuts

Parameters which are calculated based on the summed waveform (area [pe], height [mV], width [ADC bins], PMT coincidence level, delay time between S_1 and S_2, etc.) have been used to define data quality cuts in terms of removing spurious events, without changing the nuclear recoil band thus, increasing the signal to noise ratio without reducing the efficiency (probability of an event to pass the cut) for nuclear recoils. Our naming convention for the ROOT Trees programming is that the cut begin with an X and end with the version number i.e., it can be improved during the analysis period. Some of the most important cuts defined are presented below.

5.1.1.1 Basic quality cuts

Some basic cuts were defined to ensure that events satisfy certain quality criteria. Waveforms from muon interactions or micro-discharges are rejected. The *Xsignalnoise* cut is defined on the signal to noise ratio for a waveform. Events with signal to noise ratio less than 1 are discarded. In some situations different PMTs can register increased noise level or very large S_2-like pulses only in one PMT, which are clearly uncorrelated to interactions in the target volume, so special cuts are defined to exclude these PMTs from the waveforms.

5.1.1.2 Energy cuts

These cuts are used to select events in the low energy region, where a WIMP signal is expected, and to ensure that they are not caused by PMT dark current and noise.

To select the required events, a software threshold is implemented at 150pe for S_2. This cut named *XS2peak* has 100% efficiency. Therefore, all S_2 signals smaller than 150pe are discarded.

The *XS1coin*cidence cut is used to remove events for which the S_1 peak really comes from a PMT dark count or other sources which are not expected to produce scintillation photons in coincidence (S_1 in the veto region in coincidence with an S_1 inside the TPC).

5.1.1.3 Consistency cuts

These cuts are defined to remove those events that pass the waveform analysis. In this situation the consistency of the expected single scatter interaction in the target volume is checked based on the S_2 width and S_1 and S_2 light patterns.

The width of S_2 signal is energy dependent and increases with the depth of the interaction in the target volume, due to dispersion of the electron cloud during the drift towards the gas phase. A cut named *XS_2width* has been defined to check if the Z coordinate inferred from the time delay between the S_1 and S_2 peaks is consistent with the width of the S_2 peak.

Another two cuts have been developed to ensure the quality of the position reconstruction and multiple scatter identification.

A fiducial volume cut, for example *X48kg*, is defined to keep only the events within a super-ellipsoid with a reduced radius, defining a mass fiducial target. The fiducial volume cut simply reduces the target mass.

5.1.1.4 Single scatter cuts

The cross-section of WIMP-nucleon scattering is very low, so the probability of a double scatter in the detector is essentially zero. Thus, any double scatter must be due to background. Double scatters occur on a shorter time scale than the scintillation process, so the S_1 singles from the distinct scatters are combined into one larger S_1.

S_2 singles will be collected separately as long as the vertical distance between the scatters is large enough that the S_2 singles do not overlap. The typical width of an S_2 in the energy range of interest is 0.5µs, so the multiple S_2 singles can be distinguished when separated by more than $1\mu s = 1{,}7mm$.

The cuts are defined to select proper events signatures from interactions that might be WIMP candidates, together with their cut efficiencies. All the cuts are developed with respect to the WIMP expectation, i.e. they are optimized for single scatter nuclear recoil at low energies: *XS_2single* (defined on page 59) is the responsible cut for this selection. More details of single events selection can be found in the next section.

5.1.2 Single-electron signals in XENON100 experiment

In this section the observation of very low-energy S_2 signals and their origin, as well as the different characteristics used to describe the detector related to the ionization signal will be presented.

Single-electron signals are the smallest S_2 signals that can exist. First selection is done by the threshold implemented at $150pe$ defined by *XS_2peak* cut as we have seen in the previous section. The S_2 signals can be found in the 400µs waveform.

Figure 5.1a shows an example of S_2 signals below $150pe$ resulting from single electrons which also the ZEPLIN collaboration already reported from their studies [51, 52].

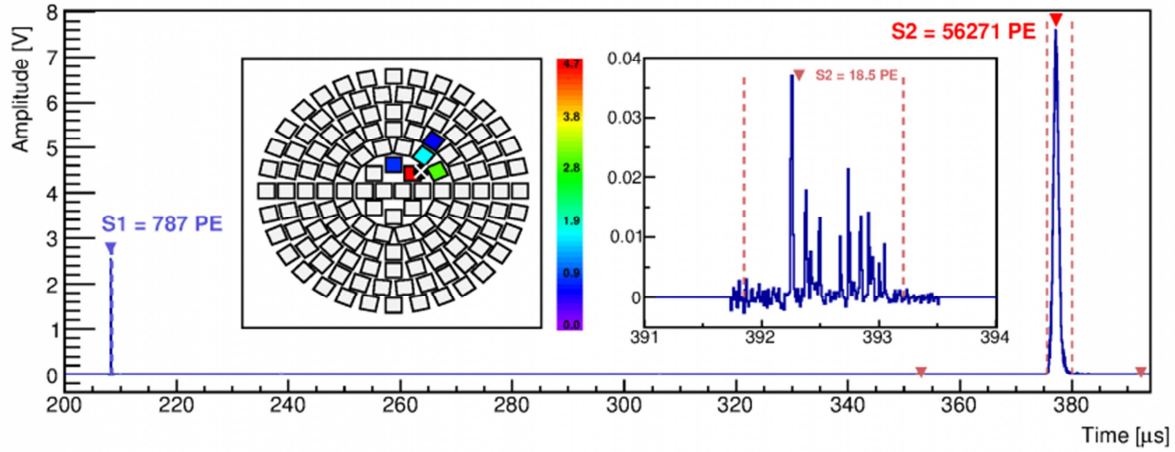

FIG. 5.1a – Example of a waveform containing a single electron signal; two single electrons are observed, one before and one after the main S_2 peak. The single electron signal shown in the zoom and in the top array PMT pattern has $18.5pe$ that corresponds to the average secondary scintillation gain [53].

One of the proofs that the small S_2 signals lower than $20pe$ are real charge signals is their duration around 1µs, comparable with the time needed for an electron to drift through the proportional scintillation gas gap d_g (see figure 4.4a in paragraph 4.2.2).

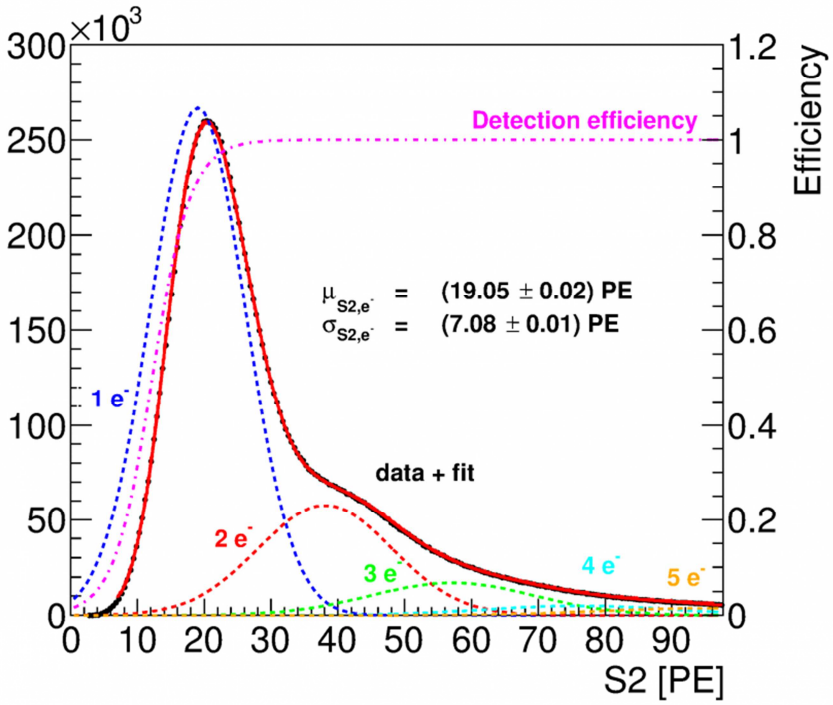

FIG. 5.1b – The low-energy S_2 spectrum [53]

The low energy S_2 spectrum (figure 5.1b) can be fitted using a sum of Gaussian functions, $Gaus(\mu_i, \sigma_i)$ with the constraint $\mu_i = i\mu_1$ and $\sigma_i = \sqrt{i}\sigma_1$, multiplied by an efficiency curve represented by a Fermi-Dirac function (expression 5.1) with A and B as free parameters:

$$f(E) = \frac{1}{\exp\left(-\frac{E-A}{B}\right)+1} \qquad (5.1)$$

This fit can also be interpreted as a sum from one to more electrons, each of them producing an independent S_2 peak, $Gaus(\mu_1, \sigma_1)$. The position of the first Gaussian defines the *secondary scintillation gain*, i.e. the number of photoelectrons per electron extracted in the gas gap. For Run10, the value is ~19pe [53].

5.1.2.1 Single-electron events selection

To select single-electron, two-electron or three-electron signals, cuts on the S_2 size will be applied. Pure samples will be defined by the cut ranges, this means selecting regions from the spectrum where Gaussians do not overlap.

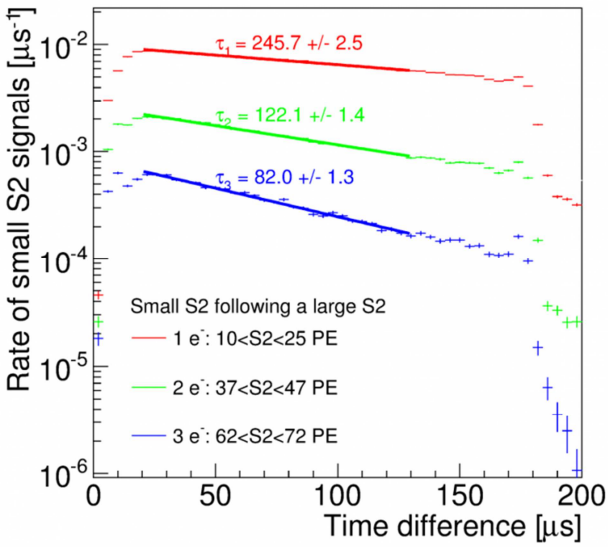

FIG. 5.2a – Distribution of the time difference between the large S_2 and the small S_2 signals for single electron signals (red), two electron signals (green), three electron signals (blue) [53]

The majority of single electrons observed in XENON100 are time correlated with a S_1 or S_2 signal. The time correlation is demonstrated by the end of the time distribution (see figure 5.2a for single electrons which follow an S_2 signal) which ends around $180\mu s$, the maximum drift time, i.e. maximum drift length divided by the drift velocity $(30cm/0.173cm/\mu s)$. By taking data with a trigger located at the beginning

of the waveform it has been demonstrated that the end of the distribution is not an artifact due to the end of the waveform.

The cut efficiencies (acceptances), or probability that a WIMP event will pass the cut, have to be estimated as a function of S_1 and S_2, or equivalently as a function of energy. Since a WIMP data sample to test this does not exist, we need to define a sample from our calibration data as close as possible to WIMPs. To do this, the data from the AmBe calibration were used, to estimate the effect that the single S_2 have on the nuclear recoil band, as a function of energy.

Since WIMPs are expected to generate only single scatter interactions in the TPC, we want to select events fulfilling this condition. Multiple scatter events produce several S_2 peaks in the trace (besides few ones which happen in the same *Z*-plane) which is considered in *XS_2single* cut. We require that a valid event only has a single S_2 peak in the trace. The problem associated with this is that at very low amplitudes, ionization signals from a few electrons (1–3) start to appear which are not due to multiple scatter interactions. Hence, a lower threshold on the size of the 2nd largest S_2 signal in a trace is required in order to have a sizeable acceptance.

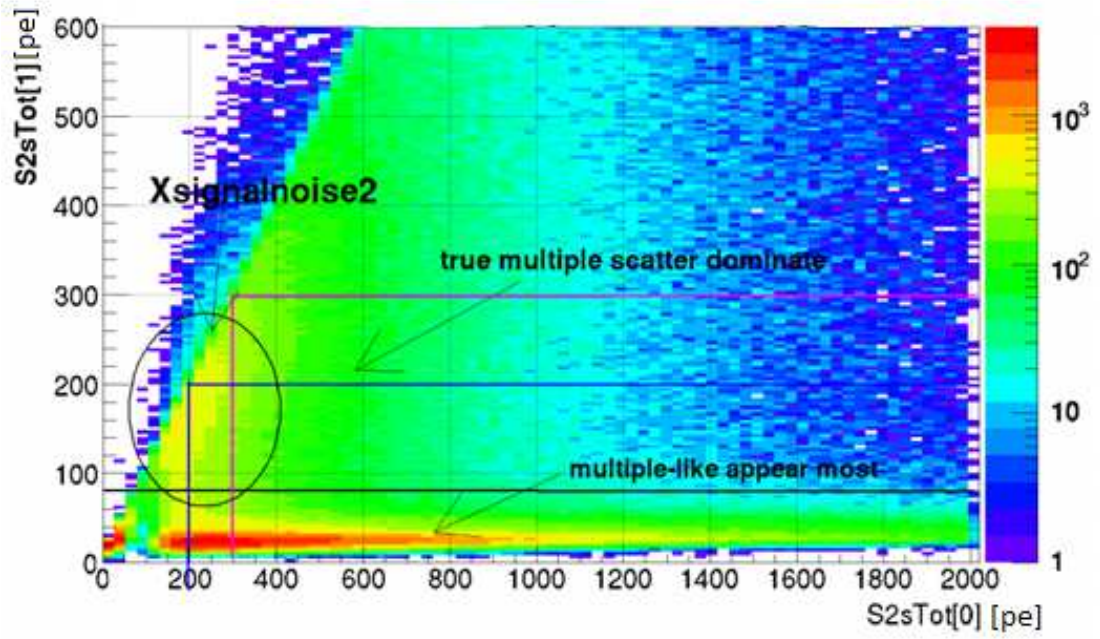

FIG. 5.2b – Energy dependence between the first two S_2 peaks, noted S2sTot[0] and S2sTot[1]

The dependence of the first two S_2 peaks (noted S2sTot[0] and S2sTot[1]) was studied [54]. The strong dependence indicates that a lower threshold cut is more reasonable (see FIG. 5.2b) since previous studies of the analysis group show that 300pe is a too high threshold and we would expect that even for single scatter, there is more than one S_2 peak. But, the S_2 peak of single electrons is less than 100pe mostly, and for

true multiple scatters, the second largest S_2 is much bigger. The size of S_2 for single electrons is almost constant with drift time.

In the figures below, we can see the energy dependent S_2 single for lower threshold cut applied (<100pe). The study shows that the second S_2 is increasing when the first S_2 is increasing (S2sTot[1] is linearly increasing with S2sTot[0] for single scatters).

The cut definition proposed to be used for the selection of S_2 single scatter events requires that the second largest S_2 peak is smaller than ~70 pe (corresponding to ~3.5 electrons), with a slight size dependence on the first S_2 peak.

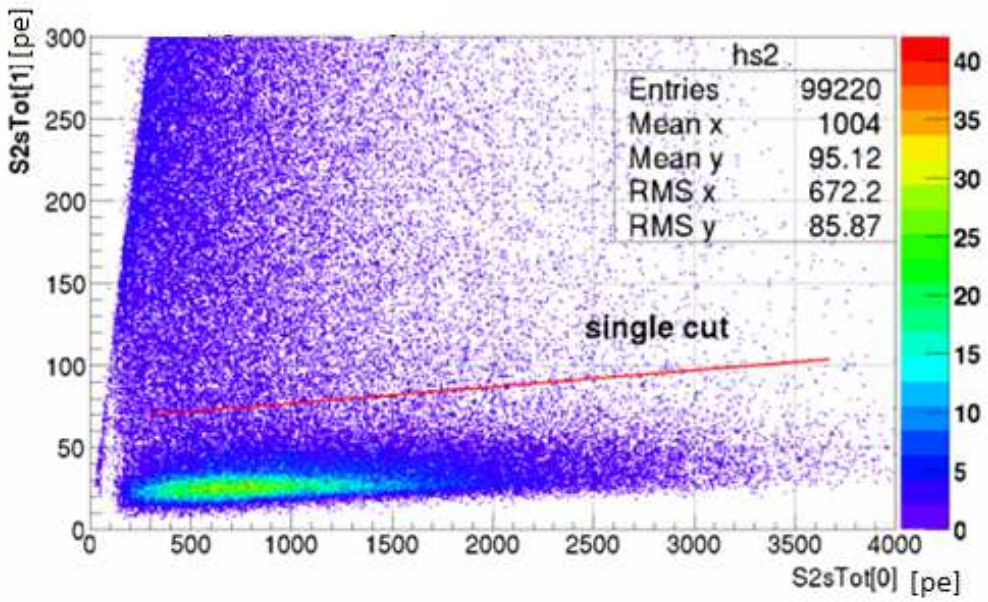

FIG. 5.3.a– Energy dependence between the first two S_2 peaks using low threshold cut

Thus, an energy dependent cut is better than a constant one. In figure 5.3.a we can see the events distributed in two main parts. The upper part is multiple scatter dominated while the lower part is single scatter dominated. To prove this, in figure 5.3.b we got almost the same distribution restricting $dt_1 > 180\mu s$ (where dt_1 is the drift time between the first two S_2 peaks). For this condition we expect the events to be truly single scatter.

Xs2single cut was checked if it´s still appropriate to be used for each data analysis run:

- the cut has the same effect of rejecting the nuclear multiple scatter events and gamma background as much as possible if comparing with previous AmBe data sets [54 – 56] ;

- decreasing the S2sTot[1] threshold (on the second S_2 peak), or cut into other spaces as S_2 width, does not improves the cut acceptance [56 , 57] ;
- the *Xs2single* cut has an improved acceptance for Run10 than for previous Run08 (tested on AmBe calibration data) (see FIG. 5.4);

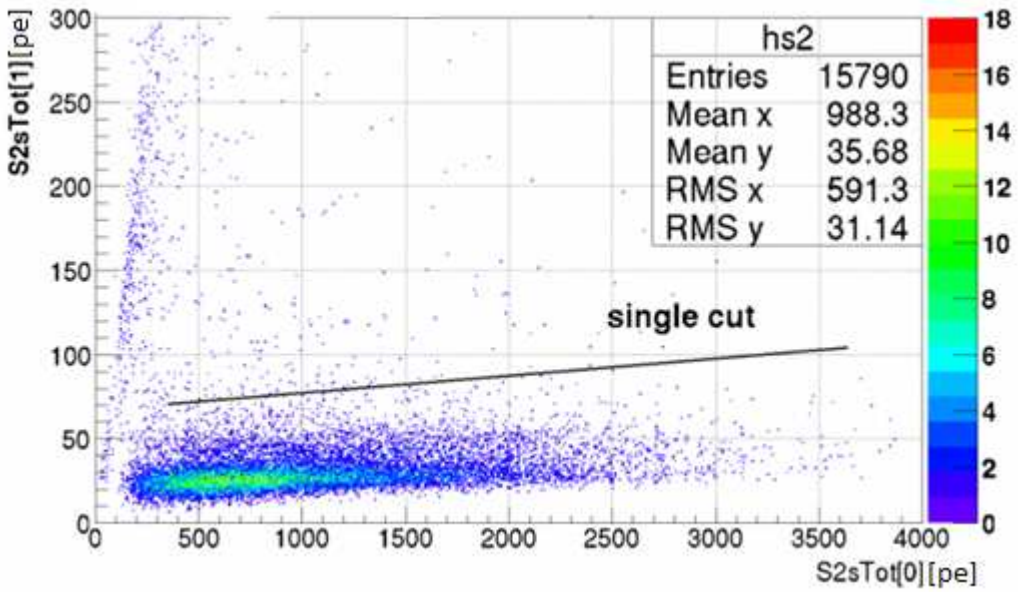

FIG. 5.3.b– Energy dependence between the first two S_2 peaks restricting $dt_1 > 180\mu s$

- the cut acceptance was calculated using all new basic cuts (*Xsignalnoise*, *Xwidth*, *Xs1coin* or *Xs2peaks*) and using the reprocessed data sets [57]; (by reprocessing the data [58], one have to understand some updates and new algorithms integrated into the processor program regarding the S_1 and S_2 map corrections, noise rejection, procedures to handle different PMT gains or event selection for low energy);
- the cut acceptance, i.e. the ratio of events that pass the single cut from all the events, was calculated selecting a region which is single scatter dominated, for $dt_1 > 180\mu s$, where dt_1 is the time difference between the largest and the 2nd largest S_2 (see FIG. 5.5). Due to the maximum drift time of $\sim 180\mu s$, no S_2 peak in this region can come from a double scatter event;
- the averaged acceptances obtained are (99.68 ± 0.26)% [57], using the $cS1sTot[0]$ (corrected S_1) energy range and (99.66 ± 0.18)% [57], using the S_2 energy range (see FIG. 5.6). In the study we are using binomial errors and the acceptance is defined via relation 5.2:

$$acceptance = \frac{number\ of\ events\ (Xs2single\ \&\ dt_1 > 180\mu s\ restriction)}{number\ of\ events\ (dt_1 > 180\mu s\ restriction)} \qquad (5.2)$$

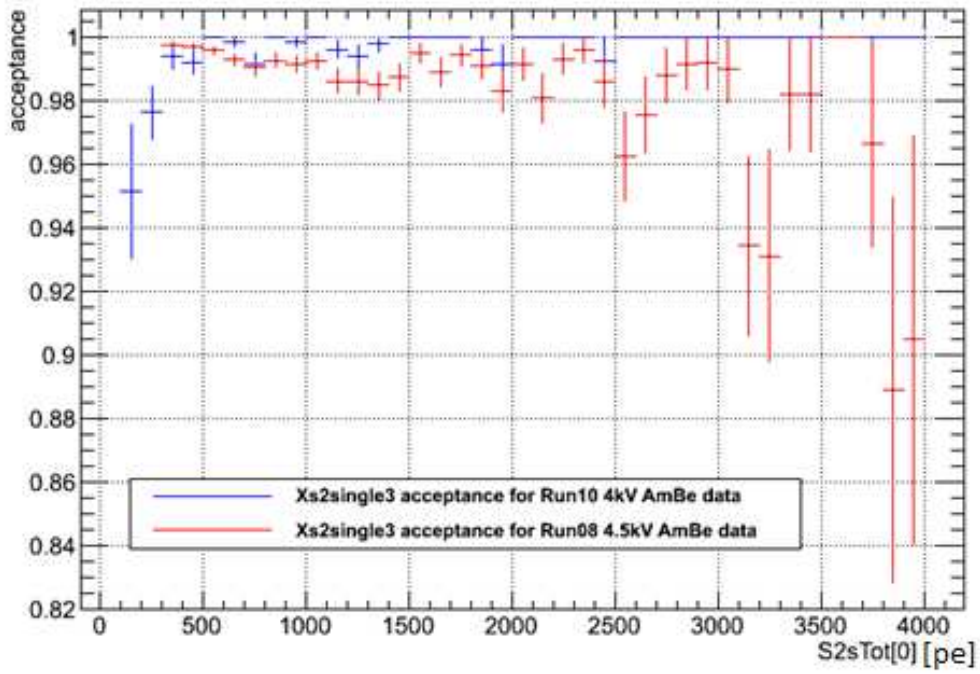

FIG. 5.4 – Comparison of *Xs2single* acceptances as a function of S_2 for Run08 and Run10 AmBe data

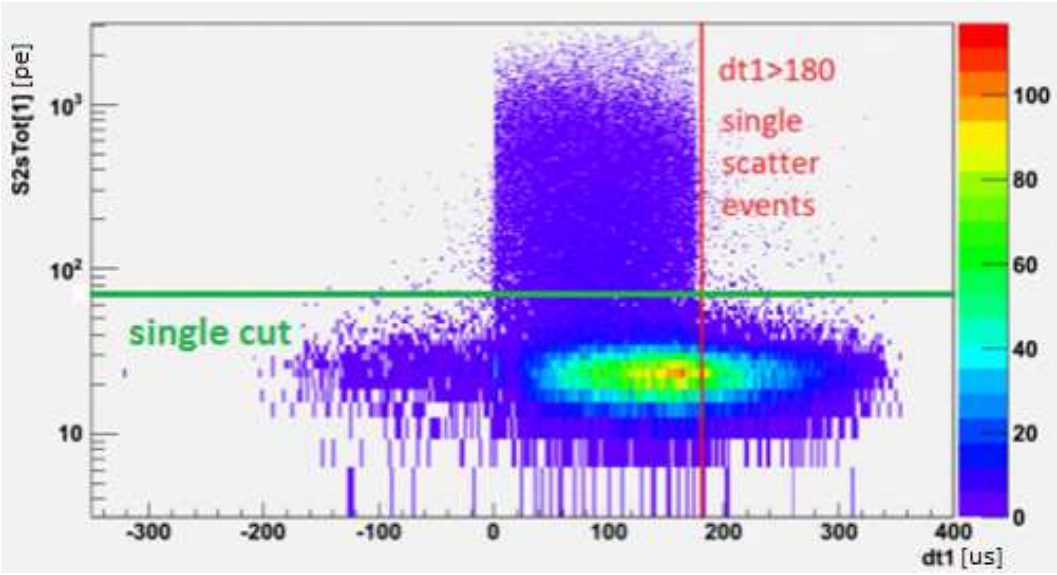

FIG. 5.5 – Scheme of single scatter events selection

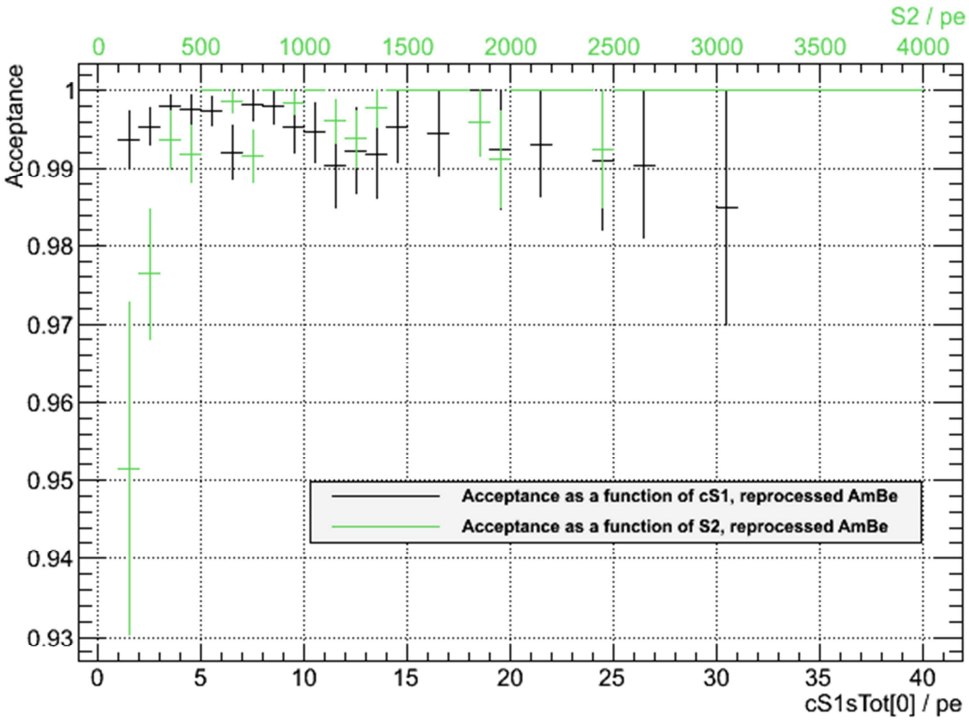

FIG. 5.6 – *Xs2single* acceptances as a function of cS_1 and S_2 for Run10 nuclear recoils data

So *XS$_2$single* cut is developed to remove events with multiple S_2, as would be the case of multiple scatters. As we expect a large number of multiple scatters in the AmBe data that would bias the acceptance computation, we rechecked the acceptance, in this case computing the electron recoil data taken over time [59].

For the case of ER, it is very unlikely to observe a multiple interaction in which the summed S_1 would be in the interest region, and hence we expect to have a much cleaner sample in terms of single scatters. The computed acceptance as a function of S_1, for each 2 photo-electrons for Run08 and for each photo-electron in Run10 is shown below in the figures 5.7a and 5.7b respectively. In this case the acceptance is defined via relation 5.3 and again the better acceptance of the cut for Run10, if comparing with Run08, is proved by using also ER data.

$$acceptance = \frac{number\ of\ events\ (all\ cuts)}{number\ of\ events\ (all\ cuts\ \ without\ Xs2single)} \qquad (5.3)$$

From studies motivated by data/MC comparisons [60], there seems to be an indication that a fraction of ~10% of double-scatter events survives the cut for NR data. However, since it is basically impossible for low energy electronic recoils to produce low energetic double scatters, this only affects the neutron background, which would

then be a bit higher than necessary (since not all double scatters are removed). However, since the neutron background in the present data taking run is still the smallest fraction of the total background, a change of ~10% is not relevant.

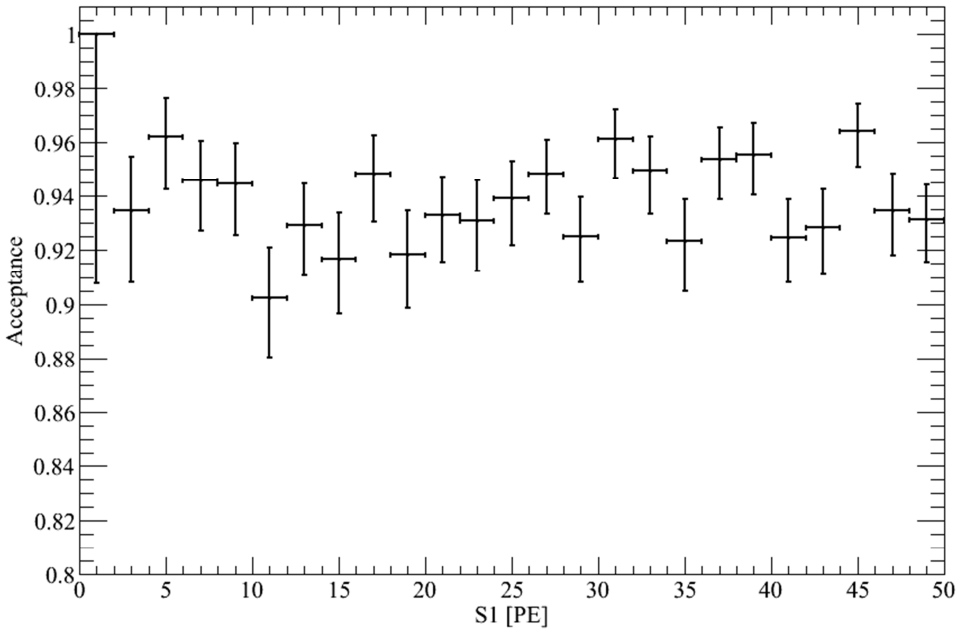

FIG. 5.7a – *Xs2single* acceptance as a function of S_1 for Run08 electronic recoils calibration data

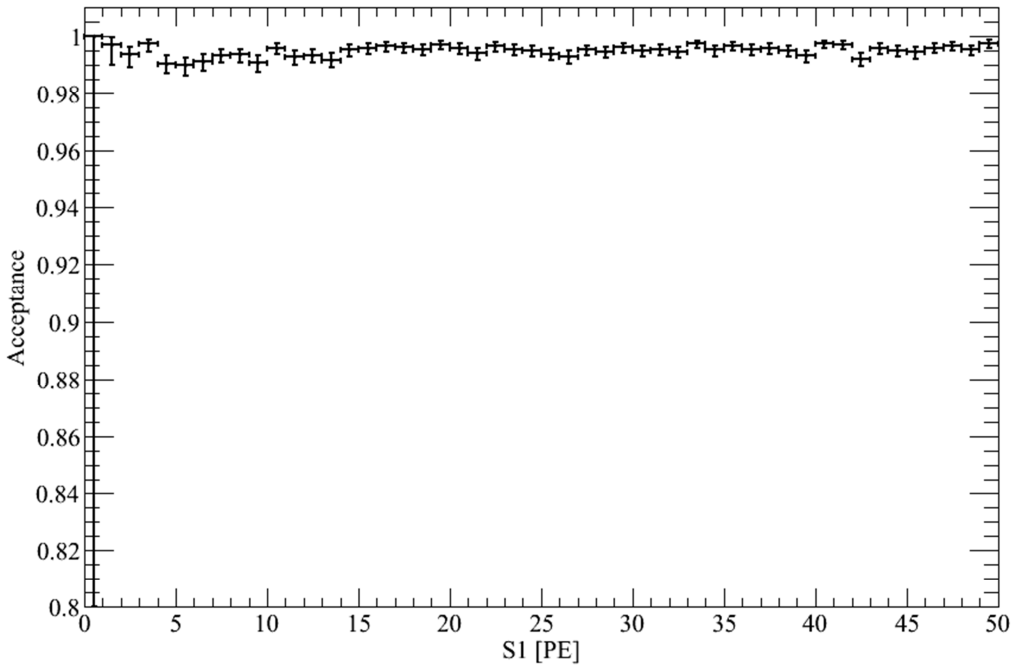

FIG. 5.7b – *Xs2single* acceptance as a function of S_1 for Run10 electronic recoils calibration data

5.1.2.2 Origins of single-electron signals

From all the studies reported in the previous section, we can draw several conclusions regarding the several possible origins of the single-electron signals.

Most of the small S2 signals are induced by primary or secondary scintillation photons. This is the only way to explain the time distributions shown in figure 5.2a. Delayed extraction of electrons at the interface liquid-gas (i.e. electrons which would be trapped at the liquid surface and extracted later than the main part of the electron cloud) could explain the exponential decrease for single electrons following the S2 signal but not the sudden end at a time corresponding to the maximum drift time.

Scintillation photons can induce electrons by photoelectric effect and one photon can only generate one electron. It is compatible with our observations since all small S2 signals are single electrons or accidental coincidences of single electrons, as we showed in previous section.

We observe, as expected from the previous conclusions, a proportionality of the relative rate of small S2 signals with the largest S2 size. From the proportionality coefficient and taking into account the mean collection efficiency in XENON100 (~20% from MC simulation) and the averaged PMT quantum efficiency (~25%), we conclude that about 50000 secondary scintillation photons are needed in average to produce one single electron. The non-zero ordinate at the origin, corresponding to an average of 0.3 additional single electrons, corresponds to single electrons which are either induced by the S1 photons or not induced by any photon [53].

The dominating responsible for the photo-ionization process are the impurity molecules in liquid xenon. There are several candidates for the photo-ionization process: xenon, impurity molecules (O_2, N_2, …) contained in the xenon at the ppb level or the metal components (grid, cathode, field rings,…). Among impurity molecules, the negative ions O_2 are the best candidates. Given the VUV photon energy $\sim 7eV$, the negative ions O_2 created by drift electrons attachment are the best candidates, being the needed energy $\sim 0.45eV$, while the first ionization energies of O_2 and N_2 are above $12eV$ [61 – 63]. However, since the cross sections and the number of ions are unknown, it is not possible to make any quantitative statement. We cannot exclude photo-ionization of other chemical species. Another source comes from photoelectric effects on the copper of the 40 field shaping rings and on the stainless steel of the cathode.

The multiple scatter events that have only one scintillation pulse (S_1) and ionization pulse (S_2) are categorized as *anomalous single scatter events*. The S_2/S_1 ratio for these events is lower than the ratio expected for the single scatter events or for a WIMP interaction. Therefore, for a sensitive dark matter search, it is essential to specially analyze, identify and reject this category of events. The estimation of the number of anomalous single scatter events in XENON100 dark matter datasets was done by a Monte Carlo study validated with data from gamma calibration [64].

5.1.2.3 Secondary scintillation gain and yield using single-electrons

The single-electron signals can be also used to study the TPC characteristics in terms of *secondary scintillation gain*, G, i.e. the total number of photoelectrons, measured with all the PMTs per electron extracted into the gas gap. The gain is related to the *secondary scintillation yield*, Y i.e. the number of emitted photons per electron extracted into the gas gap, the *mean collection efficiency* of photons emitted from the gas gap, $\bar{\beta}$ and the *mean PMT quantum efficiency*, $\bar{\eta}$ as written in expression 5.4 below:

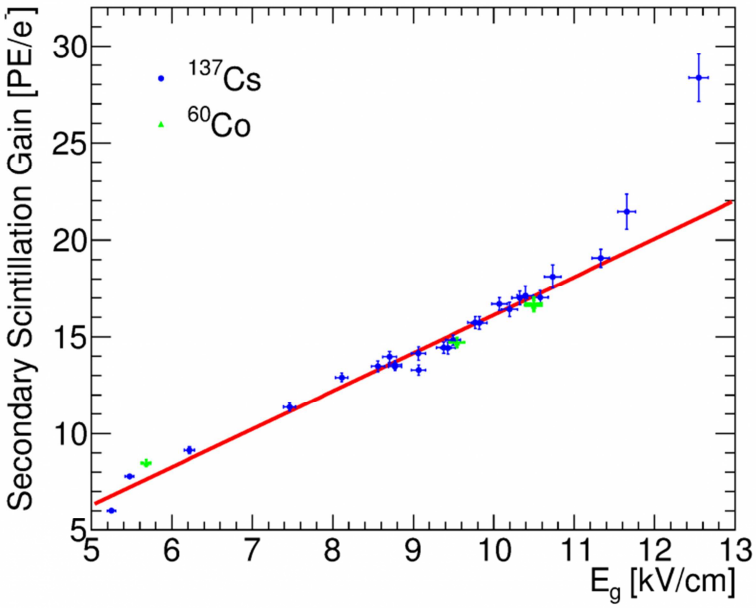

FIG. 5.8 – XENON100 secondary scintillation gain as a function of the electric field in the gas gap; the highest values which does not follow the linear trend are due to electron multiplication [53]

$$G(E_g, P_g, d_g) = Y(E_g, P_g, d_g)\bar{\beta}\bar{\eta} \qquad (5.4)$$

where E_g, P_g and d_g are the gas gap electric field, pressure and liquid xenon height respectively, according to the following expression:

$$Y = \left(a\frac{E_g}{P_g} + b\right) d_g P_g \qquad (5.5)$$

Figure 5.8 shows the secondary scintillation gain as a function of the electric field using calibration data (^{137}Cs and ^{60}Co). The values for parameters a and b obtained from the fit presented in the figure above are in good agreement with values from the literature [33]:

$$a = (152 \pm 19) photons/e^-/kV \text{ and } b = -(151 \pm 20) photons/e^-/cm/bar$$

Calculating then the values for secondary scintillation gain, the values obtained are $18.70 \pm 0.45\, pe$ and $19.70 \pm 0.16\, pe$ for Run08 and Run10 respectively [53] and the difference come from different gas gap height and anode voltage.

5.1.3 *Hot Spots* monitoring

After the acquisition of each dark matter dataset we have to check the status of the files. From the beginning of the experiment we could identify and study several regions with an increased number of S_2 peaks. These regions can be easily identified if we plot an X-Y map of the TPC (as in figure 5.9 below) and we will call them *hot spots*.

Most of the hot spots appear in some runs but not others. For these reason, we tried to classify them.

The first class is defined by a region (near $X = 20mm$ and $Y = -4mm$) that appears *hot* in all runs. This persistent hot spot is characterized by waveforms which arrive early, are relatively wide, but with very low amplitude and low S_2 yield. In figure 5.9 we can see a representative plot of the number of observed S_2 peaks in the X-Y plane, using data from Run10 of the XENON100 experiment, while in figure 5.10 we can see the projections along the X and Y axis that motivate the choice for a reference function that can be written as [65]:

$$f(x,y) = p_0 \times x^2 + p_1 \times x \times y + p_2 \times y^2 + p_3 \times x + p_4 \times y + p_5 \qquad (5.6)$$

so it is a parabolic function that will accurately describe the shape of the distribution. Performing a fit in a region without hot spot, will remove the central hot spot present in all the runs.

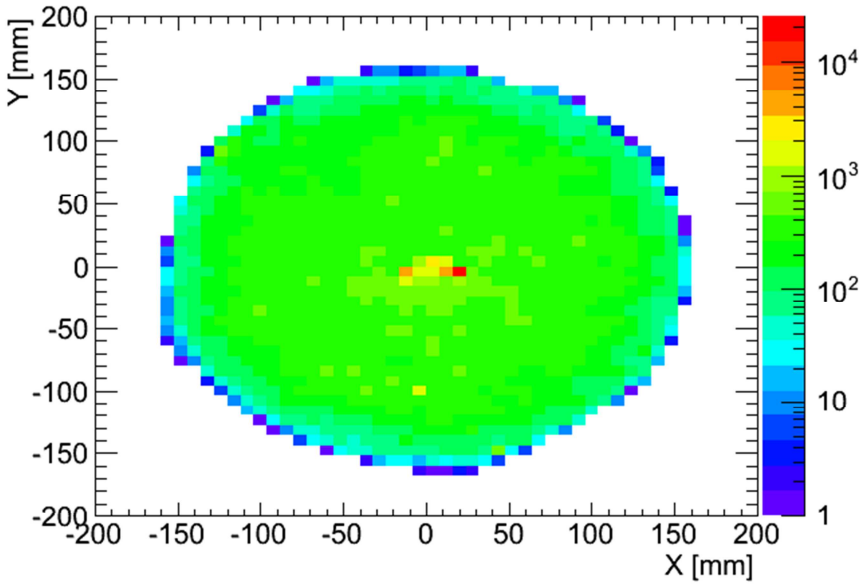

FIG. 5.9 – Example of central hot spot present in all the runs

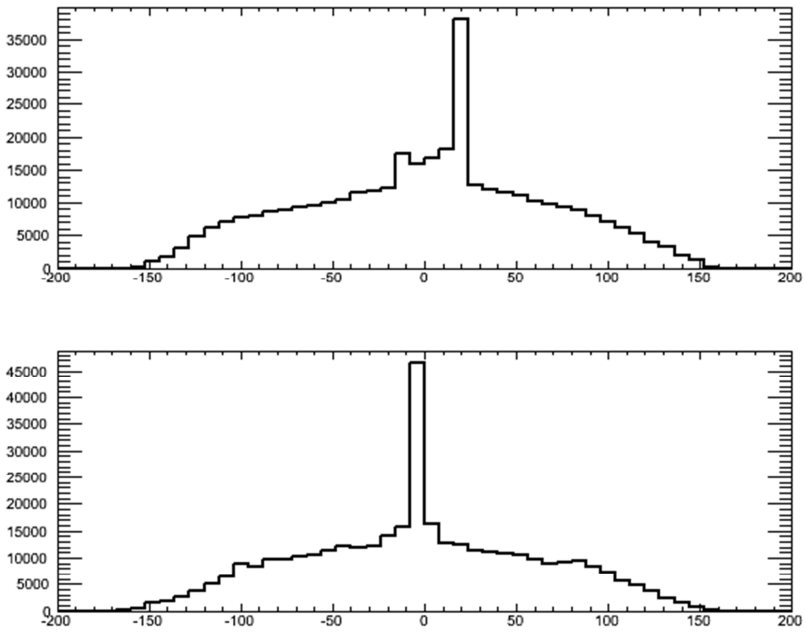

FIG. 5.10 – Projections along the X and Y axis

The detector stability in time is assessable with this method so, each run is analyzed with the same functional form. Another issue observed also in previous analyses shows that hot spots may be differentiated by a low total S_2 yield than other regions of the detector or by an anomalous ratio of S_2 signal in the top PMT array to S_2 signal in the bottom PMT array.

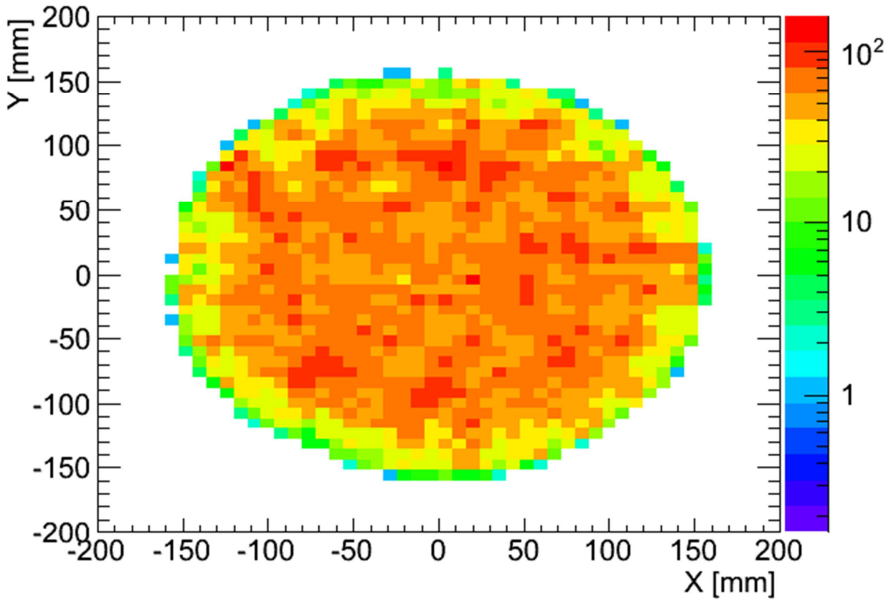

FIG. 5.11 – X-Y map after removing the central hot spot

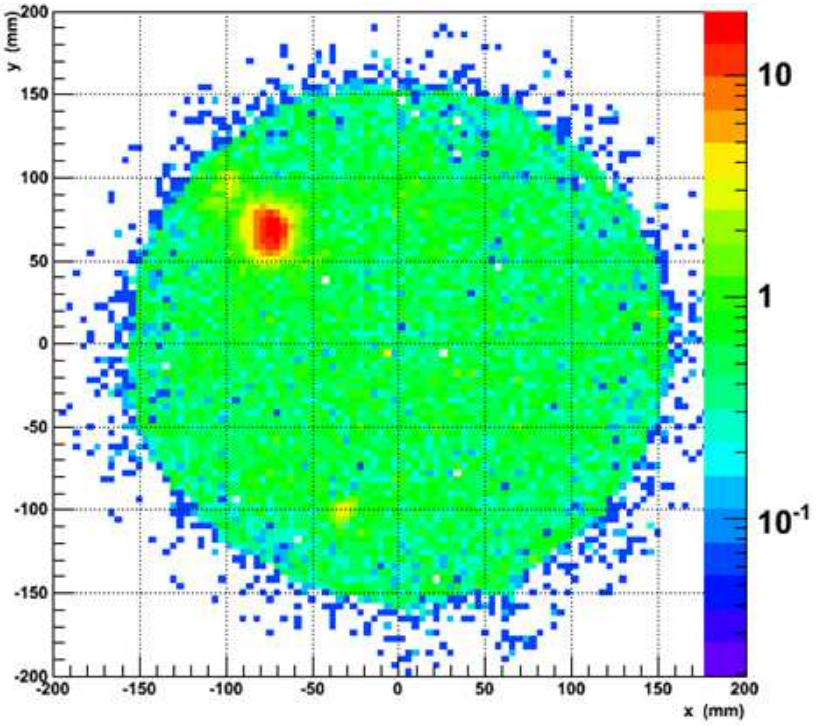

FIG. 5.12 – Example of a transient hot spot

If we require $S2 > 800pe$ and if the additional requirement $S2Top/S2Bottom > 0.2$ is applied then it is observed that all hotspots are removed. The result after this cut is relatively nice, uniform yield, as you can see in figure 5.11.

The other class of hot spots, are transient hotspots that occur elsewhere in the detector and generally are not present in all the runs but in a few datasets. An example can be visualized in figure 5.12. This kind of hot spots monitored during the operation of the detector, locally at LNGS, are due to unexplained increased data acquisition rates or changes in few of the parameters values settings. After investigating a set of distributions for S_2 peaks in the hot spots regions and the rest of detector, we can better understand them. If we have a look to the waveforms responsible for the hot spots, we can consider the S_2 peak position, S_2 peak width at 50% height and S_2 peak height. The peaks that create the hot spots are generally shorter, wider and occur earlier in the readout window. If we examine also which PMTs are responsible for the signal observed in the hotspot, by integrating yield of pe's as a function of PMT number for the S_2 peaks, it results that most of the pe's are measured by a single PMT. Finally, if we try to reconstruct the Z-coordinate of the S_2 signal for the events in the hotspots and the rest of the detector we can see that S_2 peaks in the hot spots occurs preferentially at $Z = 0$ (the LXe level) so probably no presence of S_1 for these events.

Hot Spots it's a subject in continuous study, to better understand what they are telling us about our detector and data. It is clear that all the hot spots should be removed

before the unblinding of dark matter data, as well as all the instable periods that could confuse a better and precise result of *what's left.*

5.1.4 The cut acceptance variation for background modulation analysis

The aim of this study is to independently derive the acceptance variation for all the cuts defined for XENON100 analysis then, make a statistical test on the average cut acceptance variation and see if it's needed to include this factor in the Profile Likelihood analysis of background rate for the un-blinding of dark matter datasets.

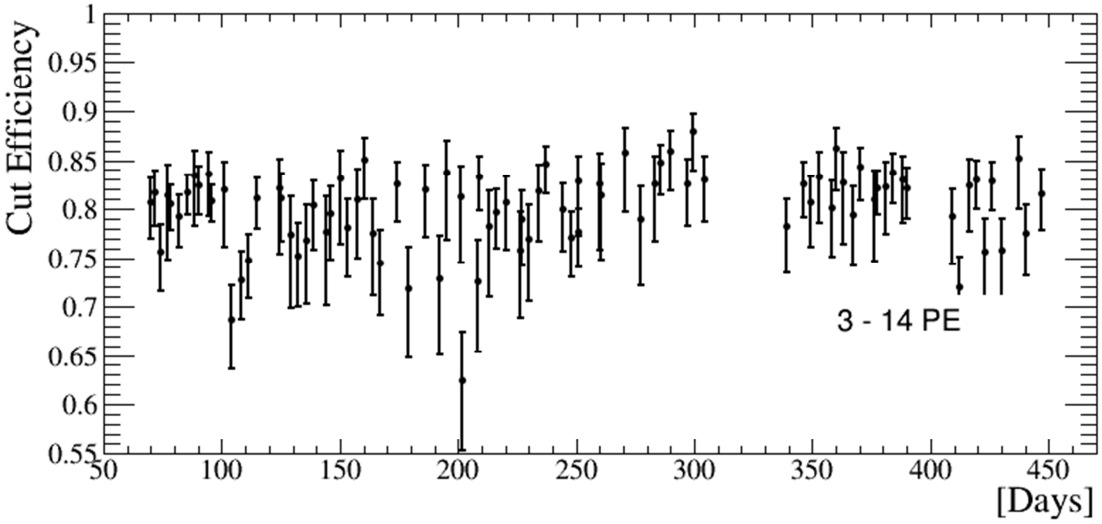

FIG. 5.13a – The average cut acceptance (3-14pe) for each data set

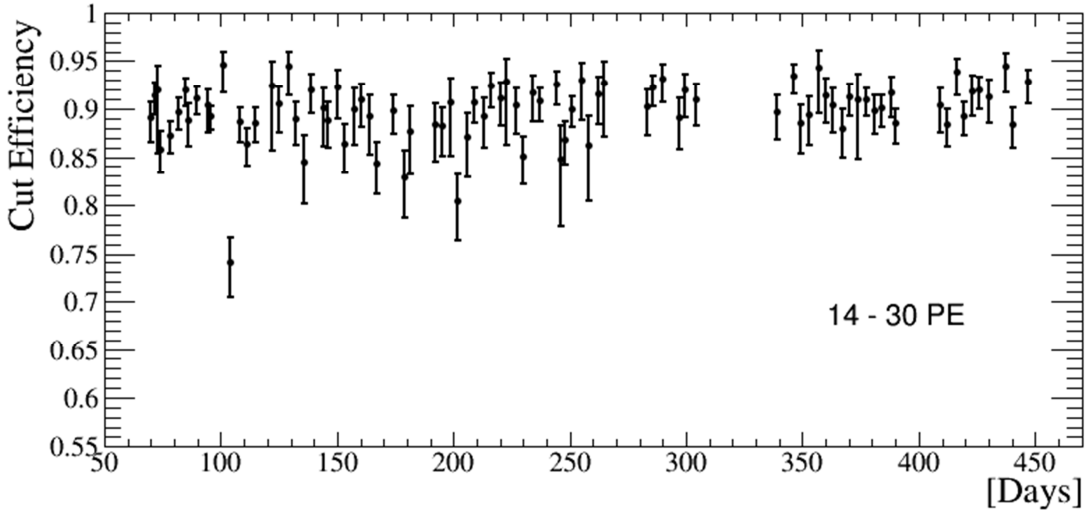

FIG. 5.13b – The average cut acceptance (14-30pe) for each data set

Assuming that each cut is independent, in this case the acceptance for each cut and for each dataset have been calculated accordingly to relation 5.7, then the average cut acceptance of all the cuts and for each data set has been determined using a simple error propagation (up and down separately). In figures 5.13a and 5.13b we can see the average acceptance variation calculated using electronic recoil calibration data and plot as a function of each dataset acquisition date (day of the run) and for two different energy ranges, (3-14pe) and (14-30pe), respectively.

$$acceptance = \frac{number\ of\ events\ (all\ cuts)}{number\ of\ events\ (all\ cuts\ \ without\ cut\ under\ study)} \qquad (5.7)$$

The average acceptances derived here are compatible to what is used for the Profile Likelihood analysis. Since the acceptance is derived in the binned approach, a binned likelihood χ^2 analysis is used to identify the temporal variation and set limits on the parameters.

For cut stability analysis we are most interested in the relative variation. So the modulation hypothesis to be tested can be expressed as:

$$f(t) = acc(t) \times \left\{C + A \times cos\left[2\pi \times \frac{(t-\Phi)}{P}\right]\right\} \qquad (5.8)$$

where $acc(t)$ is the average cut acceptance from the measurements above and for the corresponding energy range, C is the average event rate, A is the modulation amplitude with period P and phase Φ. Then we fit the cut efficiency variation to the function and calculate the χ^2 after the fitting.

At each frequency, the statistic test

$$\Delta\chi^2 = \min_C[\chi^2(A = 0, C)] - \min_{A,C,\Phi}[\chi^2\ (\mathrm{A}, \mathrm{C}, \Phi)] \qquad (5.9)$$

equivalent to the $-2\log(\frac{L_0}{L_1})$ is used to quantify the significance to reject null hypothesis H_0 (a constant rate adopted to test the temporal stability of low energy ER data). The sinusoidal rate variation formulated in relation 5.5 is an alternative hypothesis H_1, tested by DAMA/LIBRA, CoGeNT and CDMS-II experiments too. $L_0(C_0)$ and $L_1(C_1, A, \Phi)$ are the likelihoods for H_0 and H_1 respectively.

Scanning χ^2 around its minimum for a fixed modulation frequency $\frac{2\pi}{365.25\ days}$, allows the determination of the confidence levels on modulation amplitude, with other parameters to be optimized. Specifically, 3σ and 5σ upper limits can be derived.

Using the statistical technique described above, the corresponding χ^2 curves as a function of modulation amplitude are shown in figure 5.14a and 5.14b, for both energy ranges. The allowed sinusoidal variations of the cut acceptance for a fixed period of 1 year have been extracted.

The 3σ and 5σ upper limits on the modulation amplitude of acceptances in the low energy region (3-14pe) are 0.025 and 0.042 respectively. In the higher energy

region (14-30pe), the corresponding limits are 0.0145 and 0.0245 respectively. In both of the two energy ranges, the modulation amplitudes on acceptances are much smaller than that of total event rates. The best fit modulation amplitudes of these variations as a function of dataset acquisition date (day of the run) are shown in figures 5.15a and 5.15b for both energy ranges. The identified modulation amplitudes are $(3.3 \pm 0.8)\%$ and $(1.4 \pm 0.4)\%$ in the 3-14pe and 14-30pe energy ranges respectively. Thus in the profile likelihood analysis of background rate variation, we don't need to consider the contribution of cut acceptance variation in time.

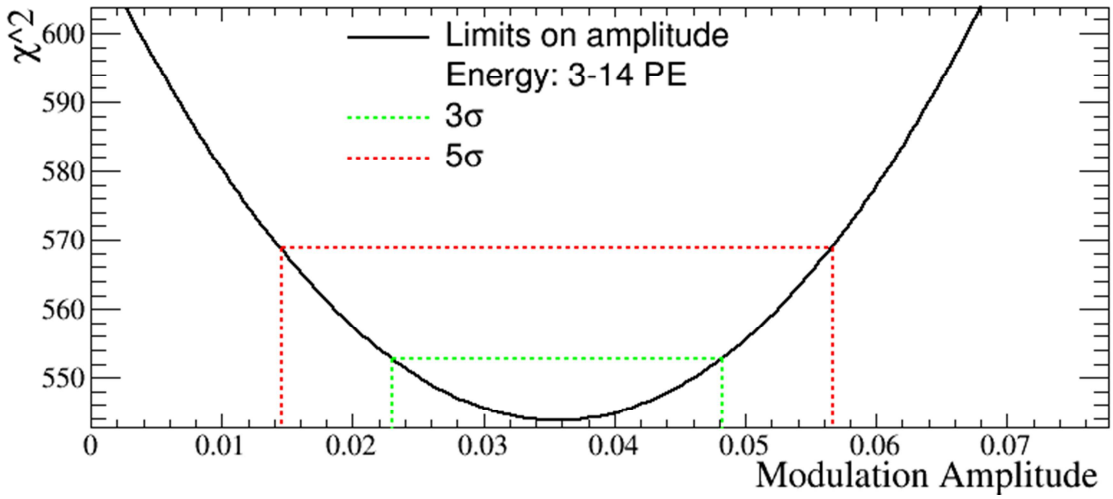

FIG. 5.14a – χ^2 curve as a function of modulation amplitude for 3-14pe energy range

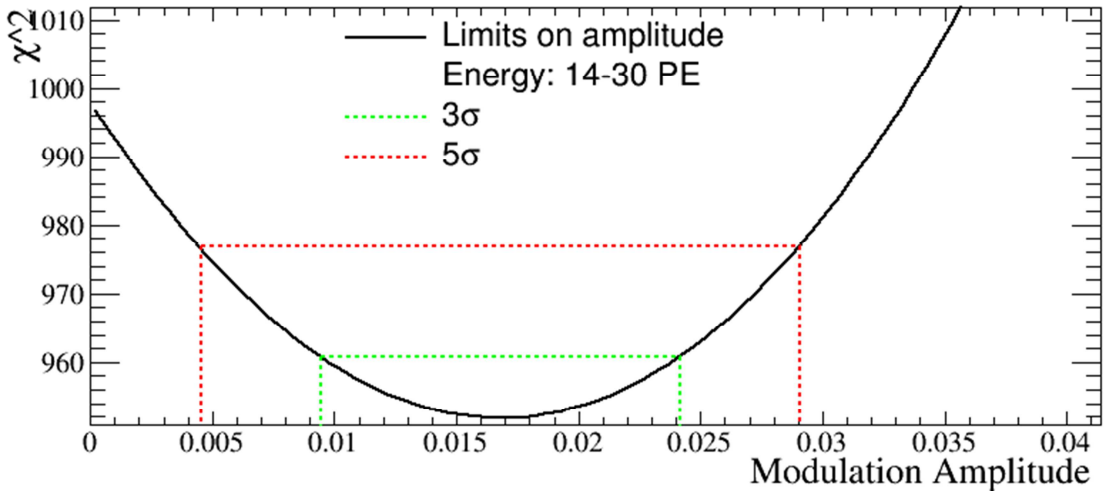

FIG. 5.14b – χ^2 curve as a function of modulation amplitude for 14-30pe energy range

The study presented in this section confirms no significant annual modulation of average cut acceptances for low energy range, so the upper limit on the amplitude of a

time varying XENON100 signal for one year and for low energy single scatter data corresponds to $0.32 \pm 0.01\ events/day$ [66]. The resulting 3σ and 5σ upper limits for the low energy range are 0.61 and $0.80\ events/day$, respectively. Monte Carlo simulations show that an annual modulation with an amplitude greater than $0.43\ events/day$ is expected to be identified at an average confidence level greater than 3σ, and that the data can constrain any modulations with a period smaller than 500 days [66]. XENON100 detector is the first long-term stable noble gas dual phase detector and the low energy single scatter background rate is independent of any detector operation parameter or known radioactive background. In this sense the upper limit on the annual modulation amplitude derived for XENON100 constrains the interpretation of DAMA/LIBRA and CoGeNT signals due to WIMP interactions at more than 5σ confidence levels [66].

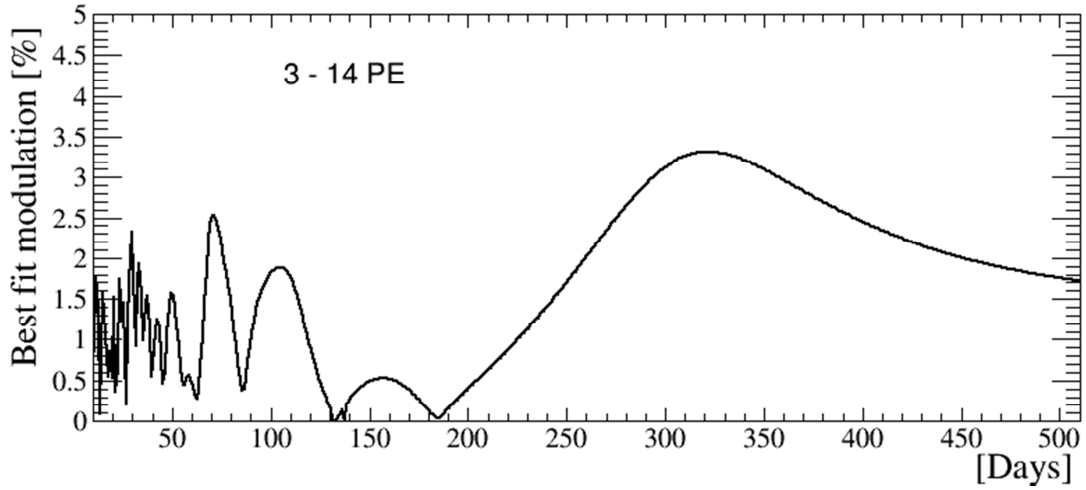

FIG. 5.15a – Best fit modulation as a function of data tacking date for 3-14pe [66]

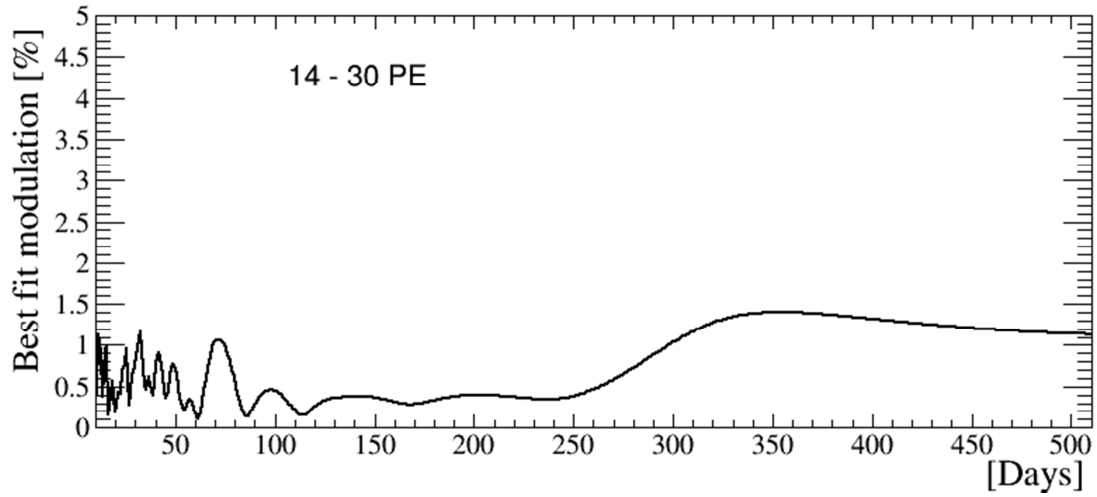

FIG. 5.15b – Best fit modulation as a function of data tacking date for 14-30pe [66]

5.2 Published results of dark matter data analysis

5.2.1 11 live days of dark matter data (Run07)

The first dark matter analysis with 11.17 live days of XENON100 background data acquired between October 20th 2009 and November 12th 2009 (Run07 commissioning run) was carried out to test the potential of the detector and to confirm the Monte Carlo prediction for the single scatter electronic recoil rate at low energies. Only for this run the dark matter data acquired was not formally taken in a blind mode i.e. events from a predefined signal region to be inaccessible. The data selection cuts were derived from ^{60}Co and AmBe calibration data.

For this run, the cumulative software cut acceptance for single scatter nuclear recoils varies between 60% for 8.7keV$_{nr}$ and 85% for 32.6keV$_{nr}$ [49]. For this energy range 22 events are observed but none in the pre-defined signal acceptance region (see figure 5.16 below).

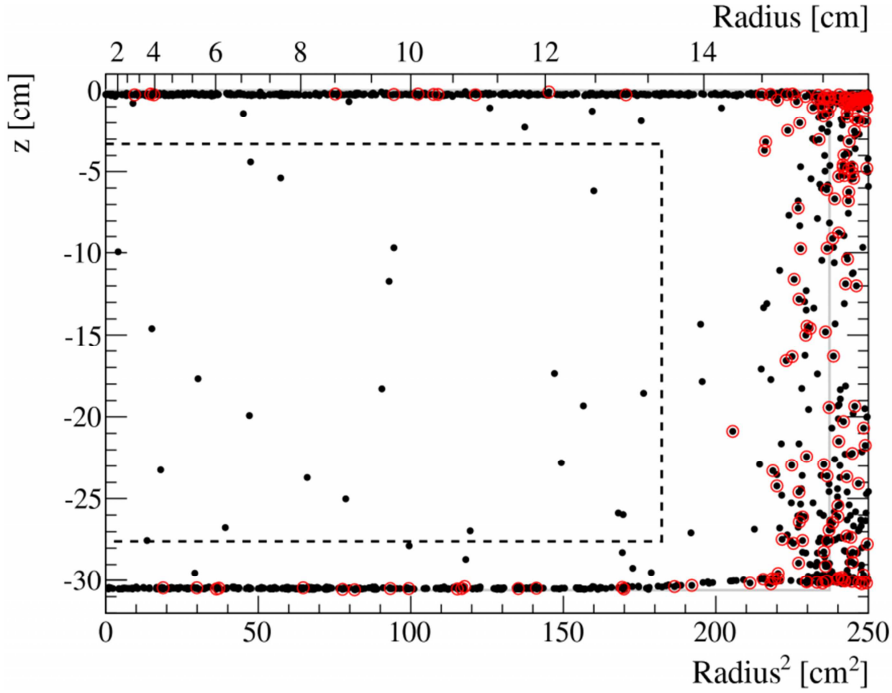

FIG. 5.16 – All the events (dots) in the TPC (gray line) and events below the nuclear recoil median (red circles) present in 8.7 – 32.6 keV$_{nr}$ energy range for 11.17 live days of data; In the 40kg fiducial volume (dashed line) no events below the nuclear recoil median are observed [42]

The upper limit on the spin-independent WIMP-nucleon elastic scattering cross section is derived based on the standard halo assumptions and considering an S_1 resolution dominated by Poisson fluctuations and constant $\mathcal{L}_{eff}$ below 5 keV$_{nr}$ from the global fit. In figure (FIG. 5.17) the result of the spin-independent elastic WIMP-nucleon

cross section exclusion limits with the minimum value of $3.4 \times 10^{-44}\, cm^2$ for a WIMP mass of 55 $GeV/_{c^2}$ [49] is shown in comparison with the other dark matter experiments running on that time.

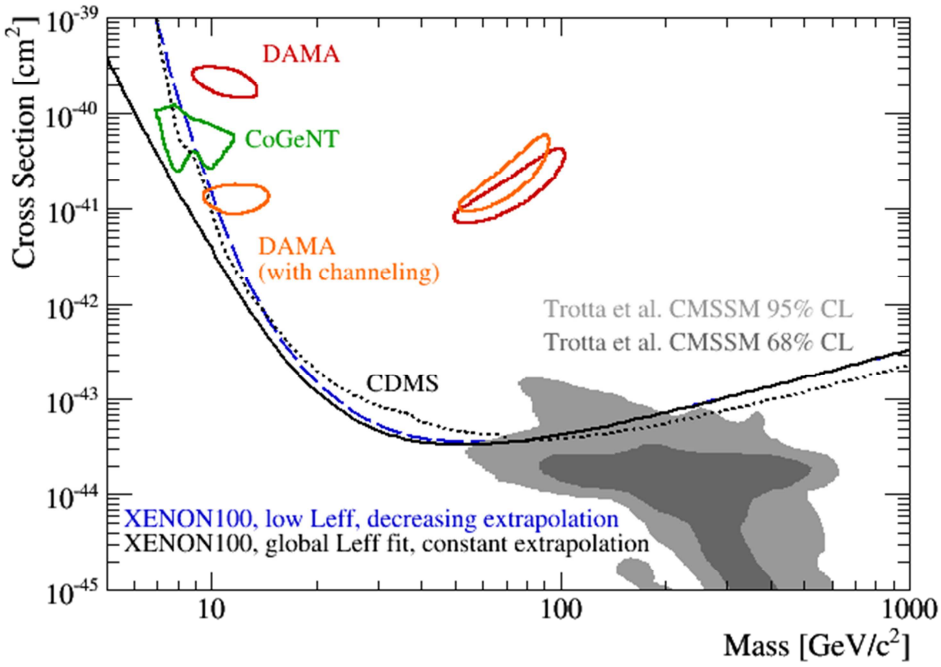

FIG. 5.17 – Spin-independent elastic WIMP-nucleon cross section (solid line) for 11.17 live days of XENON100 dark matter data [42]

Anyway, since XENON100 is massive, the sensitivity of this limited data sample is competitive with other dark matter searches and also demonstrates the low background operation of the detector and its potential to discover WIMP dark matter.

5.2.2 100 live days of dark matter data (Run08)

In this paragraph the most important results of a WIMP search using 100.9 live days of data, acquired between January and June 2010, is reported.

The energy window for the WIMP search (or the blinded energy region of the data sets) is chosen between 4 – 30pe, corresponding to 8.4 – 44.6keV$_{nr}$ based on the $\mathcal{L}_{eff}$ parametrization.

The parameter $\log_{10}(S_{2_b}/S_1)$ where S_{2_b} is the sum of bottom PMT signals, is used to discriminate the electronic recoils from the nuclear recoils. The fiducial volume was optimized on electronic recoil background data and set to 48 kg and the electronic recoil rejection level set to 99.75%. The acceptance to nuclear recoils is determined from AmBe data and the Profile Likelihood approach tests the full S_2/S_1 space.

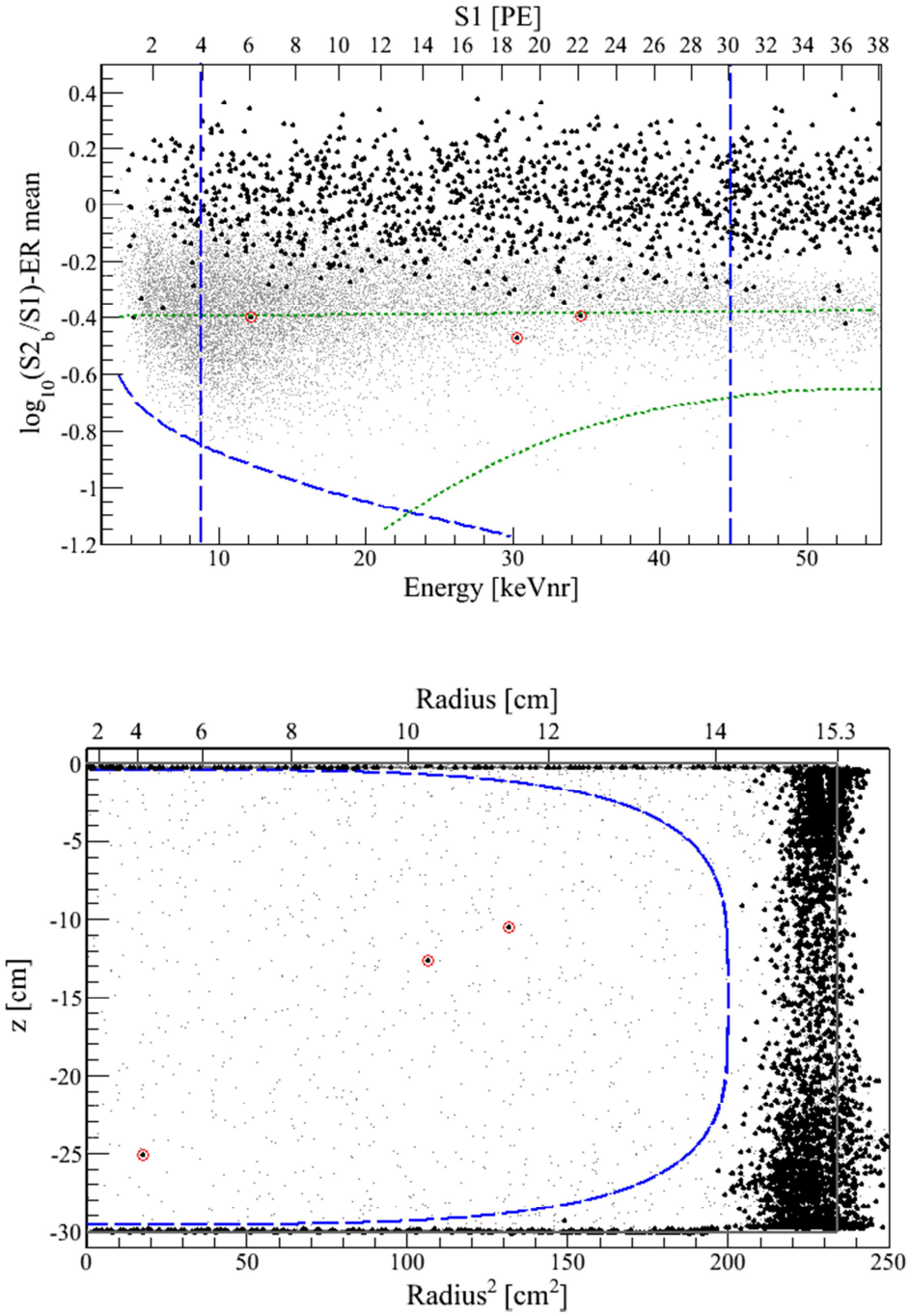

FIG. 5.18 – Up: discrimination parameter as a function of nuclear recoil equivalent energy; black dots indicate the ER band and gray dots indicate the NR distribution measured with AmBe neutron source; blue dashed line indicate the WIMP energy region defined and the green dotted line indicate the 99.75% rejection level; the 3 red circles are the events falling into the WIMP search region; down: distribution of the events in the 48kg fiducial volume (blue dashed line) [42]

In the figure 5.18, is presented the events distribution using the discrimination parameter as a function of nuclear recoil equivalent energy and subtracting the electronic recoil band mean. The total background prediction in the WIMP search region is $1.8 \pm 0.6\ events$ [30].

After unblinding the three events pass all quality criteria for single scatter nuclear recoils and fall into the WIMP search region, but this observation does not constitutes evidence of dark matter since the probability of resulting 3 events is only 28%.

The resulting 90% confidence level (CL) exclusion limit is presented in figure 5.19 below and the minimum value of the spin independent elastic WIMP-nucleon cross section is determined to be $7 \times 10^{-45}\ cm^2$ for a WIMP mass of 50 $^{GeV}/_{c^2}$ [30].

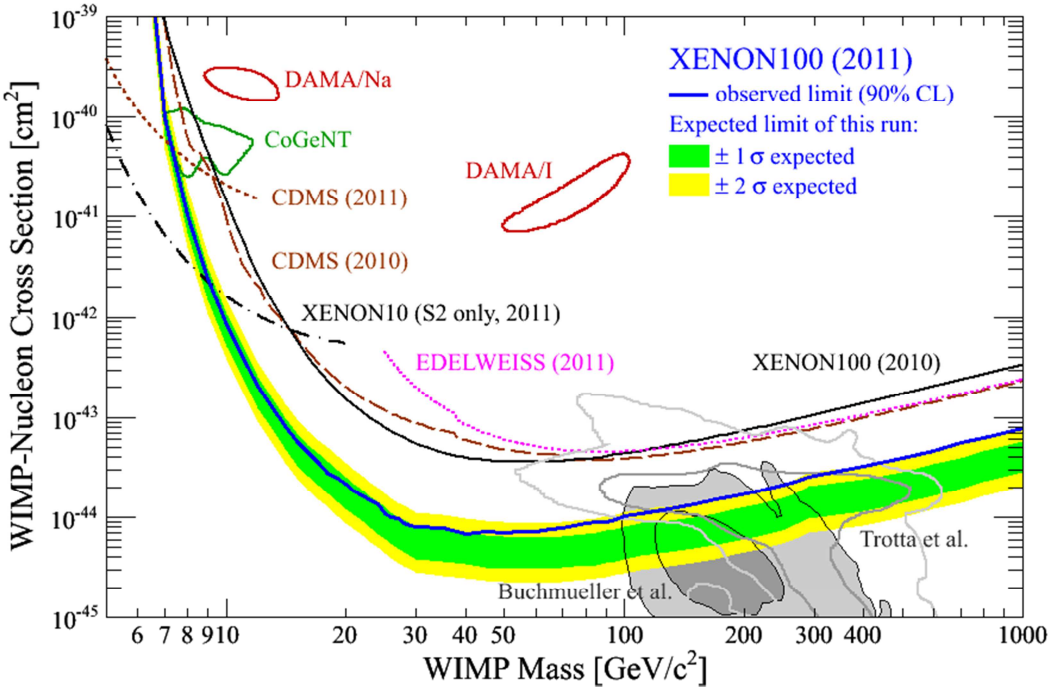

FIG. 5.19 – Spin-independent elastic WIMP-nucleon cross section (solid blue line) for 100.9 live days of XENON100 dark matter data; the green/yellow band indicates the 1 and 2 sigma expectancy of the curve [42]

5.2.3 225 live days of dark matter data (Run10)

Using the same technique as in the previous run, Run10 hunted for dark matter particles at LNGS for 13 months during 2011 and 2012. The blind analysis of 224.6 live days of dark matter data in the 34kg fiducial volume defined has yielded no evidence of dark matter in the 6.6 – 30.5keV$_{nr}$ energy range (3-20pe).

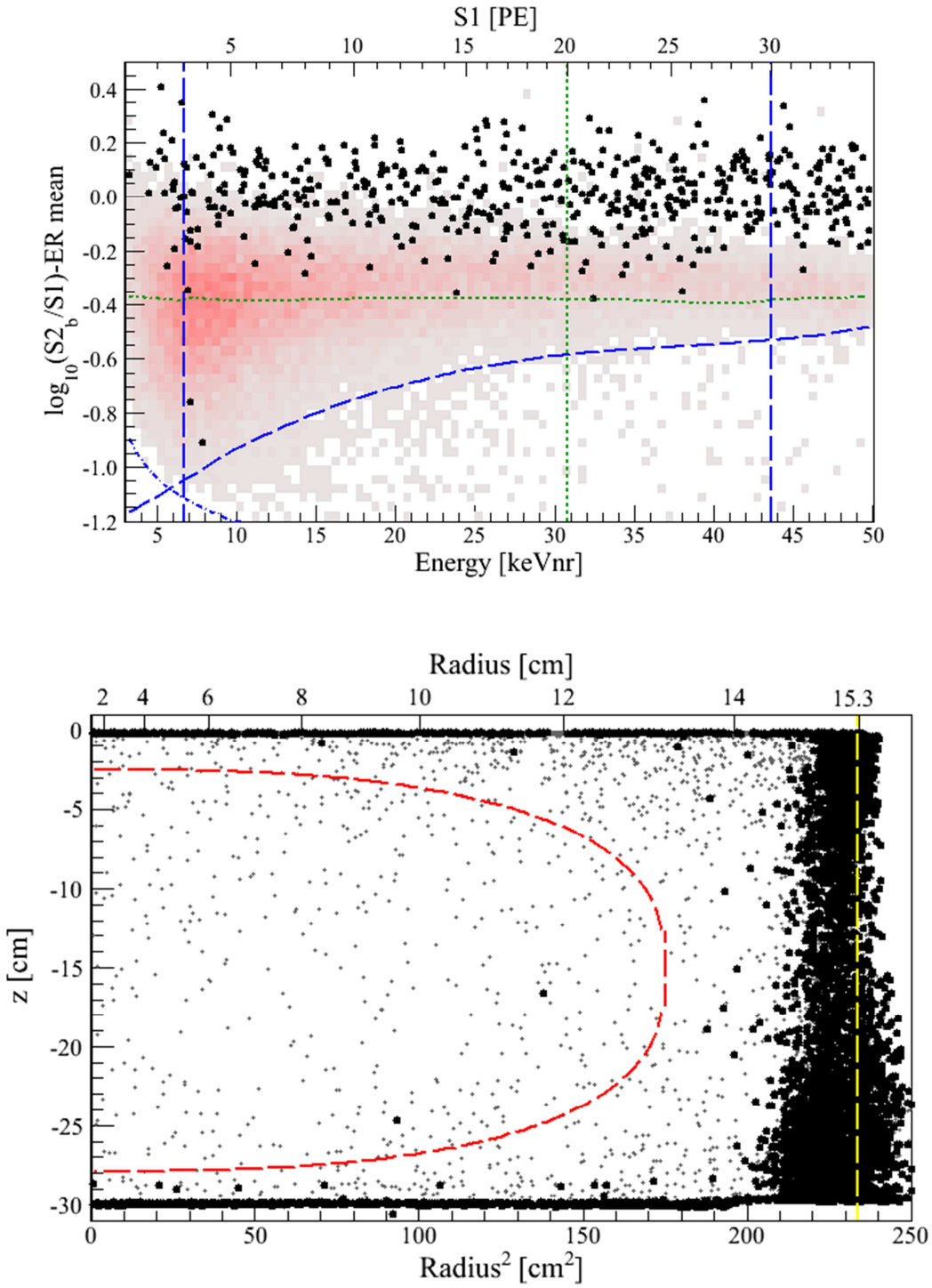

FIG. 5.20: up – discrimination parameter as a function of nuclear recoil equivalent energy; black dots indicate the ER band and gray dots indicate the NR distribution measured with AmBe neutron source; blue dashed line indicate the WIMP energy region defined and the green dotted line indicate the 99.75% rejection level; down – distribution of the events in the 34kg fiducial volume (red dashed line) [42]

In FIG. 5.20, the events distribution is presented. Two events fall in the WIMP search region after unblinding but there are no leakage events below 3pe. The Profile Likelihood analysis indicates that there is no excess due to dark matter signal and the probability that the expected background $(1.0 \pm 0.2\, events)$[19] in the region of interest fluctuates to 2 events is 26.4% leading to the conclusion of no dark matter signal.

The world's most stringent limit on the spin-independent elastic WIMP-nucleon scattering cross section has been set with a minimum value of $2 \times 10^{-45}\, cm^2$ for a WIMP mass of 55 $GeV/_{c^2}$ [19] (see figure 5.21).

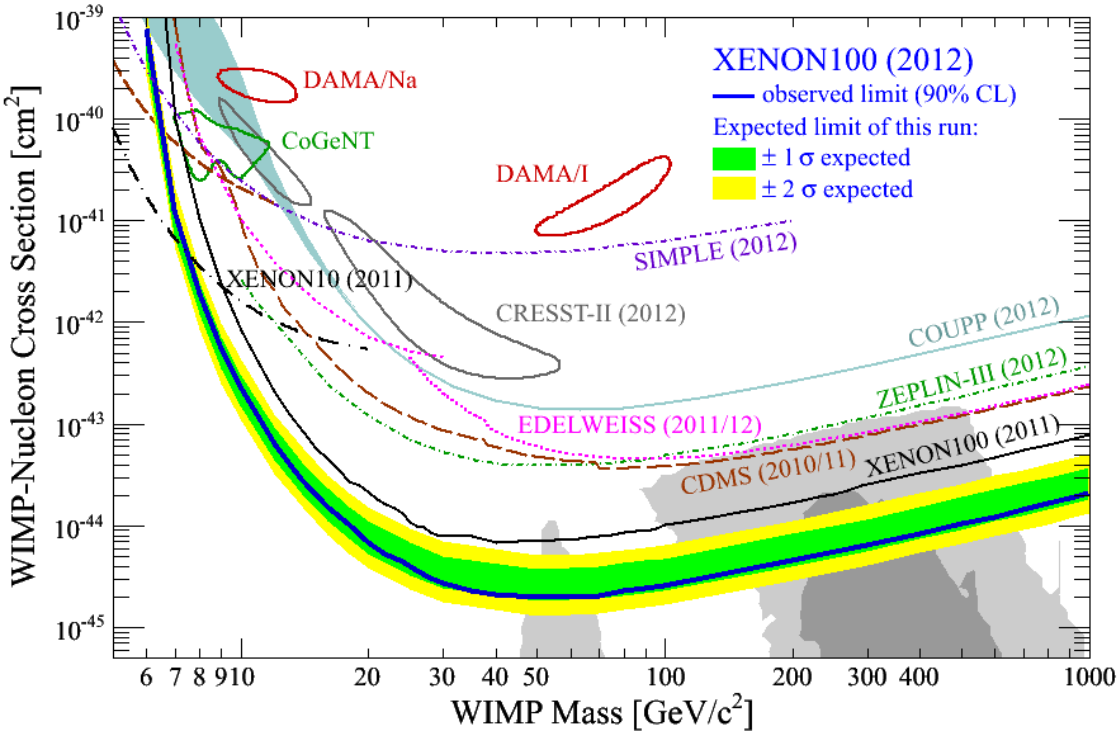

FIG. 5.21 – Spin-independent elastic WIMP-nucleon cross section (solid blue line) for 224.6 live days of XENON100 dark matter data; the green/yellow band indicates the 1 and 2 sigma expectancy of the curve [42]

5.3 Concluding remarks

The XENON100 Experiment, located in the Gran Sasso National Laboratory in Italy, looks for dark matter in the form of WIMPs by observing scintillation and ionization signals in xenon in a dual phase TPC. The nature of dark matter still remains an unanswered question in cosmology, but XENON100 has been the leading

experiment in direct dark matter detection since the first results and up to the last unblinding published results in 2012 [19].

In this chapter, details of the studies performed by me for the standard analysis of XENON100 experiment are presented. In section 5.1.2 the single scatter events study is outlined. The definition for the *XS2single*, the cut responsible for the selection of this type of events, has been improved and tested during 2 scientific runs (Run08 and Run10). The new energy dependent cut (cut on the second S_2 peak area with dependence on the first S_2 peak area), using also a lower threshold, showed a better efficiency when compared with the constant cut used for the previous runs (cut only in the area of the second S_2 peak). Better values of the cut acceptances for Run10 have been obtained, comparing with Run08, using both NR and ER calibration data and the new analysis cut. This cut is one of the most important since it is responsible for the selection of the events that might be WIMP candidates. The results obtained from the determination of the secondary scintillation gain studies ($\sim 19 pe/e^-$), using single scatter events, are in agreement with the values from the literature what further validates *XS2single.*

In the following section, 5.1.3, a concept characterizing the non-uniformity of the S_2 signals distribution (*hot spots*) has been defined and studied. The problem associated to the presence, in some situations, of an increased density of S_2 events in the acquired dark matter datasets was monitored, explained and corrected by defining proper cuts to reject the undesired events that occur spuriously during detector operation. The hot spots detected are due to the wider and lower amplitude S_2 signals, that appear earlier in the readout window, resulting in anomalous ratio of S_2 signals distributions of both top and bottom PMTs arrays. This problem has been corrected defining proper cuts in the top and bottom S_2 distribution spaces (using *S2Top* and *S2Bottom* parameters), studying the waveforms of these events and the PMTs responsible for the readout. These events could be safely discarded, since it was demonstrated that the S_2 events from the hot spots don't have a corresponding S_1.

The influence of the acceptances variation for the background modulation analysis has been also performed and the results have been reported in section 5.1.4. In this case all the cuts defined for the XENON100 experiment have been considered and the acceptances have been calculated using the ER data from the calibrations. The acceptances have been plot as a function of each ER dataset date for 2 energy ranges (3-14pe and 14-30pe). The corresponding χ^2 curves as a function of modulation amplitude have been plot and the sinusoidal variation for a period of 1 year has been extracted. The results from the 3σ and 5σ upper limits derivation (~3% and ~1.4% as best fit modulations for 3-14pe and 14-30pe energy ranges respectively) has shown that no strong influence of the acceptances variation in time exist and thus does not need to be taken into account for Profile Likelihood analysis.

Other small analysis tasks that were not presented here have also been performed during the regular shifts, locally at LNGS, since the data acquisition and calibrations required, in some situations, (after Xe recuperation and distillation procedures or after several different maintenance operations) special studies to be performed as the quality of the data can change if the liquid xenon level in the detector has changed, if there are noisy PMTs or if the applied voltages settings are changed.

The conclusions of the studies presented above, as part of the analysis group effort, helped to generate the XENON100 dark matter search results presented in the second part of the chapter, in section 5.2. The agreement with the results of the CDMS low energy analysis and with the new and better results achieved by the LUX experiment in February 2014 is evident (see FIG. 2.9 from section 2.2.3). However, they are not consistent with the interpretation of the DAMA/Libra and CoGeNT signals as WIMP interactions. The case of no ion channeling in DAMA/Libra is ruled out by both the S_2 only analysis and the $2pe$ threshold in the standard analysis with all considerations of Q_y and $\mathcal{L}_{\text{eff}}$. When ion channeling is allowed in DAMA/Libra, the regions consistent with a WIMP interaction are still excluded by the S_2 only analysis and the standard analysis with a $2pe$ threshold and the global fit with constant extrapolation for $\mathcal{L}_{\text{eff}}$. The results of this analysis also confirm that the signals in DAMA/Libra and CoGeNT are not due to WIMP interactions.

Since XENON100 is still taking data (Run14) plus the 150+ days from Run12, this analysis has great potential for establishing an increased sensitivity in the low mass WIMP region. For the XENON100 data set, which has significant exposure, the S_2 only analysis was used to probe the cross section for low mass WIMPs to much smaller values (see FIG. 5.19 and 5.21), providing both a potential for the discovery of a low mass WIMP and a consistency check for the standard analysis. The correct implementation of the trigger threshold allows for a more robust calculation of the sensitivity in the standard analysis. The un-blinding of Run12 and its realistically expected competitive scientific results are forthcoming.

CHAPTER 6

Electric field simulations for the XENON1T Experiment

Electrostatic simulations of the XENON1T dark matter detector were carried out and results of all the studies accomplished by me are presented in details in this chapter in section 6.3. Electrostatic simulations contribute to the optimization of the charge sensitive region by reducing areas of charge loss. These simulations also help determining problematic regions that would otherwise hinder detector calibration and data analysis.

6.1 XENON1T Experiment

Xenon1T Experiment is the next stage of the XENON collaboration, under construction phase in Hall B of the Gran Sasso underground laboratory in Italy (see figure 6.1 below).

For the construction of the future XENON1T detector many studies and tests have been done. This huge effort has been divided in several working groups (WG), each of them including several institutions of the collaboration that are responsible for the tasks as following: WG1 – Infrastructure; WG2 – Muon veto; WG3 – Water tank; WG4 – Detector TPC; WG5 – PMTs; WG6 – Cryostat; WG7 – Cryogenics; WG8 – RESTOX; WG9 – Slow Control; WG10 – Distillation Column; WG11 – Screening; WG12 – Purification; WG13 – Gas purity analysis; WG14 – Calibration; WG15 – Monte Carlo (MC); WG16 – Data acquisition (DAQ); WG17 – Computing.

Taking into account this consideration, only the details regarding the construction of the TPC will be presented since only these details have been used for the work presented in this chapter.

The LXe detector will be placed in a large water shield instrumented with PMTs using Cherenkov light as muon veto. With about 4 m of purified water in all directions the LXe target will be effectively shielded from gamma and neutron background associated with the environment and from cosmic ray induced neutrons. The cryogenics design of XENON1T is based on the experience gained by operating the XENON10 and XENON100 detectors underground in the Gran Sasso Laboratory. The larger xenon mass requires several design changes, but they are predictable and have been or are currently being tested.

FIG. 6.1 – General view of the Hall B and XENON1T prototype [67]

As the previous 2 detectors XENON10 and XENON100, XENON1T detector is a dual phase (liquid-gas) TPC and the WIMP detection is based on the same principle. Primary and secondary scintillation light is detected by the photosensors arrays at the top and the bottom. Ionization electrons produced by interactions in the liquid xenon are efficiently extracted from the liquid to the gas, with subsequent amplification via proportional scintillation. The simultaneous detection of primary scintillation (S1) and charge (via proportional scintillation light S2) provides a powerful tool for the discrimination of background events (electron recoils) from nuclear recoils (WIMPs interaction). The S2 hit pattern (X-Y) and the time difference between S1 and S2 (Z) provides a 3-D vertex reconstruction.

6.2 XENON1T detector construction requirements and tests

The Xenon1T detector (see figure 6.2a and 6.2b below) will be filled with very high purity xenon. All the materials used for the TPC production should be very pure

and do not provide high outgassing rate at liquid xenon temperature. Especially dangerous impurities are water, oxygen or any electronegative gases. TPC parts should be cleaned ultrasonically with pure alcohol and rinsed in deionized water before the TPC assembly inside the clean room. The grids should be stable to the process of ultrasonic cleaning and water rinse.

FIG. 6.2a – General outside view of the XENON1T TPC [68]

The XENON1T detector will be a very low background apparatus (a fraction of ~100 lower than background in the actual XENON100 detector). Extremely low radioactivity materials should be used (high purity copper, titanium or low radioactivity stainless steel). The amount of material used should be minimized, but to keep the mechanical properties required. Before using inside the XENON1T detector, the metals will be screened using the low background screening facility at Gran Sasso Laboratory.

FIG. 6.2b – General inside view of the XENON1T TPC [68]

Grids are used to provide uniform electrical field for the charge drift in liquid, extraction of the charges from liquid to the gas phase and for the production of the proportional scintillation light. In the case of the XENON1T detector we are using three grids on top and two grids on the bottom of TPC.

The grids will be placed in front of VUV sensitive PMTs. In order to have low threshold for the detected energy and good resolution, the number of scintillation photons should not be attenuated before hitting the photosensor. The grids should be optically transparent to the VUV scintillation light of xenon (178nm as a median wavelength). Since we are going to use several grids the optical transparency of the meshes become critical for the volume averaged scintillation light yield. The mesh optical transparency should be as high as possible (96-99 %).

Electrical field simulations for the Xenon1T TPC have been performed to ensure drift field uniformity and energy resolution for the proportional scintillation signal (S_2). The optimization of the E-field uniformity should be done in compromise with the optical transparency as maximizing optical transparency requires increasing the mesh pitch, while E-field uniformity requires the opposite.

6.3 Electrostatic field simulations

Electrostatic Simulations of the field profiles in the detector were carried out using COMSOL Multiphysics software, which uses finite element algorithms for 2D and 3D partial differential equations. The simulations were used to determine what potential settings and field values should be used to maximize the sensitive volume and minimize regions of charge loss within the detector.

6.3.1 Optimization of Charge Sensitive Region

The charge sensitive region of the detector is defined as the volume of liquid Xe inside of the Teflon shaping cylinder, a cylindrical volume with a diameter of 975mm and a height of 987mm from the cathode mesh to the liquid-gas interface. The presence of a uniform and properly shaped drift field in this region allows for charge to be drifted towards the interface. From here it is extracted to the anode mesh resulting in the secondary scintillation signal. This drift field is maintained by 74 regularly spaced copper shaping rings mounted outside of the inner Teflon cylinder. The shaping rings have their voltages applied through a chain of resistors. Computations of the filed profiles were made for an idealized $1kV/cm$ drift field.

The details of dimensions and voltages applied for each part of the TPC are listed in tables 6.1 and 6.2.

TABLE 6.1 – Default geometry details of the TPC used for COMSOL simulations

Geometry element	*dimensions/distances*
Cathode to liquid surface	987mm
Shaping ring diameter	975mm
Shaping ring width	5mm
Shaping ring height	10mm
Distance between shaping rings	3mm
Cathode and bottom mesh wire diameter	200µm
Cathode and bottom mesh pitch	5mm
Anode, gate and top guard mesh wire diameter	127 µm
Anode and gate mesh pitch	3.75mm
Top guard mesh pitch	7.5mm
Cathode to bottom mesh distance	70mm
Gate to anode distance	5mm

TABLE 6.2 – Default voltages values applied

Geometry element	*Voltages applied*
S2 threshold in gas phase	2.6kV/cm at 2atm
Anode	5kV
PMT, top and bottom guard meshes	-1.7kV
Cathode	-100kV
Gate and chamber wall	ground
ΔV between cathode and last shaping ring	2750V
ΔV between others shaping rings	1296.7V

Anode and two field closing grounded grids are used for the top mesh structure (see FIG. 6.3). The distance between lower grounded mesh and anode will be kept to 5mm, the same distance as it is in the actual XENON100 detector (see FIG. 4.5). The

anode voltage up to 5.0kV is expected to be applied to provide proper field for producing proportional scintillation for the extracted charge. The anode mesh should be parallel to the surface of the liquid-gas interface (2.5mm from the lower grid) with high accuracy. Any sagging or warping of the mesh creates deterioration in the proportional scintillation signal resolution.

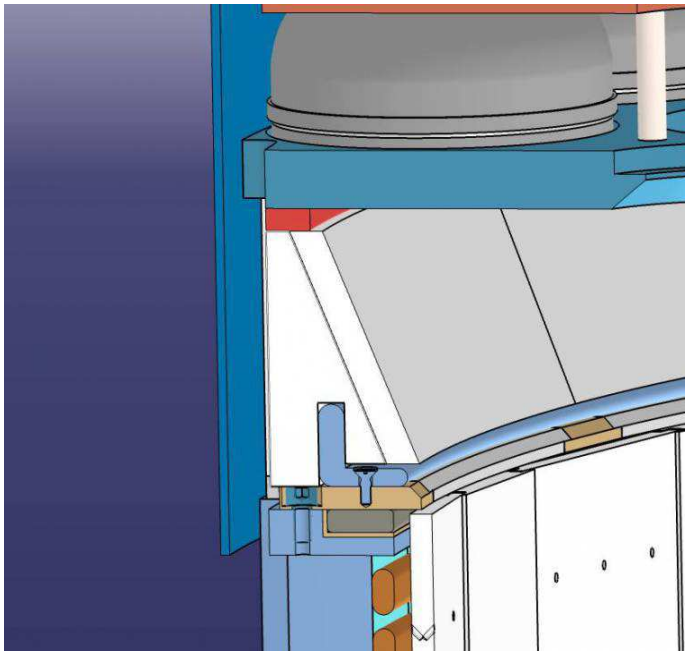

FIG. 6.3 – Details of the top XENONIT detector structure [68]

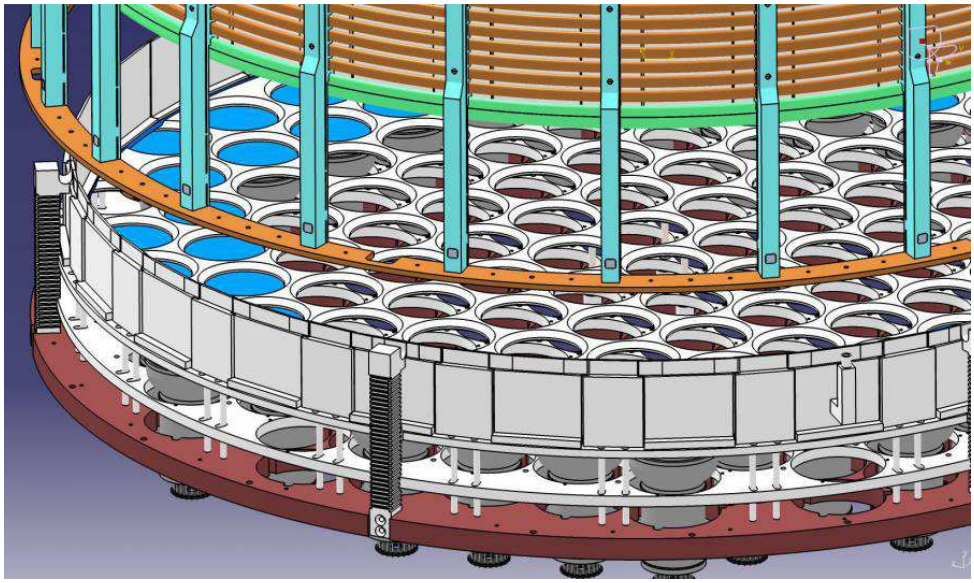

FIG. 6.4 – Details of the bottom XENONIT detector structure [68]

The cathode grid is situated in the liquid xenon, in the bottom part of the detector (see FIG. 6.4). The highest voltage (up to -100kV) will be applied to cathode electrode. The cathode mesh geometry is still under study. Several mechanical tests showed that this mesh can be easily made by linear thin wires instead of hexagonal cells preserving in this case a better transparency. Anyway, studies regarding the electric field uniformity in the drift region could not be compared directly for these 2 alternatives (linear wires vs. hexagonal cells). Since for a 2D diametrical section of the TPC, the intersection of the cut plane with the hexagonal mesh or single wires mesh corresponds to a distribution of linear circles, the 3D correspondence in COMSOL of the 2D circles distribution obtained is defined by a concentric wires mesh and to perform a 3D simulation for entire drift region is limited by the COMSOL software. The results related to this subject are presented in more details in the next section.

6.3.2 COMSOL simulations results

6.3.2.1 2D simulations for entire TPC geometry

The purpose of the simulations presented in this section is to determine how much of the sensitive volume is affected by non-uniformities of the electric field in the drift region.

After performing the COMSOL simulation of the electric field, the charge flow paths can be plotted in the geometry. This generation of liquid noble gas detectors requires delicate work to obtain the uniform drift field inside the TPC needed to collect charge signal from all the regions of the active target. In particular more difficult is to generate uniform field in the bottom corner of the detector, cathode region i.e., at large radii, because of strong potential gradient due to the presence of the high voltage of the cathode and the other grounded components of the detector. It is necessary to avoid dielectric breakdown and field emission in the detector materials.

In this section we present the behavior of the streamlines and their dependence on the TPC height and radius, adding the plots of the field displacement, the electric field normal along the radial direction and the electric field normal as a function of the TPC height. Following the design of the detector presented above, the best result of the 2D simulation obtained is presented in FIG. 6.5. These simulations are very important for the final design of the XENON1T TPC since the charge loss and charge displacement (see figures below) can be minimized by optimizing the field cage.

Teflon is an insulator. So charge that follows a field line that penetrates into the Teflon will be deposited onto the Teflon resulting in a reduction or loss of charge signal. In addition to charge loss there is also the issue of charge displacement. Fields at larger radii and closer to the shaping rings will have a radial component in addition to the Z component for upward drift. For this category the position at which the charge reaches the liquid/gas interface will be displaced with respect to the position where the

event occurred in the liquid. This would result in improper reconstruction of the event position.

The charge displacement region occurs inside the sensitive region of the detector. This effect is due to the resultant electric fields at the fringes of the sensitive volume having an outward direction (see figure 6.6 and 6.7).

In the ideal case the radial component of the electric field is expected to be zero, so each streamline should be perfectly vertical. However, due to the field distortions in the cathode region, the more external streamlines bend toward the Teflon wall. Figure 6.8 shows that the effects of charge displacement decreased with the radius (i.e., moving away from the center of the detector).

The 2D simulations have been used also to check how much the uniformity of the electric field is changing by modifying the pitch of the grids meshes (anode, gate, cathode, top and bottom protection meshes).

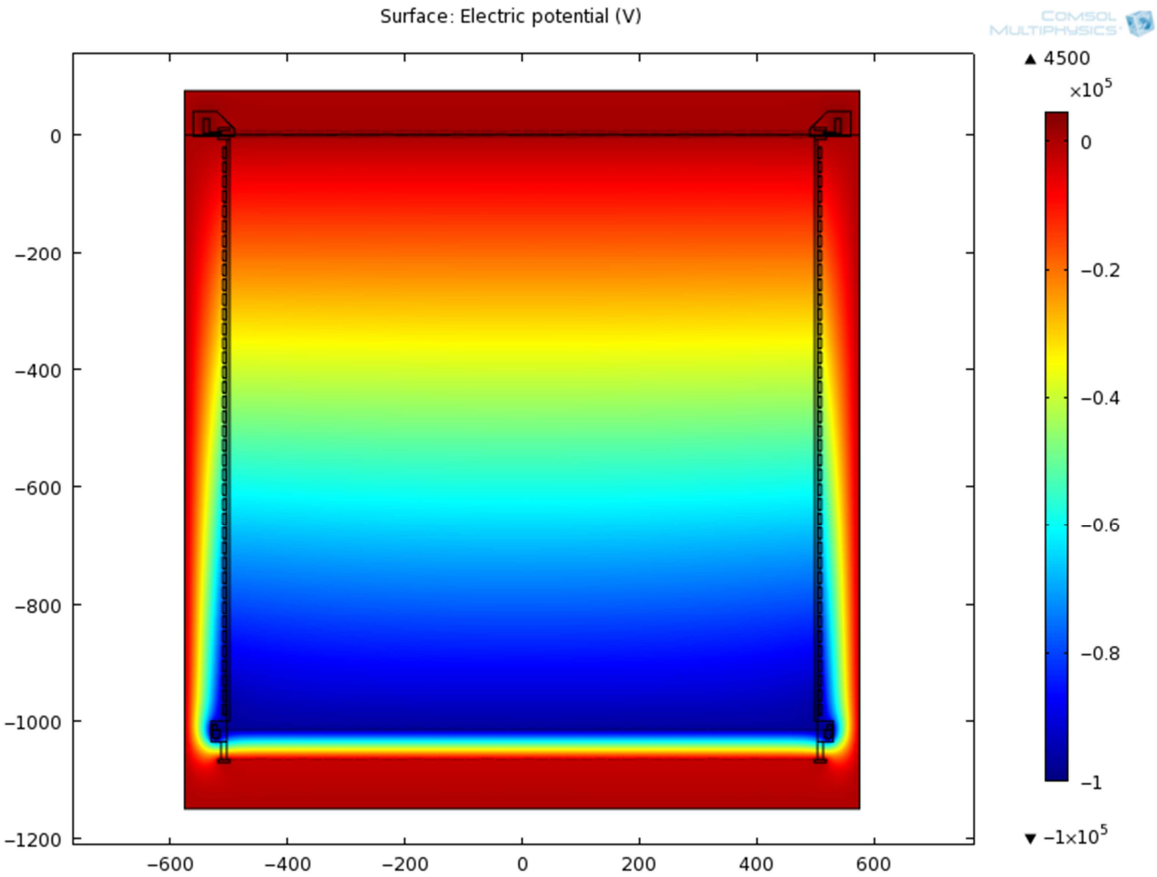

FIG. 6.5 – General view of the electric potential distribution in the TPC detector; X-Y units are expressed in mm and the colored scale in the right represents the voltages applied expressed in Volts (V)

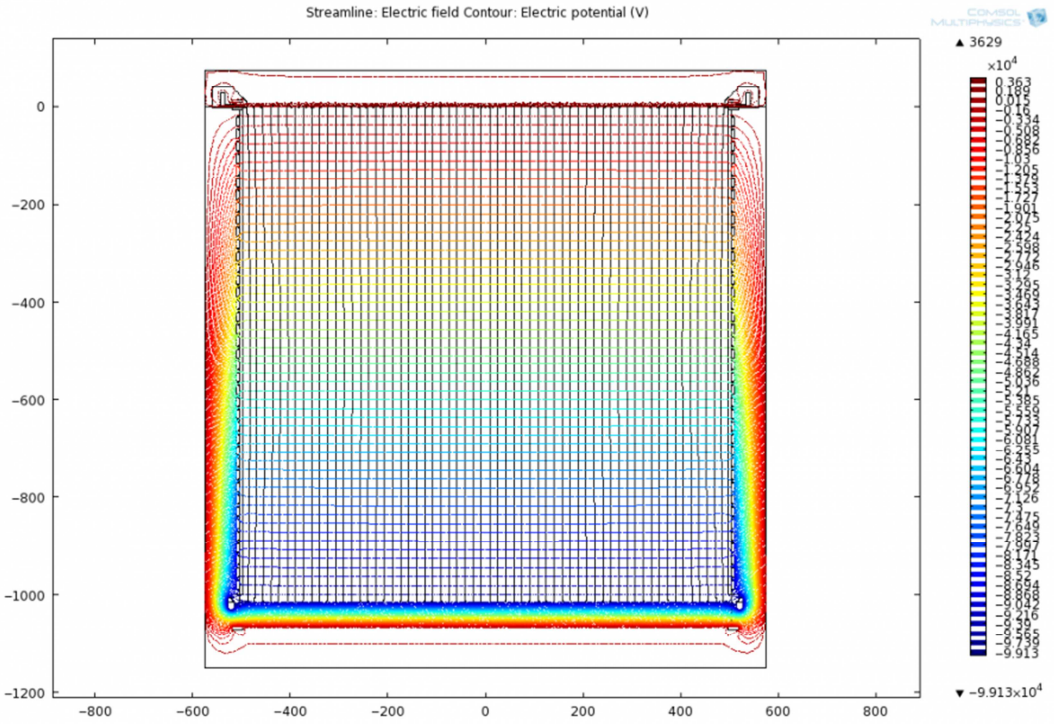

FIG. 6.6 – General view of the electric field streamlines (represented by the vertical black lines) inside the TPC; X-Y units are expressed in mm and the colored scale in the right represents the voltages applied expressed in Volts (V)

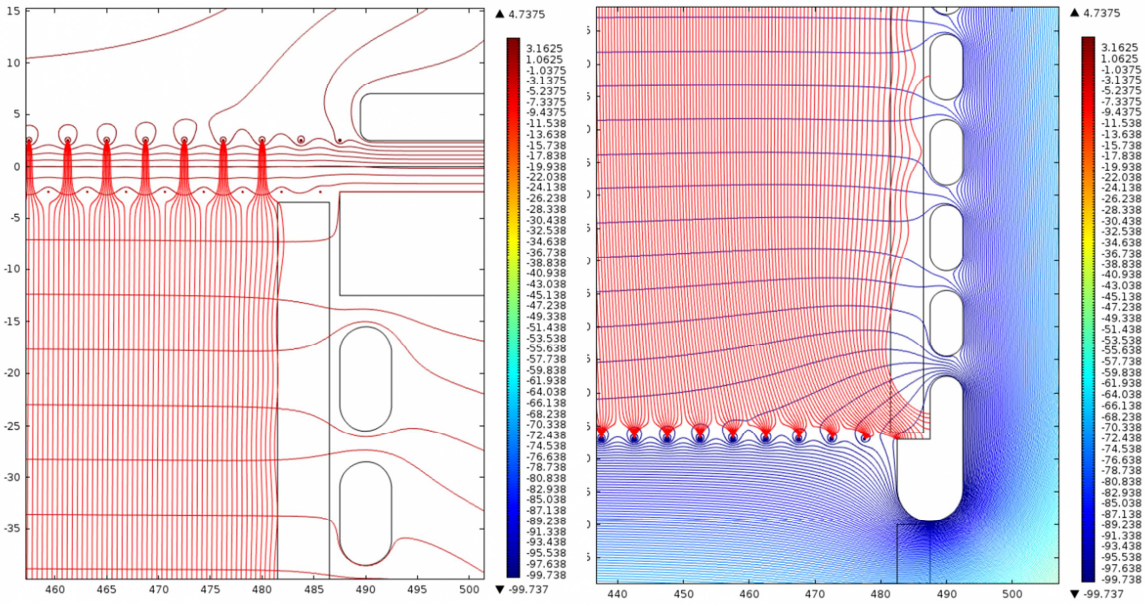

FIG. 6.7 – Detail of streamlines plot (red lines) at large radii on the anode region (left) and on cathode region (right); X-Y units are expressed in mm and the colored scale in the right represents the voltages applied expressed in Volts (V)

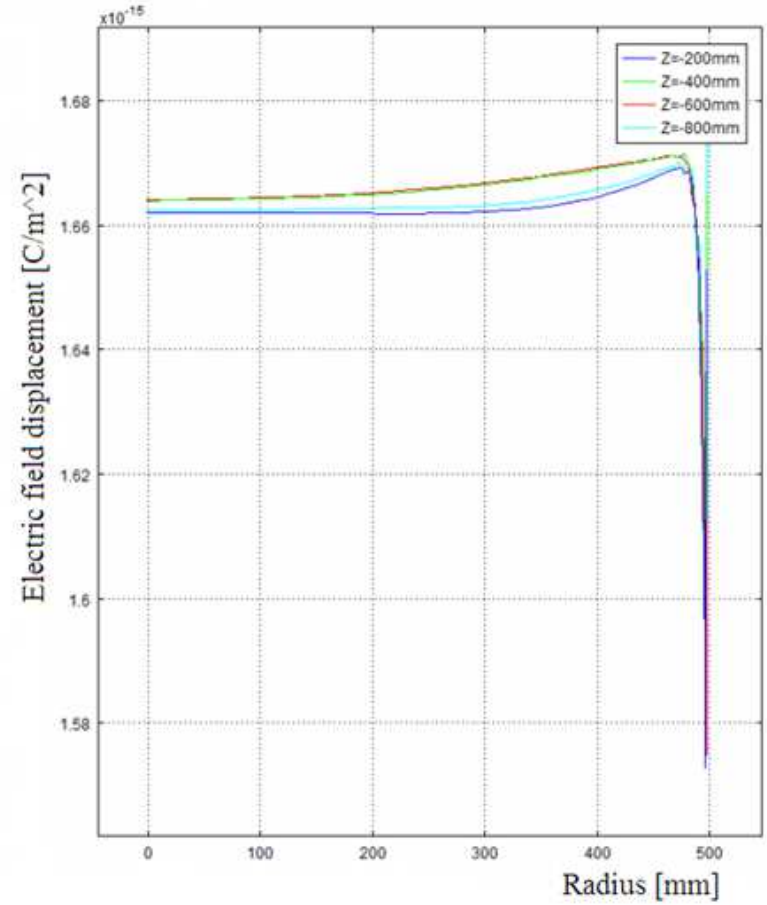

FIG. 6.8 – Electric field lines displacement as a function of radius; the various lines shown in the figure correspond to different cuts in the height of the detector: Z = -200 mm (blue), Z = -400 mm (green), Z = -600 mm (red) and Z = -800 mm (cyan); the electric field displacement is decreasing with the radius

For the anode and gate meshes the electric field uniformity for another 3 transparencies has been studied, i.e. by modifying the pitch of the hexagonal mesh from 3.63mm for the default model to 5, 7 and 10mm for models 1, 2 and 3 respectively. In figure 6.9a we plot the electric field normal as a function of radius, for a specific height, using a cut line at Z=1mm, indicating the region 1.5mm below the anode. From the results presented in figure 6.9a we can conclude that the anode/gate mesh opening cannot be increased more than 5mm in order to have good electric field uniformity in the anode region.

Additional studies show that the increase of the anode/gate mesh pitch does not affect the uniformity in the top protection mesh region, but the decreasing trend of the averaged electric field with transparency increases is still observed. The averaged electric field is decreasing with $\sim 40 V/cm$ for each 1mm of mesh pitch increase (see FIG. 6.9b).

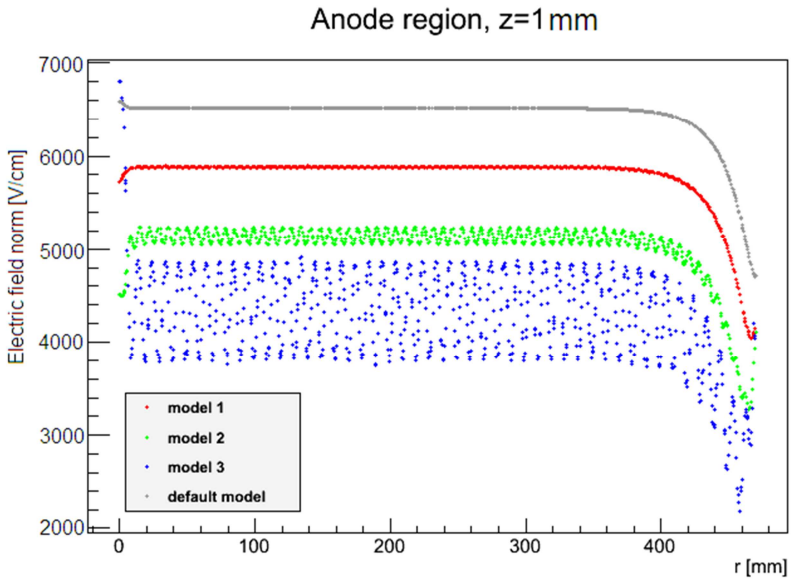

FIG. 6.9a – Comparison of the electric field uniformity and displacement as a function of radius for different four anode/gate meshes transparencies in the anode region; default model (gray dots) indicates the best result taking into account uniformity of electric field that requires pitch as small as possible and the scintillation light yield that requires the opposite; models 1, 2 and 3 (red, green and blue dots respectively) show explicitly the increase of displacement and non-uniformity of the electric field with mesh transparency; a decreasing trend of averaged electric field with mesh transparency increases (~400V/cm for each 1mm of mesh pitch increase) is also visible

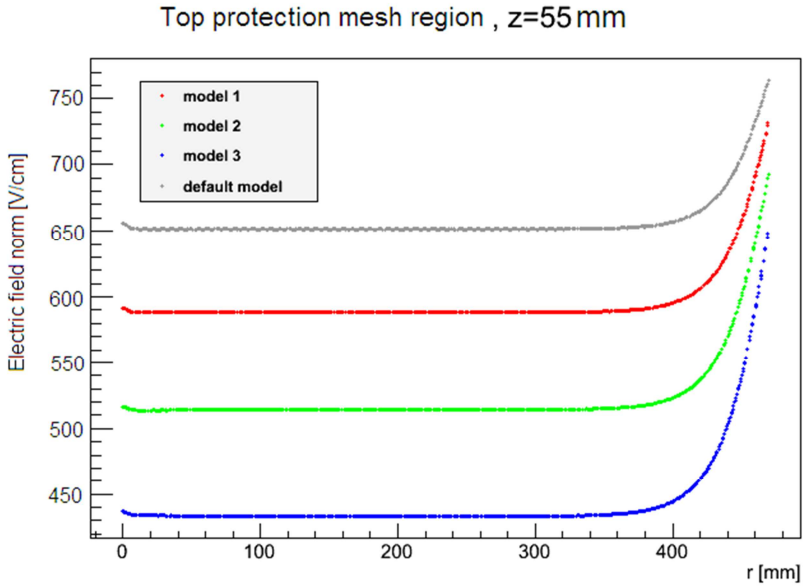

FIG. 6.9b – Comparison of the electric field uniformity and displacement as a function of radius for different four anode/gate meshes transparencies in the top protection region; default model as well as models 1, 2 and 3 (gray, red, green and blue dots respectively) show explicitly the increase of non-uniformity at large radii and decrease of averaged electric field with increases of mesh transparency

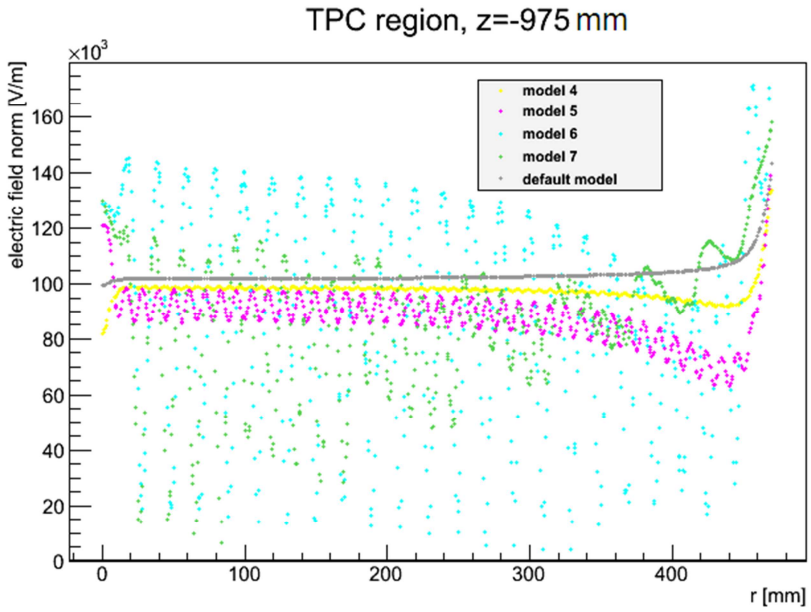

FIG. 6.10 – Comparison of the electric field uniformity as a function of radius for different five cathode meshes transparencies; the default model (gray dots) and model 4 (yellow dots) indicate the best result; the electric field for the models with cathode mesh pitch larger than 7.5mm looks like a disorder inside the TPC with big variations of the electric field (models 5, 6 and 7 corresponding to magenta, cyan and green dots respectively)

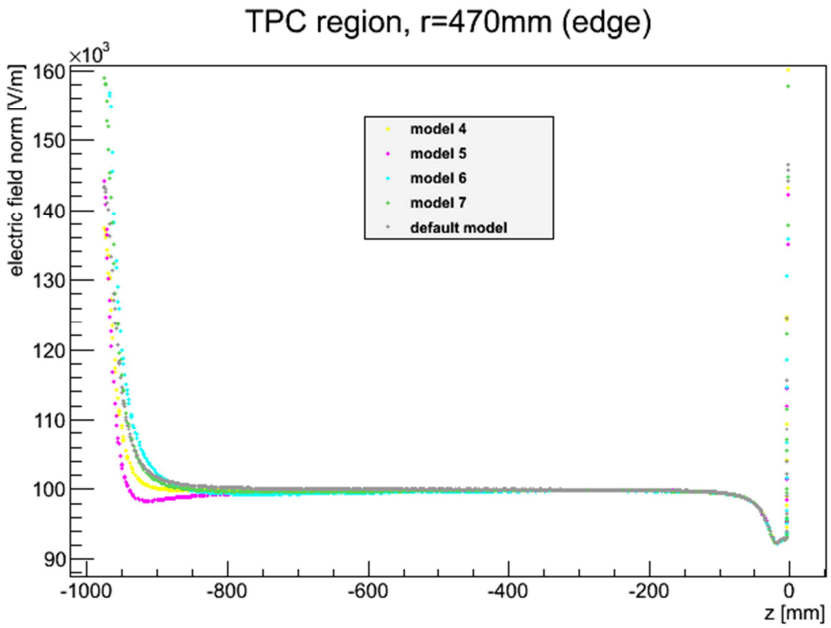

FIG. 6.11a – Comparison of the electric field displacement as a function of TPC height (Z) at large radii (edge) for different five cathode meshes transparencies represented as following: gray dots – default model, yellow dots – model 4, magenta dots – model 5, cyan dots – model 6 and green dots – model 7

The study aiming to increase the transparency of cathode mesh is presented for different 5 cases. The pitch was modified from the default model with pitch of 5.52mm to 7.5mm (model 4), 11mm (model 5), 20mm (model 6) and using higher density of wires at large radii and lower density of wires in the center of the detector, i.e. the pitch varying from 5 to 19mm (model 7). The plots of electric field as a function of radius for all the cases, figure 6.10, are related to the region 10mm above the cathode mesh, defined by a cut line at Z=-975mm.

Taking into consideration the results presented in figure 6.10, the cathode mesh pitch cannot be increased more than 7.5mm in order to keep an uniform electric field without big displacements of electric field radial component.

A variation of the electric field from $1.45kV/cm$ to $1kV/cm$ can be observed close to the Teflon walls and near the cathode frame in both radius and TPC height directions for ~10cm going to the center/top respectively, (see figures 6.10 and 6.11a respectively) for all the 5 models.

Another variation from $0.5kV/cm$ to $1.0kV/cm$ is present in the center of the TPC if going to TPC height direction but only for the models with very large mesh pitch (models 5, 6 and 7). The models that are using pitch from 5 to 7.5 mm are not affected (see figure 6.11b).

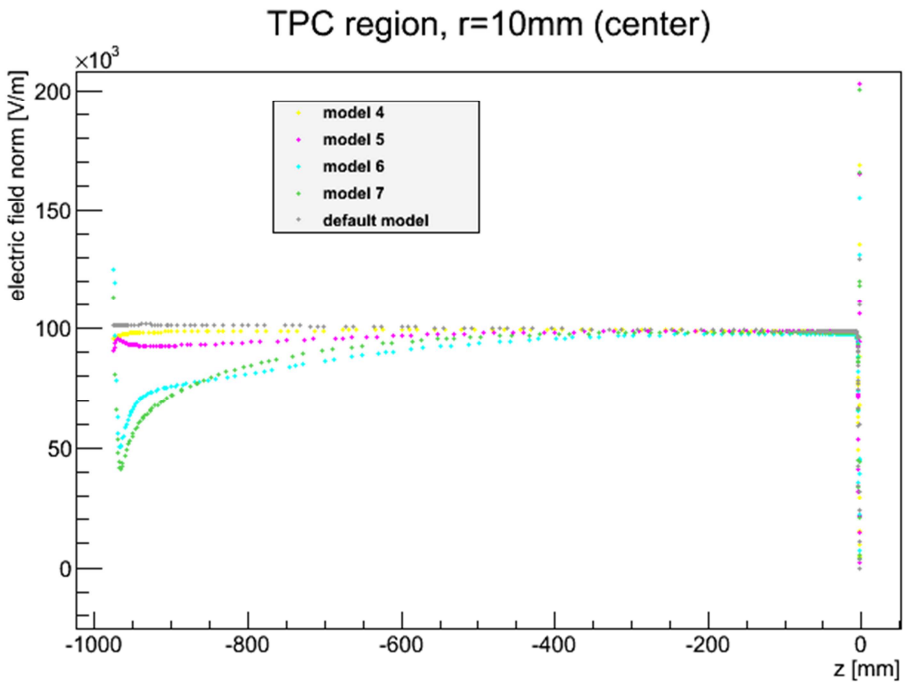

FIG. 6.11b – Comparison of the electric field displacement as a function of TPC height (Z) in the center of the detector for different five cathode meshes transparencies represented as following: gray dots – default model, yellow dots – model 4, magenta dots – model 5, cyan dots – model 6 and green dots – model 7

The electric field radial displacements and its dependence on the TPC height and radius have been studied analyzing the streamlines obtained as an output of the COMSOL simulation software. The streamlines behavior and the electric field normal along the radial direction have been compared for 5 models of the cathode mesh and 4 models of the anode/gate mesh in order to define a proper design of the electrodes.

The cathode region is quite delicate. These results show that a small field distortion similar to that one existent at the cathode region of actual XENON100 detector will be still present in XENON1T detector using the default geometry aforementioned. For example, the field distortion observed close to the XENON100 cathode led to the necessity of a software correction of the measured signals.

6.3.2.2 3D simulations and 3D/2D field simulation comparison

3D simulations could not be performed for the entire geometry of the detector because of COMSOL software limits and CPUs memory. Systematic attempts lead to the conclusion that only small volumes can be simulated in details.

In this study we have tried to see how much we can extend the 3D simulated diameter of the TPC using also small hexagonal cells for the meshes made of very thin wires ($127\mu m$). Therefore the anode region with 3 meshes (anode and gate mesh pitch 3.75mm and top protection mesh pitch 7.5mm) and the cathode region with 2 meshes (cathode mesh pitch 5mm and bottom protection mesh 7.5mm) were simulated separately.

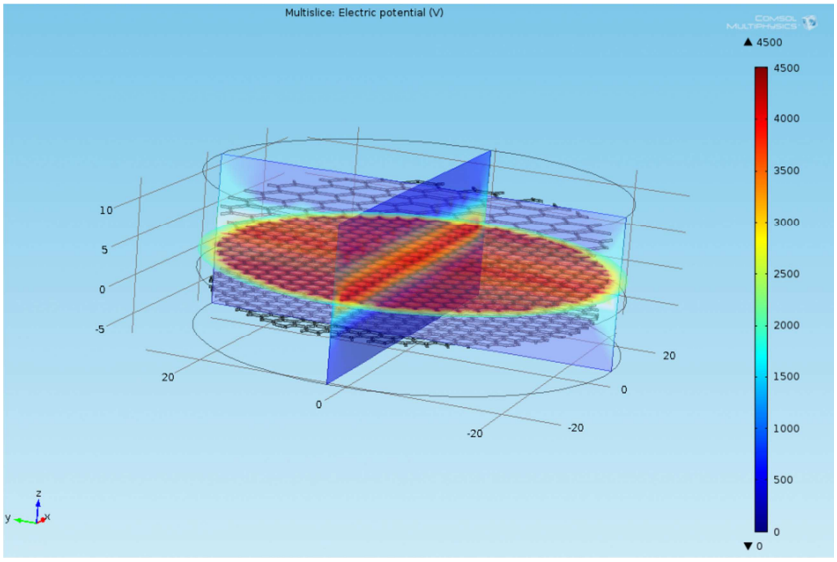

FIG. 6.12 – 3D simulation view of the anode region; on top the grounded protection mesh, in the middle the anode mesh at 5kV and below anode the grounded gate mesh can be observed; X-Y-Z units are expressed in mm and the colored scale in the right represents the voltages applied expressed in Volts (V)

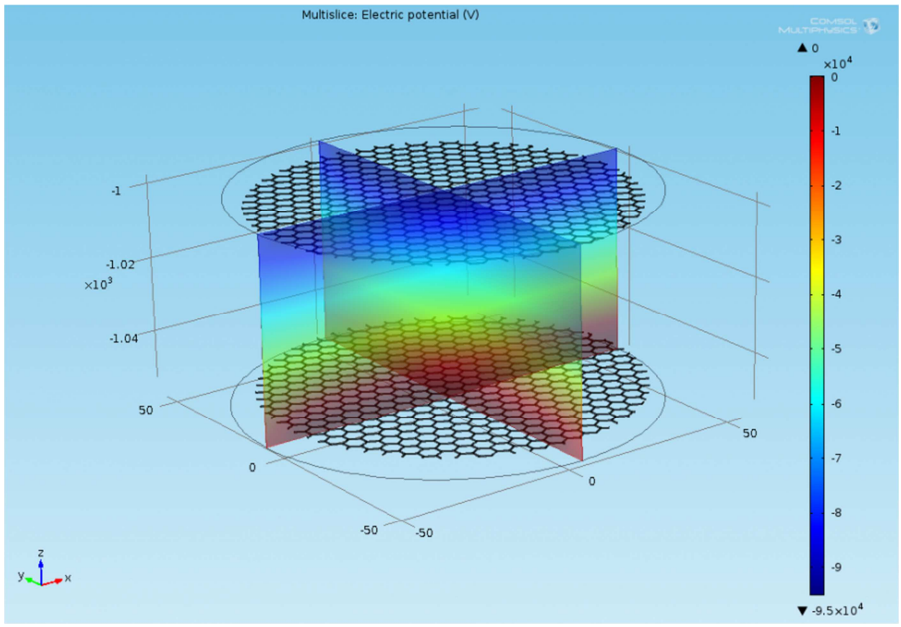

FIG. 6.13 – 3D simulation view of the cathode region; on top the cathode mesh at -100kV and below cathode the grounded bottom protection mesh can be observed; X-Y-Z units are expressed in mm and the colored scale in the right represents the voltages applied expressed in Volts (V)

As can be seen, the results in figures 6.12 and 6.13, only 50mm diameter of the TPC for the anode region and 100mm diameter of the TPC for the cathode region respectively, showed a correct field map and no error in the compilation process. Additional 3D simulations resulted that the diameter could be increased more to a maximum of 30cm but only in the case of using single wires mesh.

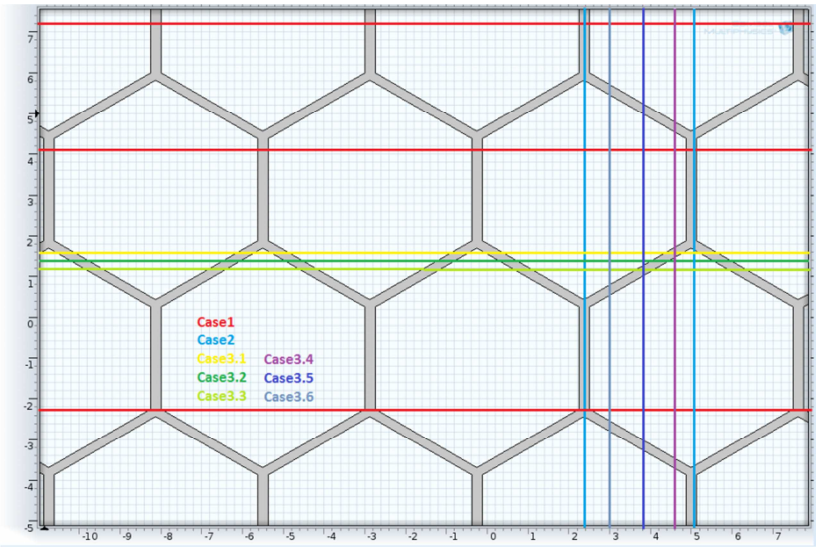

FIG. 6.14a – 2D view of the hexagonal mesh indicating the cut lines defining the cases under study

Anyway, even if only small volumes could be simulated, the 3D simulations results helped to see if there are major differences between 2D and 3D simulations and how to optimize the 2D conditions according to the 3D results. To make a comparison between 2D and 3D electric field profiles we used 7 different plane cuts to describe the possibilities to represent in 2D the 3D cathode hexagonal grid as it is shown in the figures 6.14a and 6.14b. The 2D electric field simulations have been performed for all 7 cases separately.

In case1 we consider a XZ cut plane in the 3D model, so the grid for most of different Y values will be represented in 2D as an array of circles 5 mm separated (red line). In case2 we consider an YZ cut plane in the 3D detector, so the grid for several X values will be represented in 2D as an array of rectangles 2.5mm width and 5.5mm pitch (cyan line).

The most complex case, case3, is describing all the remaining situations if we consider an XZ or YZ cut plane in the 3D detector. Now the 2D section is described by consecutive ellipsis but for simplification we are using circles too. Now the separation between 2 circles represented in 2D can vary from 0 to 2.5mm and pitch between each 2 consecutive circles vary from 5 to 2.5mm in case of a XZ cut plane and from 2.5 to 4 mm and 5.5 to 4mm in case of a YZ cut plane, respectively.

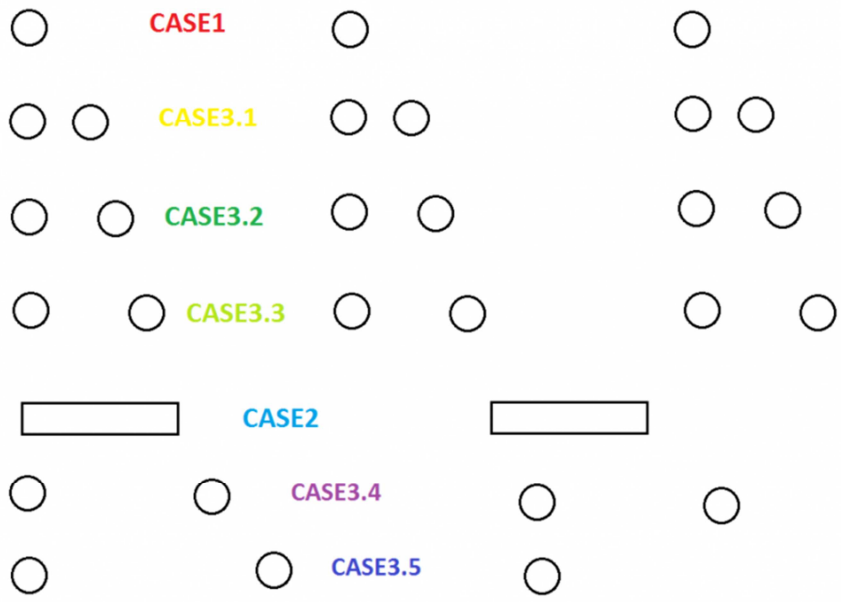

FIG. 6.14b – Scheme of the cases defined by the cut lines on the hexagonal mesh

3 cases have been studied if we are doing a XZ cut plane: distance between 2 circles is 1 mm and pitch between each 2 consecutive circles is 4 mm (case3.1); distance between 2 circles is 1.5 mm and pitch between each 2 consecutive circles is 3.5 mm (case3.2); distance between 2 circles is 2 mm and pitch between each 2 consecutive

circles is 3 mm (case3.3). Another 2 cases have been studied if we are doing a YZ cut plane: distance between 2 circles is 3 mm and pitch between each 2 consecutive circles is 5 mm (case3.4); distance between 2 circles is 4 mm and pitch between each 2 consecutive circles is 4 mm (case3.5).

For a better comparison of the discrepancies between simulations of each case in 2D and 3D respectively, the electric field displacement has been plot as a function of detector radius using a cutline in the region of the end of first bottom shaping ring, near cathode.

Only the 2D simulations show different results based on the plane through the TPC, which is studied if going from the edge to the center of the detector, instead of the 3D simulation where all the cases show almost equal behavior. This aspect is correct since in a 3D simulation the field distribution does not depend on different transparency of the mesh as in the situation of the different 2D cases (see FIG. 6.15a and 6.15b). However, the differences are probably related also to the point that the 3D correspondence of a 2D mesh is defined as concentric wires and not as hexagonal mesh.

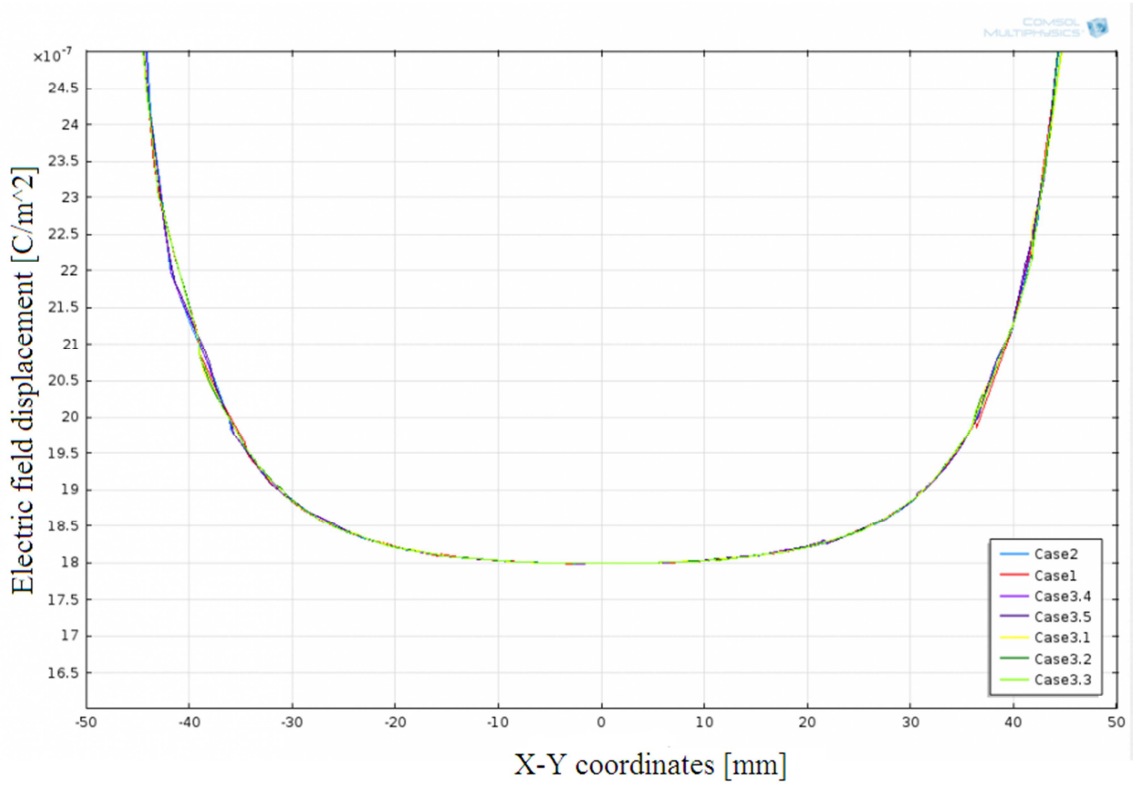

FIG. 6.15a – Electric field displacements as a function of X-Y coordinates, extracted from the 3D simulation using the plane cuts; only tiny differences can be observed

The cases 2, 3.1, 3.2, and 3.3 show the better imitation of the 3D results. If we consider such a large volume as XENON1T, the 2D simulations can optimize the electric field profile in the drift region of the detector but to be in very good agreement

with a 3D simulation it is better to implement in 2D geometry the average 3D transparency of each mesh under study.

Anyway the 3D simulations are most important and beneficial in the case of optimizing the gain and the resolution of the proportional scintillation light and the results of the study are presented in the next section.

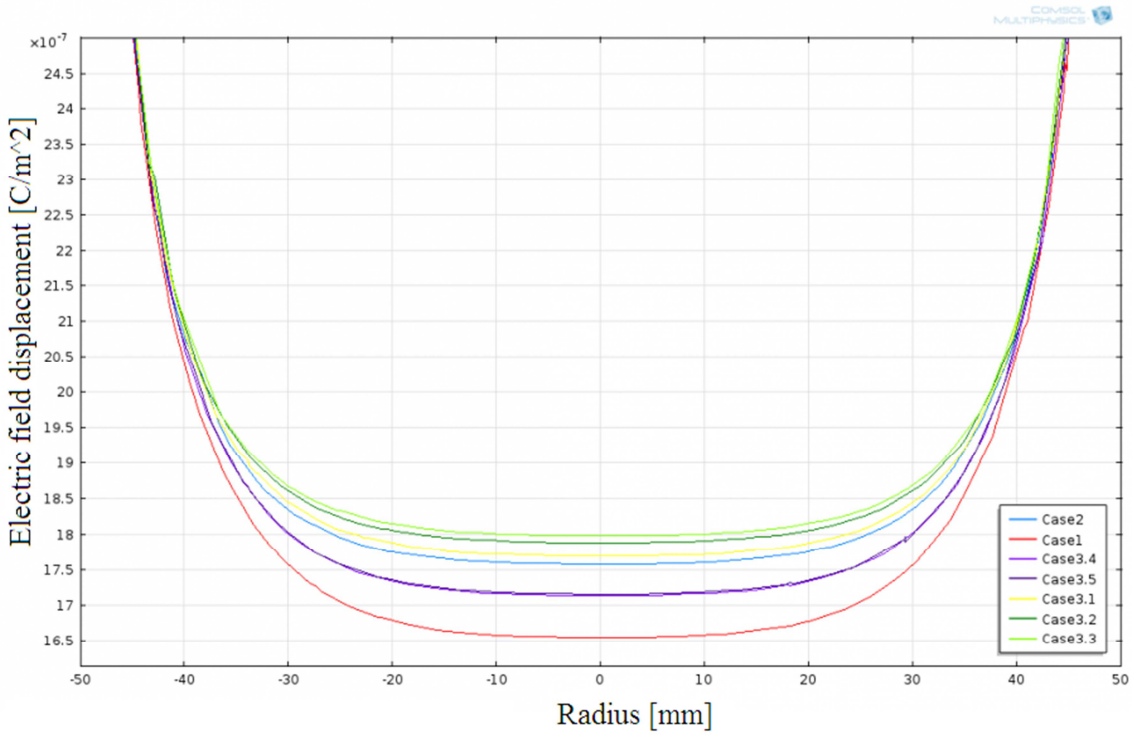

FIG. 6.15b – Electric field displacement as a function of radius, extracted from 2D individual simulation of each 2D case obtained from the plane sections in the 3D model

6.3.2.3 Optimization of single electron gain and resolution

In this section we will refer only to the upper part of the XENON1T detector (see figure 6.16 below) and focus the analysis on the proportional scintillation light S_2 that occurs in the gas phase. Taking into consideration the 3D simulations done for a small volume of the top part of the detector (see figure 6.12 above) including small diameters of the anode, gate and top protection meshes, in figure 6.17 we can see in detail the streamlines representing the charge flow paths only for one hexagonal cell of the gate mesh.

The principle of proportional scintillation light production is described in sections 3.2.2.2 and 5.1.2.3. The number of the UV photons produced in this process depends on the gas pressure P_g, the electric field E_g and the electron drift distance d_g in the gas, following the equation 5.5 that can be written as a function of amplification

factor $\alpha = 70\, photons/kV$ [69] and threshold for the reduced field for proportional light production $\beta = 1.0\, kV/cm/bar$ [69] resulting formula 6.1.

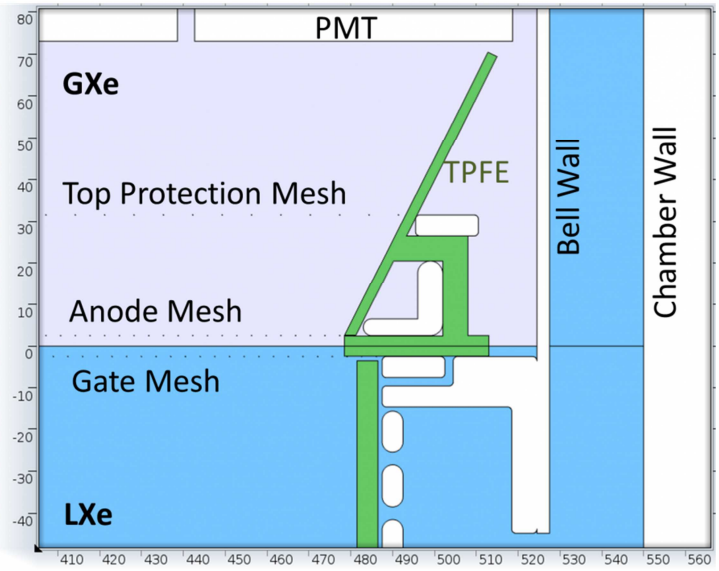

FIG. 6.16 – Scheme of the top/anode part of the detector; X-Y units are expressed in mm

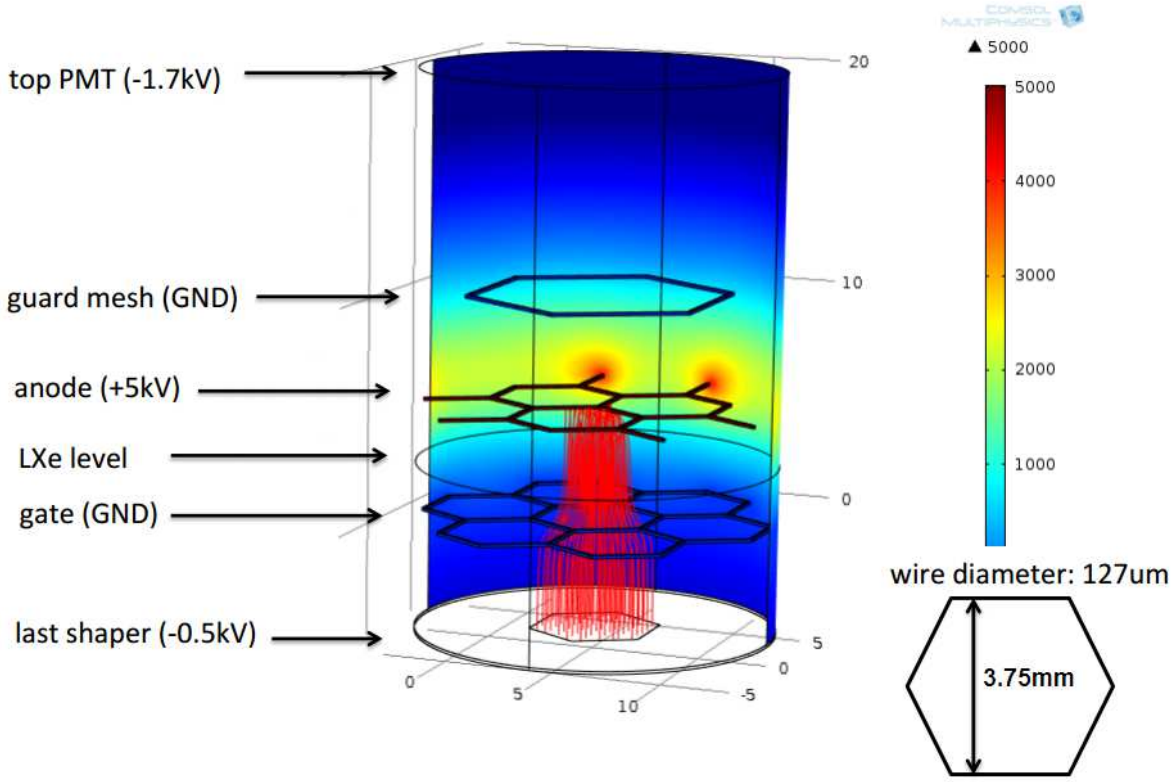

FIG. 6.17 – Streamlines for one hexagonal cell in 3D; the middle electrode is the anode mesh at 5kV and below the grounded gate mesh can be observed; X-Y-Z units are expressed in mm; the colored scale in the right represents the voltages applied expressed in Volts (V)

$$N_\gamma = \alpha N \left(\frac{E_g}{P_g} - \beta \right) P_g d_g \qquad (6.1)$$

In the formula 6.1, N is the the number of the electrons extracted from the liquid to the gas phase and N_γ is the S_2 photons yield i.e., the number of the proportional scintillation photons produced.

In figure 6.18 one can see the results for our case. The wire diameter considered is $127\mu m$, the anode/gate mesh pitch is $3.75mm$ (XENON1T default model), the drift distance in the gas phase is $0.25cm$ and the pressure is $2.26\ bar$. Using the results of the S_2 peak Gaussian fit from figure 6.18, a secondary scintillation gain value of $319.9 \pm 0.1\ photons/$é and peak resolution of $1.19 \pm 0.03\%$ are obtained.

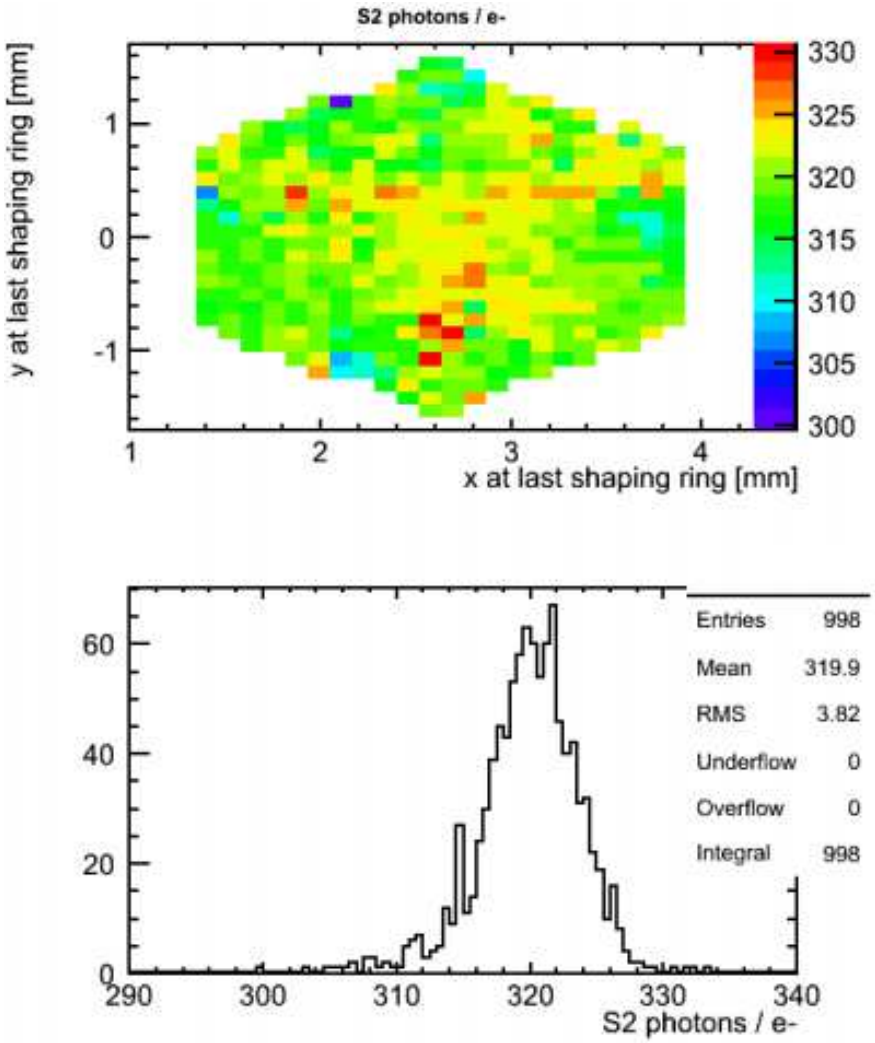

FIG. 6.18 – Top: S_2 photons distribution in the one specific hexagonal cell corresponding to the last shaping ring; Bottom: The S_2 peak related to the S_2 distribution

Following the procedure aforementioned, single electron gain and resolution from electric field simulations have been determined and compared [70] for several modifications of anode/gate mesh pitch and distances. The results are resumed in TABLE 6.3.

TABLE 6.3 – Results of single electron gain [photons/e] and S_2 peak resolution obtained from XENON1T electric field simulations

Anode/ Gate distance	*Anode/Gate hexagonal mesh pitch*							
	2.5 mm		*3.75 mm*		*5 mm*		*7.5 mm*	
	Gain [ph/e]	*Resolution [%]*	*Gain [ph/e]*	*Resolution [%]*	*Gain [ph/e]*	*Resolution [%]*	*Gain [ph/e]*	*Resolution [%]*
5 mm	319	1.2	320	1.19	322	2.1	324	2.9
10 mm	622	2.2	627	2	631	1.9	642	2.1

Several conclusions can be drawn considering the results presented in table above:

- the impact on the S_2 resolution due to the drift path is very small (less than 3%);

- the S_2 resolution becomes worse with the increasing of mesh cell pitch in the case of 5mm anode/gate distance but remains quite stable for 10mm anode/gate distance;

- the S_2 yield increases for larger anode/gate cell pitch for both anode/gate distances studied.

6.4 Concluding remarks

The studies presented in chapter 6 of this thesis presented research for the development of the future XENON1T dark matter detector. COMSOL simulations of the electric field inside the TPC have been performed. These simulations were important to assess the proper dimensions and the light collection, as well as to calculate the single electron gain and resolution of the proportional scintillation light that occurred in the gas gap.

First studies focused on the optimization of the field cage. 2D simulations for different geometries of the electrodes and shaping rings as well as several studies to assess the proper voltages settings have been performed. The best result obtained, i.e. uniform electric field, has been presented in section 6.3.2.1 and the resulting final geometry and voltages defined the *default model* (see section 6.3.1).

Since the transparencies of the meshes are critical for the efficiency of the scintillation readout, the study continued by simulating in 2D several modifications of the anode/gate and cathode meshes pitch, defining another 3 models for the anode/gate mesh and 4 models for the cathode mesh. The plots of the electric field as a function of radius, for different cut lines in the anode and cathode regions respectively, as well as plots of the electric field as a function of the detector height in the center of the detector and at large radii (edge) have been extracted from the simulations. Comparing all the results, a limit of 5mm pitch for anode/gate mesh and 7.5mm pitch for cathode mesh could be set, in order to maintain a good uniformity and small variations of the electric field (see section 6.3.2.1).

3D simulations could be performed only for small volumes, using 2 or 3 hexagonal meshes. A comparison of 3D/2D simulations has been done and it was outlined in section 6.3.2.2. The plot of the electric field displacement as a function of radius for different cut planes in the 3D simulated model have been compared with the cases defined by the cut planes, but simulated separately in 2D. Some differences could be observed for the 2D studies, due to the different 3D:2D correspondences of the mesh transparency for each case defined by the cut planes in the 3D model.

In the last section, 6.3.2.3, the S_2 gain and the peak resolution have been calculated for the default model using the 3D simulations results from the anode region for a small volume and a few hexagonal cells. The comparison of these results with those obtained by changing the mesh pitch or anode/gate distance, confirmed that the default model (3.75mm and 5mm for anode/gate and cathode meshes, respectively, and 5mm anode/gate distance) is the best alternative that will be taken into account for the TPC construction.

CHAPTER 7

Final conclusions and future work

This thesis addresses the question of the nature of dark matter in the Universe and presented a contribution for the optimization of the scintillation detection in the present and near-future double-phase Xe detectors within the XENON program.

The activities performed for the current XENON100 experiment, which has replaced XENON10, the first prototype, in the same shield and location at LNGS, as well as studies for the optimization of the TPC for the next phase of XENON program, a detector at the ton scale, XENON1T, have been presented in detail.

During the regular shifts, locally at LNGS, the experimental work included several duties to be accomplished, such as monitoring the cryogenic parameters of XENON100 detector, data acquisition and processing, calibrations and procedures for Xe distillation to remove ^{85}Kr. The details of all these techniques have been presented in Chapter 4. The data analysis tasks performed and the methods used for the single scatter event selection criteria, *XS2single* cut acceptances evaluation, *hot spots* monitoring and influence of the cut acceptances variation in time for the background predictions, associated to the dark matter search runs acquired in the period 2010 – 2014, as well as the exclusion limits for spin-independent elastic WIMP-nucleon interactions, have been outlined in Chapter 5. The selection of the single scatter events have been improved by defining a cut based on energy dependence and a lower threshold, obtaining a better efficiency. We have demonstrated the importance of this selection, since this category of events might be candidates of the WIMPs interactions. The quality of dark matter data sets acquired can be endangered by the inclusion of artificial events named *hot-spots* that are characterized by non-uniformities of the S_2 distribution on both top and bottom PMTs arrays. Cuts on the specific affected regions have been defined to equalize and correct the S_2 of the data sets. The anomalous S_2 events that generated the *hot spots* could be rejected without decreasing the nuclear recoils detection efficiency since these events do not have a corresponding signal from the primary scintillation in liquid Xe,

S_1. The acceptances for all the cuts used for the analysis have been calculated for 2 different energy ranges (3-14pe) and (14-30pe) using ER data and the variation in time for a period of 1 year has been studied. The sinusoidal variation extracted and the 3σ and 5σ upper limits derived showed no strong influence to be considered for the background estimation.

As it is essential to improve the sensitivity of terrestrial detectors for direct dark matter interactions detection with a lower background, but also to investigate various new technologies that are needed for the next XENON1T detector, data acquisition (Run14) and data analysis (preparation of Run12 un-blinding) will continue throughout the XENON100 Experiment as future developments. The new scientific data taking run already include new calibration procedures (neutrons from YBe source), that will be important both to assess the performance of the detector at the lowest energies and to identify the optimal calibration procedure for XENON1T. This means that new analysis tasks and experimental duties, locally at LNGS, will have to be accomplished.

In parallel with the activities performed for the XENON100 experiment, the development for XENON1T detector continued with excellent progress for all of the working groups responsible for its construction. In particular for the TPC, the design has been constantly updated, following discussions, simulations and R&D studies. Detailed 2D COMSOL electric field simulations have been accomplished allowing the selection for the optimal geometry of the electrodes and shaping rings, defining the TPC field cage. The operation drift field in the liquid phase for XENON1T TPC will be $1kV/cm$ applying $-100kV$ on the cathode (single wires mesh 5mm pitch) and the amplification voltage for the anode (hexagonal mesh, 3.75mm pitch) in the gas will be set to a value of $5kV$, with a very good uniformity of the electric field. Starting from this configuration, named *default model,* several studies have been made to increase the meshes transparencies since it is very important for the optimization of the scintillation detection efficiency. Taking into account the field uniformity and scintillation detection efficiency of the detector as the most important quality criteria to be obtained, our tests have shown that the pitches cannot be increased more than 5mm and 7.5mm for the anode/gate meshes and for the cathode mesh respectively, using a $127\mu m$ wire diameter and preserving the mechanical requests. 3D simulations have also been performed to assess the differences for the 2D simulations. Our studies have shown small differences due to the different transparencies obtained from the 3D:2D conversion for several cut planes applied or due to COMSOL and CPUs limitations. Studies of the secondary scintillation gain and peak resolution obtained from the 3D simulations of small volumes in the anode region confirmed the default model as the proper design for the field cage.

At the time of writing this thesis, this new dark matter detector, XENON1T was already in the phase of installation in Hall B of LNGS, aiming for a background goal of $10^{-4} evts\ kg^{-1} day^{-1} keV^{-1}$. It will provide the sensitivity to detect WIMPs in most of the theoretically favored parameter space, probing spin-independent WIMP-nucleon

scattering cross sections down to $2 \times 10^{-47} cm^2$ due mostly to the design of the experimental detection system that will allow to reduce significantly the electromagnetic background from external sources.

The studies presented in this thesis, as part of the XENON effort, addressing questions about fundamental properties of the Universe, not only will captivate the general public attention, but also society, as the imaging detectors and related technologies used can be applied outside the particle astrophysics field too, e.g. on national security or medical imaging research.

REFERENCES

[1] G. Brumfiel, *Unseen Universe: A constant problem,* Nature 448:245-246, 19 July 2007

[2] F. Zwicky, *The redshift of extragalactic fog,* Helvetica Physica Acta, 6:110-127, 1993

[3] J. Navarro et al., *The baryon of galaxy clusters: a challenge to cosmological orthodoxy,* Nature, 366:429-433, 1993

[4] D. Clowe, M. Bradac, A. H. Gonzales, M. Markevitch, S. W. Randall, C. Jones and D. Zaritsky, *A direct empirical proof of the existence of dark matter,* arXiv:astro-ph/0608407, 19 Aug 1996

[5] Jenny Hogan, *The search for structures,* Nature 448:244-245, 19July 2007

[6] D. Larson, J. Dunkley, G. Hinshaw, E. Komatsu, M. R. Nolta, C. L. Bennett, B. Gold, M. Halpern, R. S. Hill, N. Jarosik, A. Kogut, M. Limon, S. S. Meyer, N. Odegard, L. Page, K. M. Smith, D. N. Spergel, G. S. Tucker, J. L. Weiland, E. Wollack, and E. L. Wright. *Seven-year wilkinson microwave anisotropy probe (wmap) observations: Power spectra and wmap-derived parameters,* Astrophysics, arXiv:1001.4635 [astro-ph.CO], 26 Jan 2010

[7] B.J. Carr and S.W. Hawking, *Black holes in the early universe,* Mon. Not. Roy. Astron. Soc., 168:399-415, 1974

[8] Frank Wilczek, *Problem of strong P and T invariance in the Presence of Instantons,* Phys. Rev. Lett., 40:279-282, 1978

[9] Wayne Hu, Daniel J. Eisenstein and Max Tegmark, *Weighing neutrinos with galaxy survey,* Phys. Rev. Lett., 80:5255-5258, 1998

[10] Steen Hannestad, *Neutrino masses and the number of neutrino species from wmap and 2dfgrs,* JCAP, 0305:004, 2003

[11] P. Sikivie, *Experimental tests of the 'invisible' axion*, Phys. Rev. Lett., 51:1415, 1983

[12] Gerard Jungman, Marc Kamionkowski and Kim Griest, *Supersymmetric dark matter*, Phys. Rev. Lett., 267:195-373, 1996

[13] Dan Hopper, *TASI 2008 Lectures on dark Matter*, arXiv: 0901.4090 [hep-ph] FERMILAB-CONF-09-025-A

[14] A. F. Pachero and D. Strottman, *Nuclear structure corrections to estimates of the spin dependent WIMP nucleus cross-section*, Phys. Rev., D40:2131-2133, 1989

[15] M. T. Ressel and D. J. Dean, *Spin dependent neutralino nucleus scattering for an approx. 127 nuclei*, Phys. Rev., C56:535-546, 1997

[16] M. Ted Ressel et al., *Nuclear shell model calculations of neutralino – nucleus cross-section for Si-29 and Ge-73*, Phys. Rev., D48:5519-5535, 1993

[17] Kaixuan Ni, Laura Baudis, *Direct dark matter searches with CDMS and XENON*, Elsevier, Advances in Space Research, Vol. 41, Issue 12, pages 2019-2023, 2008

[18] J. D. Lewin and P. F. Smith, *Review of mathematics, numerical factors and corrections for dark matter experiments based on elastic nuclear recoil*, Astropart. Phys., 6:87-112, 1996

[19] XENON100 Collaboration (E. Aprile et al.), *Dark Matter Results from 225 Live Days of XENON100 Data*, arXiv: 1207.5988v1 [astro-ph.Co] 25 Jul 2012

[20] XENON100 Collaboration (E Aprile et al.), *First Results from the XENON10 Dark Matter Experiment at the Gran Sasso National Laboratory*, arXiv: 0706.0039v1 [astro-ph] 3 May 2007

[21] LUX Collaboration (D.S. Akerig et al.), *First results from the LUX dark matter experiment at the Sanford Underground Research Facility*, arXiv:1310.8214v2 [astro-ph.CO] 5 Feb 2014

[22] http://xenon-isotopes.com/

[23] S. Kubota et al., *Recombination Luminescence in Liquid Argon and in Liquid Xenon*, Phys.Rev. B 17(1978b), 2762

[24] R. D. Evans, *Atomic Nucleus* (McGraw-Hill New York, 1955), Chap. 12

[25] W. E. Meyerhof, *Elements of Nuclear Physics* (McGraw-Hill, New York, 1967)

[26] J. Jortner et al., *Localized Excitations in Condensed Ne, Ar, Kr, and Xe*, J. Chem. Phys.,42 (1965), 4250

[27] T. Takahashi et al., *Average Energy Expended per Ion Pair in Liquid Xenon*, Phys. Rev.A, 12 (1975), 1771

[28] T. Doke et al., *Absolute Scintillation Yields in Liquid Argon and Xenon for Various Particles*, Jpn. J. Appl. Phys., 41 (2002), 1538

[29] A. Hitachi, *Properties of Liquid Xenon Scintillation for Dark Matter Searches*, Astropart.Phys., 24 (2005), 247

[30] XENON100 Collaboration (E. Aprile et al.) – *Dark Matter Results from 100 Live Days of XENON100 Data*, arXiv: 1104.2549v3 [astro – ph.CO], 7 Sep 2011

[31] M. Yamashita et al., *Scintillation Response of Liquid Xe Surrounded by PTFE Reflector for Gamma Rays*, Nucl. Instrum. Meth. Phys. Res., Sect. A, 535 (2004), 692

[32] D. Nygren, *High pressure Xenon Gas Electroluminescent TPC for 0 Double Beta Decay Search*, Nucl. Instrum. Meth. A603 (2009) 337-348

[33] Monteiro et al., *Secondary scintillation Yield in Pure Xenon*, JINST 2, P05001 (2007)

[34] D.N. Spergel et al., *First-Year Wilkinson Microwave Anisotropy Probe (WMAP)* Observations: Determination of Cosmological Parameters*, Astrophys. J. Suppl. 148, 175 (2003)

[35] D.N. Spergel et al., *Wilkinson Microwave Anisotropy Probe (WMAP) Three Year Results: Implications for Cosmology*, astro-ph/0603449 (2006)

[36] A. Bottino, *Particle Dark Matter*, AIP Conf. Proc. 751, 46 (2005)

[37] K. Griest and M. Kamionkowsy, *Supersymmetric dark matter*, Phys. Rept. 333, 167 (2000)

[38] LNGS webpage, https://www.lngs.infn.it

[39] D. S. Akerib et al., *Limits on Spin-Independent Interactions of Weakly Interacting Massive Particles with Nucleons from the Two-Tower Run of the Cryogenic Dark Matter Search*, Phys. Rev. Lett. 96, 011302 (2006)

[40] M. Schumann, *XENON100 – Results and prospects*, Proceedings of TPC 2010, J. Phys.:Conf.Ser. 309 012011 (2011)

[41] XENON100 Collaboration (E. Aprile, et al.) – *The XENON100 Dark Matter Experiment*, arXiv: 1107.2155v2 [astro – ph.IM], 8 Feb 2012

[42] XENON100 Collaboration (E. Aprile, et al.) – *XENON wiki webpage:* https://xecluster.lngs.infn.it/dokuwiki

[43] M. Yamashita et al., *Scintillation response of liquid Xe surrounded by PTFE reflectors for gamma rays*, Nucl. Instrum. Meth. A, 535 692 (2004)

[44] XENON100 Collaboration (E. Aprile et al.) – *The distributed slow Control System of the XENON100 Experiment*, JINST **7** T12001 (2012)

[45] E. Aprile et al., *The XENON Dark Matter Search Experiment*, Nucl. Instrum. Meth. A, 535 692 (2004)

[46] A. Kish – *Dark Matter Search with the XENON100 Experiment, Ph.D. thesis*, University of Zurich, Switzerland, 2011

[47] E. Aprile, L. Baudis, B. Choi, K. L. Giboni, K. Lim, A. Manalaysay, M. E. Monzani, G. Plante, R. Santorelli, and M. Yamashita – *New measurement of the relative scintillation efficiency of xenon nuclear recoils below 10keV*, Phys. Rev. C, 79(4):045807, Apr 2009

[48] A.Manzur, A. Curioni, L. Kastens, D. N. McKinsey, K. Ni, and T. Wongjirad – *Scintillation efficiency and ionization yield of liquid xenon for mono-energetic nuclear recoils down to 4 keV*, Phys. Rev. C, 81(2):025808, Feb 2010

[49] XENON100 Collaboration (E. Aprile et al.), *First dark matter results from the xenon100 experiment*, arXiv: 1005.0380v3 [astro – ph.Co], 1 Mar 2011

[50] Lim Kyungeun, *AmBe calibration for Xenon100 detector*, Internal note of Xenon100 Analysis

[51] XENON100 Collaboration (E. Aprile et al.), *Analysis of the XENON100 Dark Matter Search Data*, Astropart. Phys. 54, 11 (2014)

[52] B. Edwards et al., *Measurement of single electron emission in two-phase xenon*, Astropart. Phys. 30, 54 (2008)

[53] XENON100 Collaboration (E. Aprile et al.), *Observation and applications of single-electron charge signals in the XENON100 experiment*, J. Phys. G: Nucl. Part. Phys. 41 (2014) 035201

[54] Fei Gao, *A width and energy dependent S2 single cut*, Internal note of XENON100 Analysis

[55] Catalin Balan, *First study of Xs2single cut for Run10*, Internal note of XENON100 Analysis

[56] Catalin Balan, *Second study of Xs2single cut for Run10*, Internal note of XENON100 Analysis

[57] Catalin Balan, *Study on Xs2single cut acceptances for Run10*, Internal note of XENON100 Analysis

[58] Luca Scotto Lavina, *Activities performed in Feb/Mar 2012 in the context of data reprocessing*, Internal note of XENON100

[59] Antonio J. M. Fernandez, *Estimation of cut acceptances in Run10*, Internal note of XENON100 Analysis

[60] Marc Weber, *Data/Monte Carlo comparisons for AmBe*, Internal note of XENON100 Analysis

[61] G. Bakale, U. Sowada, W.F. Schmidt, *Effect of an electric field on electron attachment to SF_6, N_2O, and O_2 in liquid argon and xenon*, J. Phys. Chem. 80, 2556 (1976)

[62] M.J. Travers, D.C. Cowles, G.B. Ellison, *Reinvestigation of the Electron Affinities of O_2 and NO*, Chem. Phys. Lett. 164, 449 (1989)

[63] R.G. Tonkyn, J.W. Winniczek, M.G. White, *Reinvestigation of the Electron Affinities of O2 and NO*, Chem. Phys. Lett. 164, 137, (1989)

[64] Lim Kyungeun, *Estimation of anomalous single scatter events in Xe100 data*, American Physical Society, APS April Meeting 2011, 2011APS.APRT11006L

[65] R. Wall, *Analysis of hotspots*, Internal note of XENON100 Analysis

[66] Fei Gao, *Limits on the annual modulation amplitude of XENON100 background*, Internal note of XENON100 Analysis

[67] F. Donato, *Ilustration of XENON1T detector at LNGS*, wiki page of XENON experiment

[68] A. James, *CAD drawings of XENON1T detector*, wiki page of XENON experiment

[69] A. I. Bolozdynya, *Two phase emission detectors and their applications*, Nucl. Instrum. Meth. A 422 (1999) 314–320

[70] Junji Naganoma, Petr Chagin, *Electric field simulations and tests for XENON1T detector*, Internal note of XENON1T experiment

[*] http://newscenter.lbl.gov/2009/10/27/evolving-dark-energy/

[**] http://www.solstation.com/x-objects/coma-sc.htm